Title
Physical mechanisms of immune-cell target recognition and point-of-care imaging diagnostics for neglected tropical diseases

Author
Bakalar, Matthew

Publication Date
2017

Peer reviewed|Thesis/dissertation

Physical mechanisms of immune-cell target recognition and point-of-care imaging diagnostics for neglected tropical diseases

By

Matthew H. Bakalar

A dissertation submitted in partial satisfaction of the

requirements for the degree of

Joint Doctor of Philosophy
with University of California, San Francisco

in

Bioengineering

in the

Graduate Division

of the

University of California, Berkeley

Committee in charge:

Professor Daniel A. Fletcher, Chair
Professor Zev Gartner
Professor Phillip Geissler

Summer 2017

Physical mechanisms of immune-cell target recognition and point-of-care imaging diagnostics for neglected tropical diseases

by Matthew H. Bakalar

Abstract

Physical mechanisms of immune-cell target recognition and point-of-care imaging diagnostics for neglected tropical diseases

by

Matthew H. Bakalar

Doctor of Philosophy in Bioengineering

University of California, Berkeley

Professor Daniel A. Fletcher, Chair

Controlled activation of immune cells protects the body from pathogens and disease while limiting damage to healthy self-cells Immune cells collect information through pattern-recognition receptors (PRRs) displayed on the cell membrane. While some PRRs respond to soluble ligands – small molecules, proteins, nucleotides, and sugars – signals are often transduced through direct physical contact – surface to surface – between an immune-cell and a potential target cell. Here, the cell-membrane is more than a passive platform for receptor display. Rather, the physical environment of the cell membrane influences the two-dimensional spatial organization of PRRs, which in turn controls their activation.

The goal of the first part of this dissertation is to describe a simple, protein size-dependent physical mechanism that can control protein organization at membrane-membrane interfaces. I begin by reconstituting a synthetic membrane-membrane interface in vitro using giant unilamellar vesicles decorated with adhesion proteins, and I use this model system to show that a size difference of ~5 nm relative to the membrane interface is sufficient to drive the exclusion of a tall non-binding protein from the interface. Combining in vitro measurements with Monte Carlo simulations, I find that non-binding protein exclusion is also influenced by lateral crowding, binding protein affinity, and, to a lesser extent, thermally-driven membrane height fluctuations that transiently limit access to the interface. This simple, sensitive, and highly effective means of passively segregating proteins has implications for signaling at many cell-cell contacts.

Next, I explore the consequences of size-dependent protein segregation at the interface between a macrophage and a target cell. Phagocytosis is mediated through activation of Fc receptors upon ligation with a surface-bound antibody, but it remains unclear how receptor-antibody binding triggers phosphorylation of the receptor, or how Fc receptors can accommodate the variable binding geometries formed by antigens with diverse structure, shape, and size. To determine the influence of antigen height on antibody-dependent phagocytosis, I reconstitute a minimal model of a target cell surface using lipid-bilayer coated glass beads and protein antigens with height-specific antibody binding sites. I find that phagocytosis is dramatically impaired for antigens that

position an antibody > 10 nm from the target surface. The finding that close contact (< 10 nm) between a macrophage and target cell is a requirement for triggering of Fc receptors suggests a new design principle for therapeutic monoclonal antibodies to stimulate immune effector cells against cancer and infectious disease.

Not all pathogens and diseases are recognized and cleared by the immune system. For those that result in chronic infections, especially in low-resource areas, advances in mobile technology can be used to aid in diagnosis and treatment. The last part of this dissertation describes the development of CellScope Loa, a mobile phone-based microscope for quantifying the blood-borne parasitic worm *Loa loa* at the point-of-care. Efforts to eliminate onchocerciasis and lymphatic filariasis in Central Africa through mass drug administration have been suspended because of ivermectin-associated serious adverse events, including death, in patients infected with the filarial parasite *Loa loa*. To safely administer ivermectin (IVM) for onchocerciasis or lymphatic filariasis in regions co-endemic with *L. loa*, a strategy termed "test and (not) treat" has been proposed whereby those with high levels of *Loa loa* microfilariae (>30,000/ml) that put them at risk for life-threatening serious adverse events are identified and excluded from mass drug administration. To address this, I worked on the development of an automated mobile-phone microscope for quantifying *Loa loa* directly in whole blood. The device has been used in Cameroon to identify and exclude individuals with >20,000 mf per milliliter of blood (at-risk for SAEs) from ivermectin treatment in a "test and treat" pilot, where IVM was safely delivered to more than 15,000 patients in a "test and treat" pilot.

Dedicated to my parents

Table of Contents

Acknowledgements

My time in graduate school has been time spent with an incredibly dedicated, creative, and kind group of people. I would like to take a moment to acknowledge those people who have made the last few years so valuable to me.

First, I would like to thank my research adviser Dan Fletcher for sharing his knowledge, scientific vision, and enthusiasm with me over the years. Dan leads by sharing his incredible curiosity and energy with us all. He creates endless space for exploring new ideas, and always takes time to be genuinely excited by the possibilities of a new project or approach. Every morning, Dan's first stop is in the lab, where he makes sure to visit with everyone who is around. I'll share what I'm working on, reading, or thinking about, not out of a formal obligation but because it is truly a pleasure to talk with Dan. Dan has taught me how to ask questions that are important, how I can use my expertise and resources to impact human health around the world, and to be fearless when approaching a new field of study. Most importantly, Dan has shown me how to treat a diverse group of people so that they feel valued and supported, an approach that is a foundation for the lab and the reason it has been such a pleasure to work here. Dan has been a tireless advocate of my career, and I am incredibly grateful for Dan's advice and support as I transition into a new post-doc position. I know that he will continue to be a colleague and a friend for many years to come.

I was extremely fortunate to have the opportunity to work with Eva Schmid, who has been a scientific partner and close friend to me over the years. Eva taught me how to approach biology with creativity, patience, and resilience, but most importantly, with joy. Eva also brought her son Jakob into the world two years ago, and it has incredibly to spend time with him as he learns to enjoy the simple pleasures of the park, good food, and great company.

I would like to thank to Mike D'Ambrosio, who has been an incredible partner on the Loa project over the years. Despite his background, Mike is a true engineer at heart. He has a vision that is often ahead of its time, a sense for design, and a commitment to building things that work. It has been a pleasure working with Mike to design and build the Loa device, and to together watch as it performs many thousands of tests without incident (to spec).

I am very thankful for my time with Phill Geissler. Phill took me into his lab for a research rotation despite my total lack of exposure to statistical mechanics. From there, he taught me a new language for describing the world, and a way to bring order to the incredible complexity of biological systems. He has been endlessly supportive of my career throughout many fellowship and post-doc applications, and I will always be grateful for his kindness.

I am thankful for the opportunity to work with Tom Nutman. Tom has been a dedicated and prescient partner on the Loa project, recognizing the opportunity that CellScope presented for detecting parasitic helminths, and working tirelessly with us to make the project a reality. It was also great fun to travel with Tom and Dan to Cameroon, where somehow the happy hours always seem a bit happier.

I would like to thank Ari Joffe, who has worked closely with me over the last two years. Ari's kindness, creativity, and quiet determination have made working alongside him a true pleasure.

My time in lab would not be the same without Mike Vahey, who has always been a source of knowledge and inspiration. Mike has been endlessly patient and truly generous, and I enjoy every moment at the desk beside him. Also, I'd like to extend special thanks to Andrew Harris for always understanding how to mix coffee, science, and soccer to make life in the lab fun and productive.

I am also grateful for the advice, scientific guidance, and good company over the years from my labmates: Brian Belardi, Carmen Chan, Marijia Podolski, Sungmin Son, Kathy Wei, Dan Friedman, Henry Pinkard, Max Armstrong, Tiama Hamkins-Indik and lab alumni: Pamela Jreij, Alba Diz-Munoz, Win Pin Ng, Matt Good, Neil Switz, Arunan Skandarajah, Peter Bieling, and Tai-De Li. I would also like to thank Julian Weichsel from the Geissler lab, and Scott Hansen from the Groves lab for sharing their knowledge and advice.

I would like to thank the members of my dissertation committee Phill Geissler and Zev Gartner, as well as members of my qualifying exam committee John Deuber, Bo Huang, and Orion Weiner. Your guidance, support, and friendship has made me feel like a welcome member of a community from the beginning.

To my fiancée Liza Comeau: I would not be here without your love and support, and I would not be the person I am today without your friendship. When nothing seems to work, I always know I can come home just to be near you, and that when I'm with you anything is possible.

To my sister, Dana Bakalar: You are a friend and an inspiration to me. I am so proud of everything you've accomplished, and so grateful to have you leading the way. Thank you for always understanding, and for always being there.

To my Mom and Dad: You've taught me what is beautiful in this world, and through your love you've shown me what matters. For everything, thank you.

Chapter 1 - Introduction

Immune cell recognition

Controlled activation of immune cells protects the body from pathogens and disease while limiting damage to healthy-self. In the struggle to survive, pathogens evolve elaborate mechanisms to evade, disable, or subvert the immune response for their own benefit[1]. Within the community of self-cells that compose an organism, tumor-cells play a similar game of cat and mouse, accumulating mutations that promote growth and proliferation while overcoming attempts by immune cells to disable and destroy them[2].

Individual cells are separated from their surroundings by the plasma membrane, and as a result the membrane has evolved into a dynamic interface for communication between a cell and its environment. Immune cells collect information through pattern-recognition receptors (PRRs) displayed on the cell membrane[3,4]. PRRs bind to 'molecular patterns', which are molecules that are found specifically on pathogens, in diseased or damaged cells, or in other unique contexts[5]. Some receptors respond to soluble ligands – small molecules, proteins, nucleotides, and sugars – that bind to PRRs. However, many signals are transmitted through direct physical contact – surface to surface – between an immune-cell and a target cell[6,7]. Here, binding between diverse immune-cell PRRs and a panel of surface-bound ligands transmits a multiplexed signal about the identity of the target, which is integrated to determine the nature of the cellular response (for instance, whether to attack or ignore a target). While the existence of many PRRs and their ligands has been catalogued, the physical mechanism that underlies the transmission of many PRR signals is an active area of study.

The cell membrane

More than a passive platform, the cell membrane influences the two-dimensional spatial organization of PRRs, which is critical to their activation[8,9]. The cell membrane is composed of lipids with diverse physical properties that comprise a semipermeable lipid bilayer. The bilayer is populated by proteins with amphipathic structure that promotes their stability within the lipid-bilayer[10]. Additional proteins are peripherally coupled to both the extracellular and cytoplasmic leaflet of the bilayer. The cell membrane can be described as a two-dimensional fluid – lipids and proteins diffuse about its surface while the physical structure of the bilayer is maintained. This physical property underlies Singer and Nicolson's four-decades old 'fluid-mosaic' model of the cell membrane, which describes the membrane as a dynamic tapestry of lipids and proteins in constant motion[11].

In recent years, it has become clear that spatial heterogeneity – the clustered distribution of proteins, lipid, and glycans within the bilayer – is important for cellular function. Multiple mechanisms have been implicated in the organization of proteins on membranes – including lipid rafts, protein-protein interactions, and spatial templating by the underlying cytoskeleton[9,12,13]. These mechanisms can be divided into three categories that I define here as: *in plane*, *onto plane*, and *out of plane*.

Physical principles of protein organization on the cell membrane

In plane mechanisms operate through lateral interactions within a single membrane. Examples include lipid rafts, where collective interactions between lipids within a single-bilayer generate

separate domains that are populated by some proteins, and protein clusters formed through energetically favored coupling between protein transmembrane domains[9]. *Onto plane* mechanisms are enforced by adsorption of a component from solution to the plane of the bilayer, such as occurs during ligand-induced dimerization of toll-like receptors or the recruitment of proteins to domains of charged lipids[14]. *Out of plane* mechanisms, which I will focus on in this thesis, occur when components that lie outside the bilayer enforce a boundary constraint on proteins within the bilayer. For instance, at the membrane-membrane contact site between an immune-cell and a target cell, protein-protein binding drives their enrichment via diffusion[15].

Out of plane organization at cell-cell contacts

When two cells meet at cell-cell contacts *out of plane* interactions abound. Physical contact between cells forms membrane interfaces that are important for cell-cell communication; for example, in epithelia and endothelia, initiation of cell-cell fusion during muscle formation, and T-cell activation at the immune synapse. The resultant membrane interface is composed of two closely apposed cell membranes. Each membrane is densely packed with proteins and glycans with diverse structures, and the confined space available at this interface makes it a rich site of protein-protein interaction – proteins bump into other proteins on their own and on the apposing bilayers – and for direct interactions between proteins and both lipid membranes.

The plasma membrane can be modeled physically as a semi-flexible elastic sheet – its propensity to resist bending in response to force is a function of the square of the Gaussian curvature of the membrane surface[16]. If the membrane-membrane distance at a contact site is smaller than the height of a protein on either surface, a protein will displace the membrane by bending the membrane surface (if the rigidity of the protein is greater than the rigidity of the membrane itself). However, because a membrane is fluid, proteins can also diffuse away from the membrane-membrane contact site, relieving the membrane of the necessity to bend. In cases where the energy of de-mixing (that is, perturbing the lateral concentration field of a protein by moving it out of a given membrane region) is less than the energetic penalty of bending the membrane, bringing membranes into close contact is a way of transducing a *vertical* change in membrane position into a *lateral* change in protein organization.

Macrophage phagocytosis

One context in which crowded membranes are rapidly brought into close contact, subjecting them to new *out of plane* organizing mechanisms, is upon binding between a macrophage and a potential target[17]. Macrophages protect the body from damage and disease by targeting antibody-opsonized cells for phagocytosis. Macrophage target recognition is subject to particularly intimate contact, as successful phagocytosis requires zippering-up against a target surface in order to physically internalize a target[18]. At the molecular scale, phagocytosis is mediated through activation of Fc receptors upon ligation with a target surface-bound antibody, which triggers local actin polymerization and downstream signaling.

In addition to their well-known roles targeting bacterial and fungal pathogens, macrophages have recently been found to be potent effectors of anti-tumor activity[19]. It is becoming increasingly clear that monoclonal antibody therapy against tumor-specific antigens depends on the ability of macrophages and other innate-immune cells to target their effector attack, including phagocytosis and the release of cytotoxic components, against antibody-bound cells.

Macrophages, along with dendritic cells, are sentinels of the immune system, and in addition to the direct impact of killing tumor cells, they are able to process and present tumor-specific peptides to T-cells to stimulate the adaptive arm of the immune system[20].

As antibody therapeutics move into the clinic, it is important to understand their mechanism of action. It is known that the structure of the antibody Fc domain can modulate an immune response, but does the structure of the antigen itself, which anchors the antibody in a unique position and orientation relative to the cell-surface, impact the activity of immune effector cells? Antigens are physically diverse, with variations in structure, shape, and size. At the macrophage-target interface, the antigen antibody-binding site directly modulates membrane-membrane distance by defining the structure of the antibody-Fc receptor complex, determining which *out of plane* organizing principles (such as physical segregation) are at play. Whether and how macrophages might accommodate variability in antigen structure has implications for the development of therapeutic antibodies.

Bottom-up reconstitution of cell-like systems

How do we understand the physical principles that govern the organization of a complex cellular system? Techniques in cell-biology have been historically top-down – biological systems can be observed and their properties measured at multiple scales, and small numbers of parts can be removed using genetics. An emerging approach for unraveling the complexity inherent in biology turns this on its tail – bottom-up reconstitution. Its philosophy is this: if we truly understand the assembly rules of a system, we should be able to build it from the ground up. Reconstitution uses both isolated biological parts (purified proteins, cellular lipids) and synthetic parts (recombinant synthetic proteins, chemically synthesized lipids), along with externally enforced physical boundary conditions (for instance, a two-dimensional surface for assembly of a lipid bilayer)[21]. Reconstitution makes it possible to test the influence of biophysical parameters in a quantitative manner, while reducing the possibility that perturbations are having unknown effects on other parts of the system. At its core, reconstitution is an effort to limit the collection of unknown unknowns while explicitly categorizing the known unknowns. Reconstitution is an important experimental approach in this thesis. In Chapter 2, I describe the use of giant vesicles and synthetic proteins to reconstitute cell-cell adhesion in order describe explore the principles of protein organization at membrane contact sites. In Chapter 3, I develop a reconstituted macrophage target in order to introduce a physically controlled input to Fc-receptors.

Neglected tropical diseases and mobile microscopy

Uncovering the mechanisms of immune-cell target recognition has the potential to influence the treatment of human diseases caused by pathogens, which have evolved numerous ways of evading detection[1]. The parasitic helminth is one class of human pathogen that has had a devastating impact on human health around the world. Helminths exert a remarkable influence on the regulation of the immune system, dampening the body's response to allergens and decreasing the inflammation in order to protect themselves from expulsion from the body[22]. This leads to some surprising benefits, including a reduction in autoimmune disease and allergy, in infected populations. Unfortunately, parasitic helminths are also the cause debilitating diseases that affect millions of people in primarily low-resource settings.

Diseases caused by the parasitic helminths *Loa loa* and *Onchocerca volvulus* are a leading cause of infective blindness worldwide, with severe impacts on public health and economic development in Africa[23,24]. While mass drug administration (MDA) programs with Ivermectin (IVM) are extremely effective for onchocerciasis control, IVM can induce serious adverse events in individuals who are co-infected with *Loa* microfilariae (mf)[25]. A potential solution to prevent *Loa*-associated SAEs is to identify *Loa* infected individuals at highest risk (>30,000 mf/mL of blood) and to exclude them from IVM treatment.

In chapter 4 of this thesis, I describe the development an automated mobile-phone microscope for quantifying *Loa loa* directly in whole blood[26]. The device images a magnified blood sample onto the camera of a mobile phone, and an algorithm automatically detects the wriggling motion of *Loa* to localize individual microfilariae. The devices was used in the summer and fall of 2015 to identify and exclude individuals with >20,000 mf per milliliter of blood (at-risk for SAEs) from ivermectin treatment in a "test and treat" pilot, where IVM was safely delivered to more than 15,000 patients in a "test and treat" pilot. In the spring of 2017, a new "test and treat" trial was repeated in the pilot population, resulting in safe delivery of an additional ~15,000 doses of IVM.

Neglected tropical diseases (NTDs), including those caused by helminth infections, account for enormous suffering around the world both through direct impacts on patient health and through the economic burdens of illness that strike effected communities. Combatting neglected tropical disease will continue to require new tools – simple and effective medications, means for delivering those medications, and methods for detecting who needs them – due to the unique economic constraints of the impacted communities. Further, as the medical community moves from control of endemic disease to local elimination, tracking disease becomes increasingly important in order to ensure population-level control. Diagnostic technologies that are affordable, simple, accessible, and trusted are an important part of the battle against NTDs[27].

Scope of the thesis

In Chapter 2, I describe a simple physical mechanism that drives protein organization at cell-cell contacts that arises from the interaction of proteins constrained to two-dimensions pushing against a semi-flexible lipid-bilayer. In Chapter 3, I explore the consequences of this mechanism on target recognition by macrophages, demonstrating that tall target antigens can disrupt phagocytosis simply by changing the physical constraints of the membrane-interface. In Chapter 4, the thesis takes a turn into the development of a new microscopy-based diagnostic for neglected tropical disease. Microscopy is the fundamental approach in this thesis for understanding the organizing principles of membrane interfaces – 'you can see a lot just by observing'[28]. Microscopy is also at the core of medical pathology – it is the oldest, often the cheapest, and most accessible approach to diagnostics. Translating microscopy into the field to diagnose parasitic disease is a powerful way to have an immediate impact on human health. My work in the Fletcher lab has been incredibly exciting and rewarding to me personally, and I hope it makes for an interesting read.

References

1. Roy, C. R. & Mocarski, E. S. Pathogen subversion of cell-intrinsic innate immunity. *Nat. Immunol.* **8,** 1179–1187 (2007).

2. Iannello, A., Thompson, T. W., Ardolino, M., Marcus, A. & Raulet, D. H. Immunosurveillance and immunotherapy of tumors by innate immune cells. *Curr. Opin. Immunol.* **38,** 52–58 (2016).
3. Gordon, S. Pattern Recognition Receptors. *Cell* **111,** 927–930 (2002).
4. Erwig, L. P. & Gow, N. A. R. Interactions of fungal pathogens with phagocytes. *Nat. Rev. Microbiol.* **14,** 163–176 (2016).
5. Tang, D., Kang, R., Coyne, C. B., Zeh, H. J. & Lotze, M. T. PAMPs and DAMPs: Signal 0s that Spur Autophagy and Immunity. *Immunol. Rev.* **249,** 158–175 (2012).
6. Goodridge, H. S. R. Activation of the innate immune receptor Dectin-1 upon formation of a 'phagocytic synapse'. *Nature* **472,** 471 (2011).
7. Flannagan, R. S., Canton, J., Furuya, W., Glogauer, M. & Grinstein, S. The phosphatidylserine receptor TIM4 utilizes integrins as coreceptors to effect phagocytosis. *Mol. Biol. Cell* **25,** 1511–1522 (2014).
8. Beekman, J. M., van der Linden, J. A., van de Winkel, J. G. J. & Leusen, J. H. W. FcγRI (CD64) resides constitutively in lipid rafts. *Immunol. Lett.* **116,** 149–155 (2008).
9. Lingwood, D. & Simons, K. Lipid Rafts As a Membrane-Organizing Principle. *Science* **327,** 46–50 (2010).
10. Physical properties of the fluid lipid-bilayer component of cell membranes: a perspective | Quarterly Reviews of Biophysics | Cambridge Core. Available at: https://www.cambridge.org/core/journals/quarterly-reviews-of-biophysics/article/physical-properties-of-the-fluid-lipid-bilayer-component-of-cell-membranes-a-perspective/816F1B5DAE587B3A42EE81BE92D3B071. (Accessed: 1st July 2017)
11. Singer, S. J. & Nicolson, G. L. The Fluid Mosaic Model of the Structure of Cell Membranes. *Science* **175,** 720–731 (1972).
12. Dustin, M. L. & Cooper, J. A. The immunological synapse and the actin cytoskeleton: molecular hardware for T cell signaling. *Nat. Immunol.* **1,** 23–29 (2000).
13. Banani, S. F., Lee, H. O., Hyman, A. A. & Rosen, M. K. Biomolecular condensates: organizers of cellular biochemistry. *Nat. Rev. Mol. Cell Biol.* **18,** 285–298 (2017).
14. Akira, S. & Takeda, K. Toll-like receptor signalling. *Nat. Rev. Immunol.* **4,** 499–511 (2004).
15. Dustin, M. L., Chakraborty, A. K. & Shaw, A. S. Understanding the Structure and Function of the Immunological Synapse. *Cold Spring Harb. Perspect. Biol.* **2,** (2010).
16. Fluid lipid membranes - a primer. *ResearchGate* Available at: https://www.researchgate.net/publication/252159182_Fluid_lipid_membranes_-_a_primer. (Accessed: 4th July 2017)
17. Flannagan, R. S., Jaumouillé, V. & Grinstein, S. The Cell Biology of Phagocytosis. *Annu. Rev. Pathol. Mech. Dis.* **7,** 61–98 (2012).
18. Jaumouillé, V. & Grinstein, S. Receptor mobility, the cytoskeleton, and particle binding during phagocytosis. *Curr. Opin. Cell Biol.* **23,** 22–29 (2011).
19. Gül, N. *et al.* Macrophages eliminate circulating tumor cells after monoclonal antibody therapy. *J. Clin. Invest.* **124,** 812–823 (2014).
20. Gajewski, T. F., Schreiber, H. & Fu, Y.-X. Innate and adaptive immune cells in the tumor microenvironment. *Nat. Immunol.* **14,** 1014–1022 (2013).
21. Liu, A. P. & Fletcher, D. A. Biology under construction: in vitro reconstitution of cellular function. *Nat. Rev. Mol. Cell Biol.* **10,** 644–650 (2009).

22. Maizels, R. M. & Yazdanbakhsh, M. Immune Regulation by helminth parasites: cellular and molecular mechanisms. *Nat. Rev. Immunol.* **3,** 733–744 (2003).
23. Osei-Atweneboana, M. Y., Eng, J. K., Boakye, D. A., Gyapong, J. O. & Prichard, R. K. Prevalence and intensity of Onchocerca volvulus infection and efficacy of ivermectin in endemic communities in Ghana: a two-phase epidemiological study. *The Lancet* **369,** 2021–2029 (2007).
24. Kamtchum Tatuene, J. *et al.* Epidemiology of Loa loa and Mansonella perstans filariasis in the Akonolinga health district, Centre Region, Cameroon. *Health Sci. Dis.* **15,** (2014).
25. Boussinesq, M., Gardon, J., Gardon-Wendel, N. & Chippaux, J.-P. Clinical picture, epidemiology and outcome of Loa-associated serious adverse events related to mass ivermectin treatment of onchocerciasis in Cameroon. *Filaria J.* **2,** S4 (2003).
26. D'Ambrosio, M. V. *et al.* Point-of-care quantification of blood-borne filarial parasites with a mobile phone microscope. *Sci. Transl. Med.* **7,** 286re4-286re4 (2015).
27. Hotez, P. J. *et al.* Eliminating the Neglected Tropical Diseases: Translational Science and New Technologies. *PLoS Negl. Trop. Dis.* **10,** e0003895 (2016).
28. Berra, Y. *The Yogi Book: 'I Really Didn't Say Everything I Said'*. (Workman Publishing, 2010).

Chapter 2

Size-dependent protein segregation at membrane interfaces

Eva M Schmid*[1], Matthew H Bakalar*[2], Kaushik Choudhuri[3,4], Julian Weichsel[5], HyoungSook Ann[1,6], Phillip L Geissler[5,7], Michael L Dustin[3,8], and Daniel A Fletcher[1,2,9]

[1]Department of Bioengineering, University of California, Berkeley, CA; [2]UC Berkeley / UC San Francisco Graduate Group in Bioengineering, Berkeley, CA; [3]Skirball Institute, New York University School of Medicine, New York, NY; [4]Current address: Department of Microbiology and Immunology, University of Michigan Medical School, MI; [5]Department of Chemistry, University of California, Berkeley, CA; [6]Current address: Institute for Genomic Biology, University of Illinois at Urbana-Champagne. IL; [7]Chemical Sciences Division, Lawrence Berkeley National Laboratory, Berkeley, CA; [8]Kennedy Institute, NDORMS, University of Oxford, Oxford, UK; [9]Physical Biosciences Division, Lawrence Berkeley National Laboratory, Berkeley, CA.

*Co-first author.

Abstract:
Membrane interfaces formed at cell-cell junctions are associated with characteristic patterns of membrane protein organization, such as E-cadherin enrichment in epithelial junctional complexes and CD45 exclusion from the signaling foci of immunological synapses. To isolate the role of protein size in these processes, we reconstituted membrane interfaces in vitro using giant unilamellar vesicles decorated with synthetic binding and non-binding proteins. We show that size differences between binding and non-binding proteins can dramatically alter their organization at membrane interfaces in the absence of active contributions from the cytoskeleton, with as little as a ~5 nm increase in non-binding protein size driving its exclusion from the interface. Combining in vitro measurements with Monte Carlo simulations, we find that non-binding protein exclusion is also influenced by lateral crowding, binding protein affinity, and thermally-driven membrane height fluctuations that transiently limit access to the interface. This simple, sensitive, and highly effective means of passively segregating proteins has implications for signaling at cell-cell junctions and protein sorting at intracellular contact points between membrane-bound organelles.

Introduction:
Direct physical contact between cells forms membrane interfaces that are important for cell-cell communication; for example, in epithelia and endothelia, initiation of cell-cell fusion during muscle formation, and T-cell activation in the immune system[1–3]. These membrane interfaces are comprised of two closely apposed plasma membranes that are densely packed with binding proteins that form adhesions and non-binding proteins that occupy space in the interface but do not form adhesions. Specific binding proteins, such as E-cadherins, are known to be enriched at membrane interfaces[4] and to hold the membranes together. The membrane separation distances at these junctions are determined, at least in part, by size of the binding proteins that form the interface and could, in principle, influence which non-binding proteins are permitted at the interface. However, there is no quantitative understanding of the fundamental interplay of protein size and membrane properties on the segregation of binding and non-binding proteins at membrane interfaces.

Recently, spatial organization of binding and non-binding proteins at membrane interfaces has been found to be critical for function[5,6]. One well-studied example is the immunological synapse (IS) formed during initiation of the adaptive immune response, during which peptide-bound Major Histocompatibility Complexes (pMHCs) on the surface of an antigen-presenting cell interact with T-Cell Receptors (TCRs) on the apposing T-cell membrane[7–9]. Subsequent activation of the T-cell relies on spatial segregation of proteins that make up a kinase–phosphatase system, wherein the transmembrane phosphatase CD45, which has a large extracellular domain, is excluded from pMHC/TCR clusters[10–13], permitting stable TCR phosphorylation and a downstream signaling cascade leading to activation[14–16].

Multiple mechanisms have been implicated in the organization of proteins at membrane interfaces, including receptor-ligand clustering by diffusion and trapping, lipid raft formation, intracellular protein-protein interactions, protein displacement based on size of the extracellular domain, and reorganization driven by the underlying cortical cytoskeleton[17–19]. Modeling of binding proteins at membrane interfaces has revealed that binding affinities, membrane fluctuations, and mixing entropy can produce phase transitions that segregate different binding

proteins[20]. In the immunological synapse, it has been suggested that exclusion of the non-binding protein CD45 is driven by a size-dependent mechanism[12,21,22], since CD45 isoforms can have extended conformations that are 15-40 nm larger than the space between apposing membranes imposed by pMHC/TCR binding at the membrane interface[16,23]. Detailed simulations of membrane interfaces have provided important insight into the organization and affinity of binding proteins[24–26], but little is known about how the interplay between binding proteins and non-binding proteins contributes to protein segregation at membrane interfaces.

Here we show that size alone is sufficient to titrate non-binding protein exclusion from membrane interfaces, absent the underlying dynamics of the actin cortex, receptor-ligand clustering, and complex lipid composition of the plasma membrane. We find that nanometer-scale increases in non-binding protein height beyond that of the binding protein will monotonically increase non-binding protein exclusion. We also show that lateral crowding of binding proteins at the membrane interface can exclude non-binding proteins regardless of their height within an interface. Since lateral crowding depends on surface area coverage of the binding protein, this demonstrates a direct connection between lateral footprint and binding affinity of one protein species and exclusion of another. We use Monte Carlo simulations to generalize and extend these results to show that changes in binding protein affinity govern the maximum inclusion of non-binding proteins due to lateral crowding and to reveal that changes in membrane bending rigidity have only a modest effect on protein segregation. The experiments and simulations presented here provide a framework for predicting the size-dependent organization of both binding and non-binding proteins at membrane interfaces – patterns that can either directly contribute to functional cell-cell interactions or must be modified by active processes in the cell for productive signaling.

Results:

In vitro membrane interface system

To experimentally isolate the role of protein size on segregation, we developed a simplified membrane interface system using giant unilamellar vesicles (GUVs) decorated with synthetic binding and non-binding proteins (Fig. 1a and 1b). We chose Green Fluorescent Protein (GFP)uv, an anti-parallel homodimer, as a homophilic binding protein (BP) because its binding affinity (Kd = 20-100 μM[27,28]) is in the range of TCR/pMHC interactions (Kd = 0.1–500 μM[29], and references therein). Since GFPuv is not spherical (~4.5 nm height, ~4 nm width, ~ $(4\ nm)^2$ cross-sectional area; PDB: 1GFL), we refer to protein size in two distinct ways: (i) height above the membrane and (ii) lateral footprint on the membrane. We used mCherry, which has nearly identical dimensions to GFPuv, as the modular building block for a set of non-binding proteins of different heights above the membrane but constant lateral footprints (see Methods): single length (NBP), double length (2L-NBP), and triple length (3L-NBP). We similarly constructed a set of binding proteins of increasing height above the membrane using dark mCherry as the modular spacer (see Methods): single length (BP), double length (2L-BP), and triple length (3L-BP). All binding and non-binding proteins had a single fluorescent molecule (either mCherry or GFPuv) and used non-fluorescent mCherry for additional length.

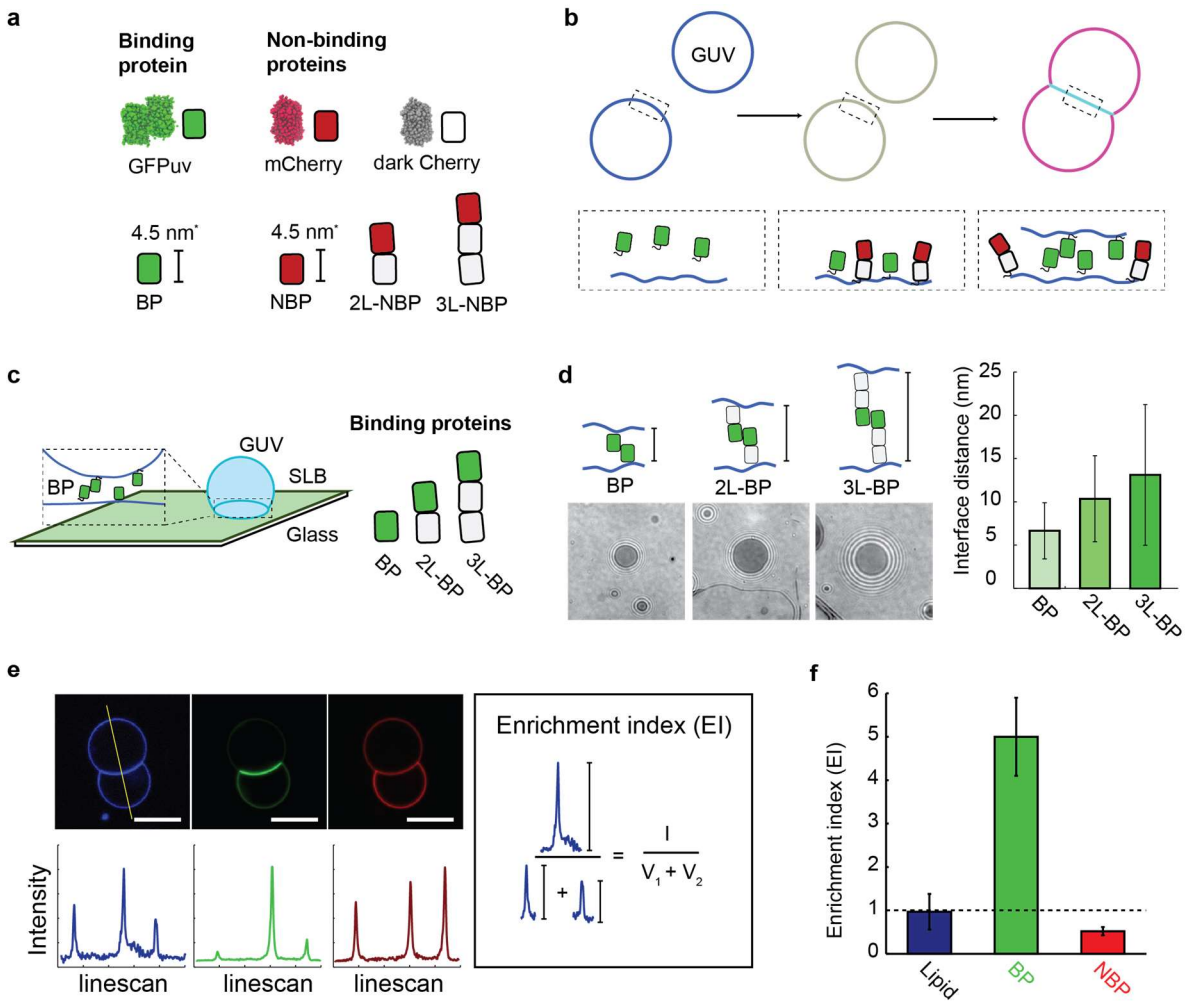

Figure 1: **a**, Synthetic binding proteins (GFPuv, BP) and non-binding proteins (mCherry variants, NBP, 2L-NBP, 3L-NBP) are used to investigate protein segregation at membrane interfaces. (* height estimated from crystal structure) **b**, Membrane interfaces are formed after the synthetic proteins bind to giant unilamellar vesicles (GUVs) that then come into contact. His-tagged binding proteins and non-binding proteins first attach to DOGS-Ni-NTA containing GUV membranes, and then binding protein dimerization leads to interface formation and protein segregation, which can be monitored fluorescently. **c**, Membrane interfaces with different gap sizes were formed using binding proteins of different lengths (BP, 2L-BP, 3L-BP) and quantified using reflection interference contrast microscopy (RICM) at an interface formed between a supported lipid bilayer (SLB) and a GUV. **d**, Representative RICM images at the interface between GUV and SLB for interfaces formed with BP, 2L-BP and 3L-BP. Image contrast and refractive index differences were used to extract the axial distance between the two membranes. Interface distance increased monotonically with the addition of spacer modules, forming interfaces of 6.2 ± 3 nm (BP), 10.3 ± 5.0 nm (2L-BP) or 13.1 ± 8.1 nm (3L-BP). Error bars are standard deviation across N = 10 vesicles. **e**, Representative confocal fluorescence images of GUVs (composition: 97.2% DOPC, 2.5% DOGS-Ni-NTA, 0.3% Atto 390-DOPE) incubated with 100 nM BP and 100 nM 2L-NBP in solution

for 10 min. Scale bar is 5 μm long (blue channel: Atto 390-DOPE, green channel: BP, red channel: NBP). Linescans through vesicles dimers allow for quantification of fluorescence intensity at outside vesicle membranes (V_1 and V_2) and interface (I). We calculate an 'Enrichment index' (EI) by taking the ratio between (I) and the sum of (V_1 and V_2). **f**, Plot of the EI revealing uniform distribution of the fluorescently labelled lipid (EI = 1), enrichment of BP (EI > 1) and exclusion of 2L-NBP (EI < 1) at the interface. Error bars are standard errors of the mean from three independent experiments on separate vesicle batches, each with ~50 vesicles quantified.

The binding proteins and non-binding proteins were expressed and purified with an N-terminal deca-His tag, enabling fluid protein attachment to Ni-chelating lipids (DOGS-Ni-NTA) on the synthetic GUV membranes. GUVs were prepared with typical protein densities on the vesicle surface of ~2,300 molecules/um^2 as measured by fluorescence correlation spectroscopy (FCS) (see Methods and Supplementary Figure S1). For proteins with lateral footprints of (4 nm)^2, this corresponds to a protein surface area coverage of approximately 3.7%, which is lower than the total membrane protein coverage on cellular membranes (~20,000 to 130 000 molecules/um^2) [28,29]. GUVs containing only binding proteins showed protein enrichment at the interface, while GUVs containing only non-binding proteins showed no interface formation, as expected (Supplementary Figure S2).

We used reflection interference contrast microscopy (RICM) between a GUV and a supported lipid bilayer[30] to determine the average distance between membranes at interfaces formed by the synthetic binding proteins (Fig. 1c; see Methods). Single length binding protein BP on both membranes formed membrane interfaces separated by 6.2 +/- 3.0 nm, consistent with size estimates from crystal structures of GFP-dimers (PDB: 1GFL[31]). Double and triple length binding proteins (2L-BP and 3L-BP) on both membranes formed membrane interfaces separated by 10.3 +/- 5.0 nm for 2L-BP and 13.1 +/- 8.1 nm for 3L-BP (Fig. 1d). As expected for thermally-driven proteins that may tilt at the membrane interface, the measured RICM distance is somewhat shorter than the estimated extended structure. The size of the non-binding proteins could not be directly measured with this approach because of the lack of a second interface needed for RICM.

To quantify the relative proportion of proteins at membrane interfaces containing both binding and non-binding proteins, we measured fluorescence intensity along a line bisecting the GUV-GUV pair and calculated an "Enrichment Index" (EI) – the intensity ratio between the interface (I) and the sum of the individual vesicle intensities (V1+V2) (Fig. 1e). EI values greater than 1 indicate an enrichment of molecules (increased surface density, #/μm^2) at the membrane interface, while EI values that are less than 1 indicate an exclusion of molecules (decreased surface density) at the membrane interface (Fig. 1f). An EI of 1 is expected for a fluorescent molecule that is distributed homogenously across each vesicle's surface.

Effect of protein height on segregation

We began quantifying size-dependent segregation by separately incorporating the three non-binding proteins of different heights (NBP, 1L-NBP, 2L-NBP) with the single-length (shortest) binding protein (Fig. 2a). Pairs of GUVs containing both binding proteins and non-binding proteins showed significant protein reorganization at the membrane interface (Fig. 1c), with the binding protein BP significantly enriched (EI = 3.54 +/- 1.25), leading to an estimated binding

protein density of ~8,200 molecules/μm^2 at the interface, or 13.2% membrane area coverage (see Methods). In contrast, we found that all non-binding proteins were excluded, though to varying extent (Fig. 2b). Single length non-binding protein (NBP) was partially excluded (EI = 0.52 +/- 0.17), while double length non-binding protein (2L-BP) was significantly excluded (EI = 0.14 +/- 0.11). Triple length non-binding protein (3L-BP) was similarly excluded (EI = 0.13 +/- 0.13), suggesting that protein exclusion has reached a limit. To control for any changes in membrane morphology at the interface, we included a fluorescently-labeled lipid (Atto 390-DOPE) and confirmed that it was neither enriched nor excluded (EI = 0.97 +/- 0.41) (Fig. 2b).

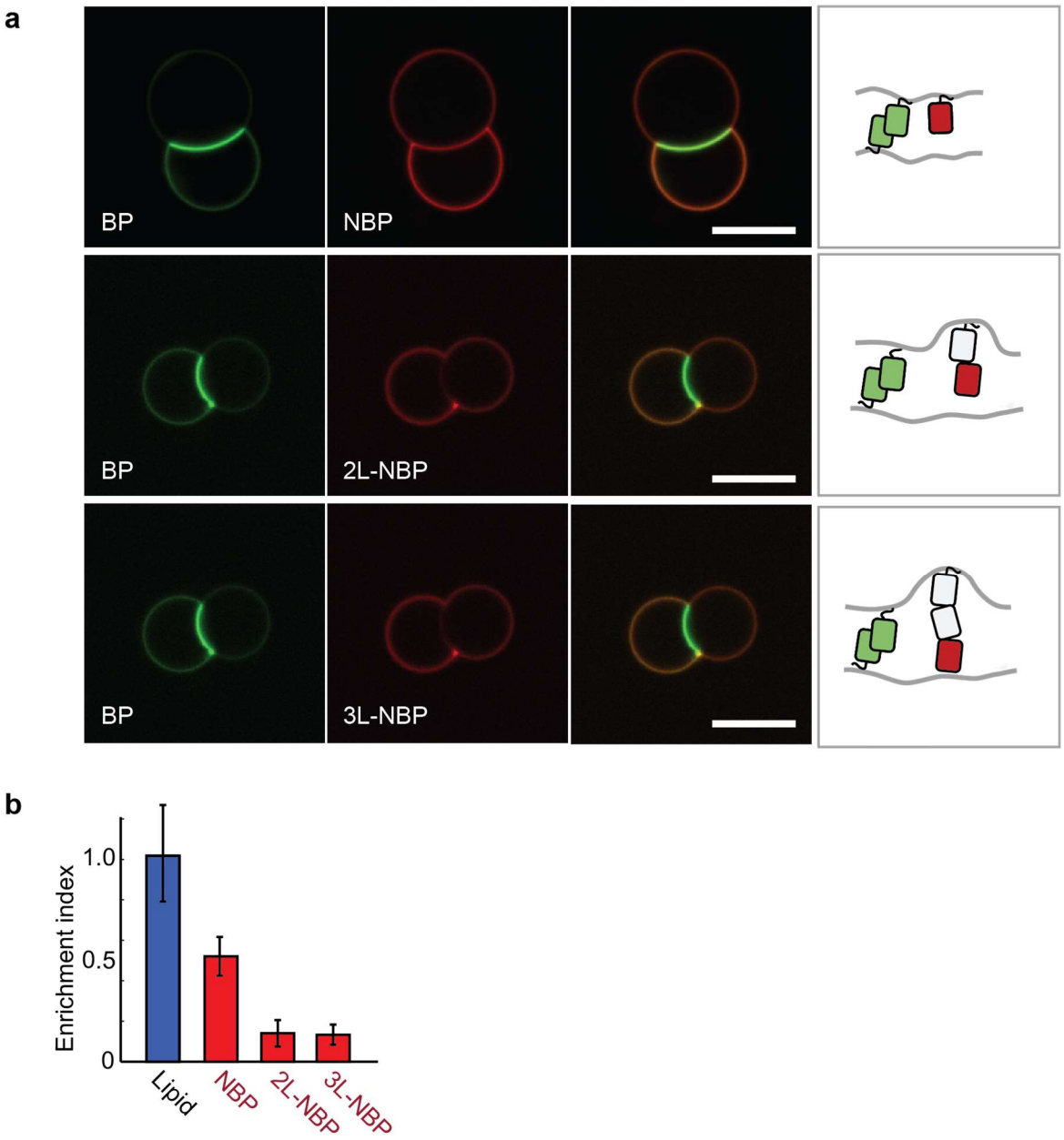

Figure 2: **a**, Representative confocal fluorescence images of non-binding protein (NBP) exclusion from GUV interfaces formed with the single-length binding protein (BP). GUVs (composition: 97.2% DOPC, 2.5% DOGS-Ni-NTA, 0.3% Atto 390-DOPE) were

incubated with 100 nM BP and 100 nM NBP, 2L-NBP, or 3L-NBP in solution for 10 min. Scale bar is 10 μm long (green channel: BP, red channel: NBP, 2L-NBP, or 3L-NBP). **b**, Quantification of NBP, 2L-NBP and 3L-NBP exclusion from BP interfaces in comparison to a fluorescently labelled lipid (Atto 390-DOPE), which should not exhibit size-dependent exclusion. Error bars are standard errors of the mean from three independent experiments on separate vesicle batches, each with ~50 vesicles quantified.

A single mCherry is approximately 4.5 nm (PDB: 2H5Q) in height, so the 2L-NBP and 3L-NBP are expected to be ~9.0 nm and ~13.5 nm, respectively, in their extended configuration. Since the measured distance of the membrane interface created by the single length binding protein (BP) is only 6.2 +/- 3 nm, the membrane interface must bend in order to accommodate the 2L-NBP and 3L-NBP. To test whether membrane bending is associated with exclusion of long non-binding proteins from the membrane interface, we captured multi-channel fluorescence and RICM images of membrane interfaces formed between SLBs and GUVs. When single length binding protein (BP) interfaces were formed in the presence of triple length non-binding proteins (3L-NBP), small clusters of the tall non-binding proteins were observed that excluded the short binding protein (Fig. 3a). RICM imaging of the membrane interface revealed regions of increased membrane separation that were co-localized with 3L-NBP clusters (yellow arrows in Fig. 3a lower panel), which coarsened over time to minimize total bending across the membrane interface (Fig. 3b). This behavior is consistent with an elastic model that attributes exclusion to the minimization of membrane bending energy[32].

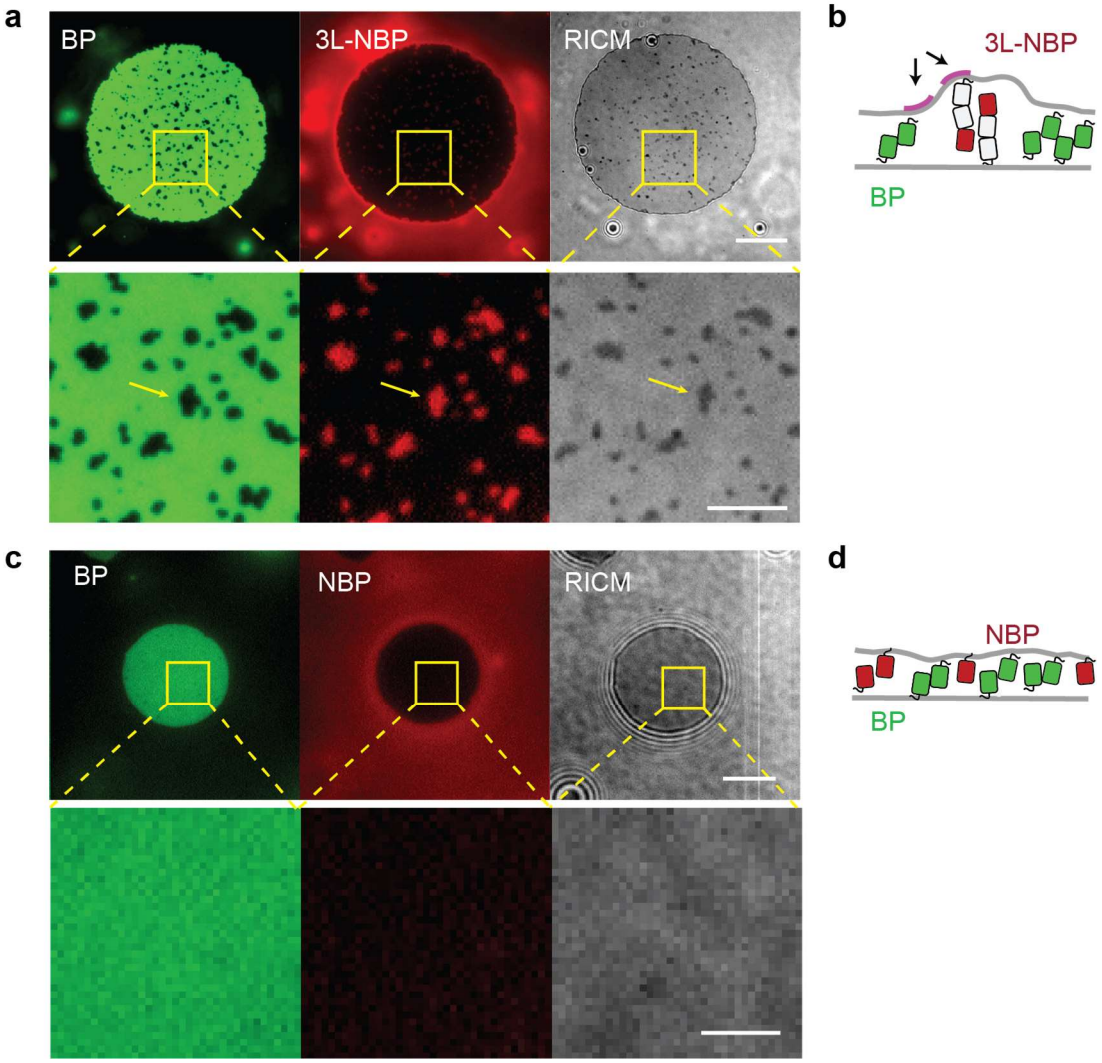

Figure 3: a, Representative multichannel fluorescence and RICM images of membrane interface formation between SLBs and GUVs showing cluster formation of the triple-length non-binding protein (3L-NBP, red). The 3L-NBP clusters exclude the single-length binding protein (BP, green) and co-localize with increased membrane distance (darker contrast, RICM), indicating there is a bending energy penalty for inclusion of long non-binding proteins at the membrane interface. Lower panels show zoomed regions of images in the upper panels. At long times, the long non-binding protein clusters are fully excluded from the interface. Scale bars 10 μm. **b**, Cartoon representation of long non-binding protein cluster formation and associated membrane bending stress (arrows). **c**, Representative multichannel fluorescence and RICM images of membrane interface formation between SLBs and GUVs show no cluster formation of the single-length non-binding protein (NBP, red), no exclusion of the single-length binding protein, and no membrane bending in RICM. Scale bars 10 μm. **d**, Cartoon representation of single-length non-binding proteins and single-length binding proteins at a membrane interface, where protein crowding could influence exclusion.

If long non-binding proteins are excluded from membrane interfaces due to membrane bending, proteins shorter than the interface distance should not be excluded. However, the single length non-binding protein (NBP), which is shorter (~4.5 nm) than the measured single length binding protein (BP) membrane interface distance (6.2 +/- 3 nm), was still partially excluded (EI = 0.52 +/- 0.17) (Fig. 2a and 2b). Using a combination of fluorescence microscopy and RICM, we again looked for localized membrane deformation in interfaces formed with BP and NBP but found only uniform fluorescence and no clusters or RICM contrast changes indicating deformation (Fig. 3c), suggesting that exclusion of a non-binding protein shorter than the interface cannot be explained by a simple elastic membrane model of protein segregation. Instead, we hypothesized that lateral protein crowding may be involved (Fig. 3d).

Effect of protein crowding on segregation

To test whether lateral protein crowding at the interface contributes to exclusion of non-binding proteins from the membrane interface, we lowered the concentration of the binding protein (BP) in solution from 100 nM to 25 nM, resulting in a proportional decrease in protein density at the interface from 11,585 / μm^2 (or 18.5% coverage) at 100 nM to 1,930 molecules / μm^2 (or 3% coverage) at 25 nM (Supplementary Figure S4). This reduced binding protein density resulted in a decrease in single length non-binding protein (NBP) exclusion (Fig. 4a, EI = 0.52 +/- 0.1, 0.62 +/- 0.1, 0.68 +/- 0.08, and 0.8 +/- 0.9 at 100 nM, 75 nM, 50 nM, and 25 nM respectively), indicating that lateral space taken up by the binding protein due to its footprint on the membrane, as well as its tilt and flexibility, reduces the space available for non-binding proteins. Proteins in the interface have been suggested to experience reduced entropy due to alignment and a reduction in tilt states[33], which could additionally influence the crowding-induced NBP exclusion.

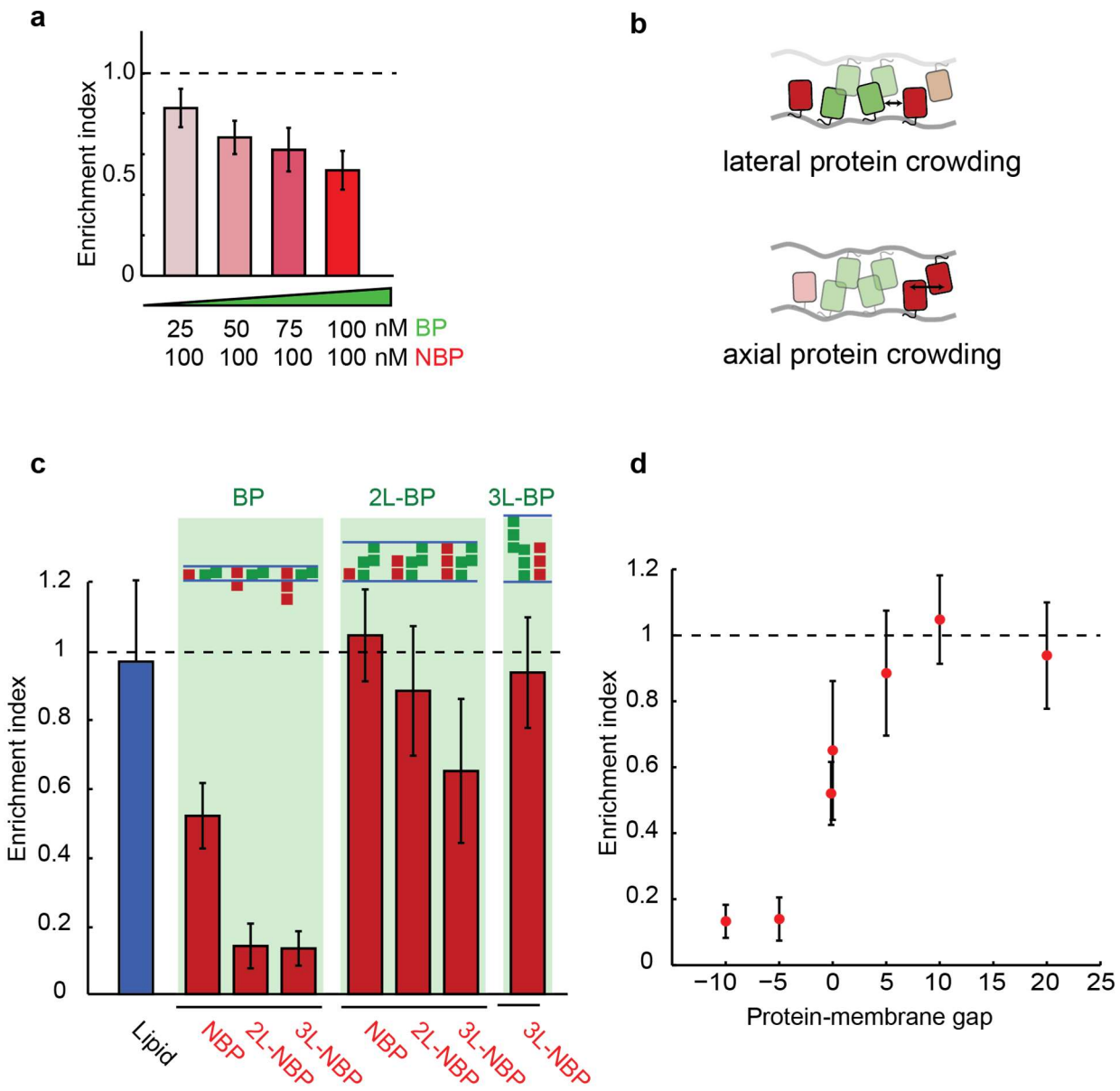

Figure 4: a, Single-length non-binding protein exclusion increases with increasing single-length binding protein concentration in solution. Error bars are standard error of the mean from three independent experiments on separate vesicle batches, each with ~50 vesicles quantified. **b**, Cartoon representation of lateral protein crowding (due to steric conflict with proteins on the same membrane) and axial protein crowding (due to steric conflict with proteins present on the opposite membrane). Lateral crowding of binding proteins, which depends on both protein footprint on the membrane and binding affinity, limits space available for non-binding proteins. **c**, Summary of measured non-binding protein exclusion for each pair of binding protein (BP, 2L-BP, 3L-BP) and non-binding protein (NBP, 2L-NBP, 3L-NBP), showing increases in exclusion with increases in non-binding protein size. **d**, Non-binding protein exclusion data is plotted as a function of the space between non-binding proteins and the apposing membrane (protein–membrane gap). A negative gap indicates the non-binding protein is larger than the average measured distance of the interface, whereas a positive gap indicates there is space

between the non-binding protein and the apposing membrane. Error bars are standard error of the mean from three independent experiments on separate vesicle batches, each with ~50 vesicles quantified.

Since lateral space at membrane interfaces is taken up not only by binding proteins but also by non-binding proteins on opposite membranes when the gap is small (Fig. 4b), we next investigated whether steric exclusion across membranes contributes to non-binding protein exclusion. To test for this, we increased the height of the binding protein to the double length binding protein (2L-BP, gap = 10.3 +/- 5.0 nm) while continuing to use the single length non-binding protein (NBP) on the two membranes. We found that NBP was no longer excluded from the interface (EI = 1.05 +/- 0.23) (quantification in Fig. 4b and confocal images in Supplementary Figure S5), consistent with reduced crowding from the single length non-binding protein on opposite membranes. Interestingly, we found that enrichment of the double length binding protein (2L-BP) in the membrane interface (EI = 1.28 +/- 0.28) was significantly less than that of the single length binding protein (BP) (EI = 3.55 +/- 1.7) (Fig. 4c; Supplementary Figure S4 and Supplementary Figure S5), likely because 2D affinity decreases with protein length[20,33], indicating that reduced crowding of the 2L-BP (from ~11,000 to ~3,000 molecules per um^2 at the interface, Supplementary Table) could also contribute to the lack of NBP exclusion.

To directly test whether steric interference of non-binding proteins from opposite membranes contribute to exclusion, we held the double length binding protein (2L-BP) constant and doubled the length of the non-binding protein to 2L-NBP (~9 nm), which is shorter than the measured membrane gap but tall enough to interact with non-binding proteins on the opposite membrane. Indeed, we found that the double length non-binding protein (2L-NBP) was excluded to a small but statistically significant amount (EI = 0.89 +/- 0.33), consistent with limited interaction between non-binding proteins in the opposite membrane (Fig. 4c). Increasing the length of the non-binding protein by ~4.5 nm to the triple length non-binding protein increased the exclusion (EI = 0.65 +/- 0.36) (Fig. 4c).

Overall, our experimental data show that a combination of changes in protein height and lateral crowding can titrate exclusion of non-binding proteins from membrane interfaces with only small changes in protein size. This can be seen more explicitly by re-plotting the data as a function of the difference between non-binding protein length and measured membrane gap size (set by the binding protein), which we refer to as protein-membrane gap (Fig. 4d, where 0 corresponds to non-binding protein size = membrane gap). To test in detail size-based mechanisms of protein exclusion and investigate the role of membrane properties, we turned to Monte Carlo simulations.

Monte Carlo simulations of size-dependent protein segregation

Monte Carlo models of membranes have been productively used to capture both membrane dynamics and spatial organization of adhesion proteins[20,36]. To explore the interplay between protein height, membrane gap, and lateral crowding at the interface, we developed a simulation of binding and non-binding protein segregation at membrane interfaces that includes as parameters the properties identified as important in our experimental work (non-binding protein height, binding protein height, protein lateral footprint, and protein density) and those that were

not easily accessible experimentally (membrane physical properties, binding protein affinity). To that end, we constructed a Monte Carlo simulation of a deformable, fluid membrane interface in which a fluctuating triangulated mesh represents each of the two membrane surfaces that form the interface, and nodes of the mesh can be occupied by diffusing proteins of defined height and binding potentials[36,37] (Fig. 5a, details in Methods). We seeded the membranes with a binding protein that defines a membrane gap size of 10 nm, comparable to the double length binding protein (2L-BP) interface, together with non-binding proteins of heights between 1 nm (protein-membrane gap = 9 nm) and 20 nm (protein-membrane gap = -10 nm).

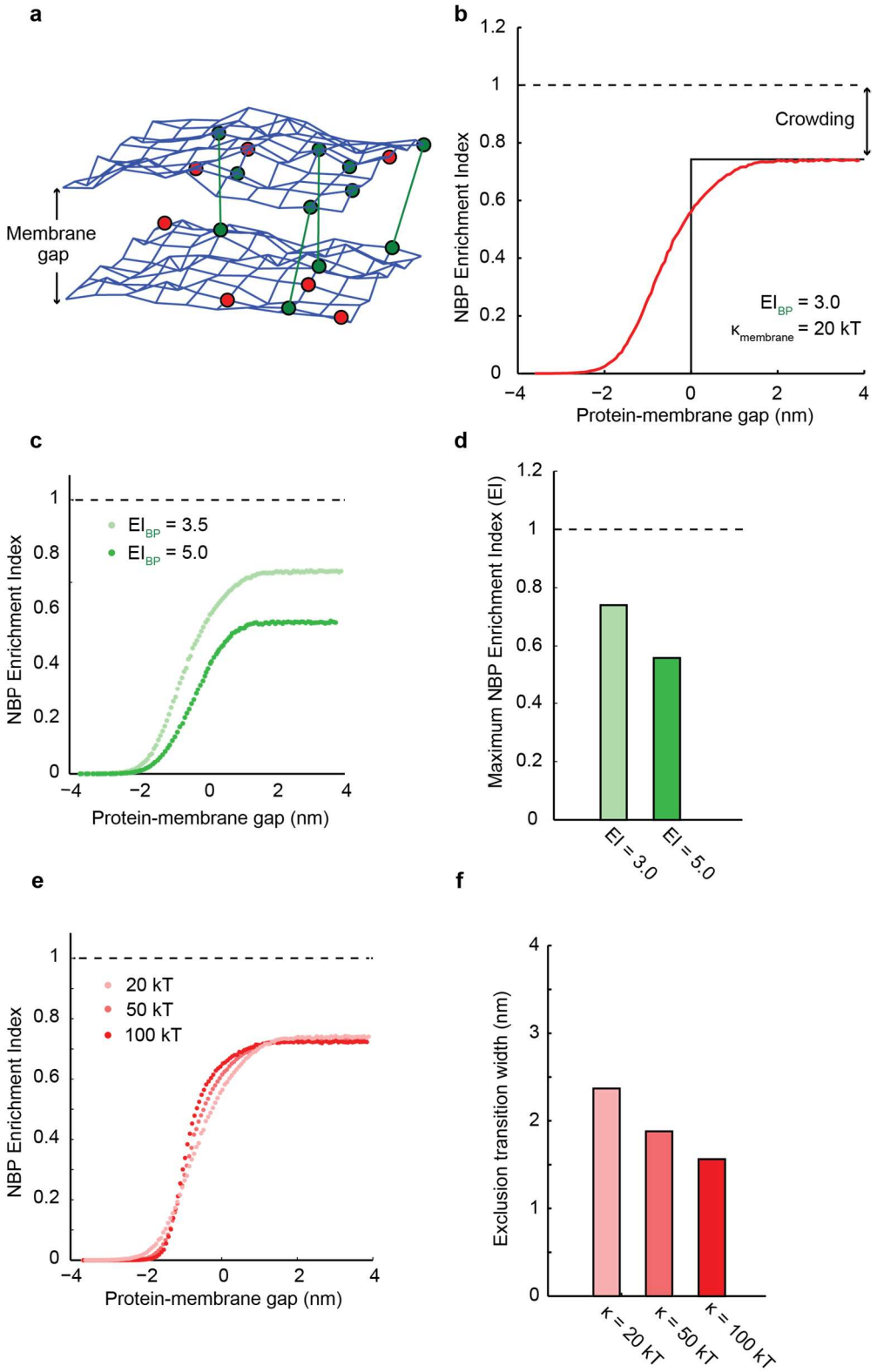

Figure 5: a, Single-length non-binding protein exclusion increases with increasing single-length binding protein concentration in solution. Error bars are standard error of the mean from three independent experiments on separate vesicle batches, each with ~50 vesicles quantified. **b**, Cartoon representation of lateral protein crowding (due to steric

conflict with proteins on the same membrane) and axial protein crowding (due to steric conflict with proteins present on the opposite membrane). Lateral crowding of binding proteins, which depends on both protein footprint on the membrane and binding affinity, limits space available for non-binding proteins. **c**, Summary of measured non-binding protein exclusion for each pair of binding protein (BP, 2L-BP, 3L-BP) and non-binding protein (NBP, 2L-NBP, 3L-NBP), showing increases in exclusion with increases in non-binding protein size. **d**, Non-binding protein exclusion data is plotted as a function of the space between non-binding proteins and the apposing membrane (protein–membrane gap). A negative gap indicates the non-binding protein is larger than the average measured distance of the interface, whereas a positive gap indicates there is space between the non-binding protein and the apposing membrane. Error bars are standard error of the mean from three independent experiments on separate vesicle batches, each with ~50 vesicles quantified.

Using parameters based on our experimental system, we found that non-binding protein exclusion varies sigmoidally as a function of the protein-membrane gap (Fig. 5b), consistent with our experimental observations (Fig. 4d). The simulations predict that proteins more than 2 nm taller than the membrane gap are fully excluded (EI = 0) from the interface, while proteins more than 2 nm shorter than the membrane gap are included to a level below full mixing (EI = 1) due to crowding, comparable to the effect of a ~4.5 nm change in protein height seen experimentally. Decreasing the binding protein density at the membrane interface by reducing its binding potential decreases the level of exclusion of non-binding proteins in the simulation (Fig. 5c, quantification in Fig. 5d), which is also consistent with our experiments (Fig. 4c and Supplementary Figure S4).

Increases in membrane bending rigidity from 20 kT to 100 kT in the simulation sharpened the transition between maximum exclusion and maximum inclusion of non-binding proteins (Fig. 5e, quantification in Fig. 5f), though the effect was not pronounced enough to be resolved in our experiments (Supplementary Figure S4). These results indicate that thermal fluctuations both make room for proteins taller than the membrane gap and exclude proteins shorter than the membrane gap, to a degree that is reduced with increasing bending rigidity. Interestingly, the small magnitude of membrane thermal fluctuations at even low membrane bending rigidities suggests that passive thermal fluctuations at crowded membrane interfaces may not be sufficient to bring a second species of short binding proteins into contact during cell-cell signaling, such as engagement of the peptide MHC-TCR (~13 nm) within a membrane interface formed by the comparatively longer LFA-ICAM adhesion (~40 nm)[2].

Discussion:

Our experiments and simulations show that protein size is a simple, sensitive, and highly effective means of altering local protein concentrations at membrane interfaces. Nanometer-scale changes in the height of non-binding proteins can dramatically change their densities at membrane interfaces, while high surface area coverage of binding proteins, which is dependent on both protein lateral footprint and binding affinity, can exclude non-binding proteins even when membrane gap size is not limiting. Our data and simulations show that increasing non-binding protein height has a large effect when it is comparable to membrane gap size (e.g. NBP to 2L-NBP in a BP interface) and a small effect when the protein height already exceeds the membrane gap size (e.g. 2L-NBP to 3L-NBP in a BP interface).

Given our finding that only ~5 nm increase in non-binding protein size is necessary for significant protein exclusion, the large length difference between CD45 isoforms (28 to 53 nm [22]) and the membrane interface gap size defined by TCR-pMHC binding (~13 nm [15]) is surprising and may not be necessary for exclusion. However, the active cytoskeletal processes that are involved in T-cell membrane reorganization and receptor engagement likely create a highly dynamic membrane interface with a variable protein-membrane gap size, for which extra non-binding protein length is needed to ensure exclusion. While T-cell receptors are at low abundance on a T-cell prior to cell-cell junction formation (100 molecules per μm^2), signaling occurs in micron-scale TCR micro-clusters that are highly enriched in TCRs and other membrane proteins, suggesting that lateral crowding may also be relevant for CD45 exclusion in the immunological synapse. More broadly, we believe that size-dependent protein segregation may be a general organizing mechanism at membrane interfaces. In fact, the dramatic size-diversity of membrane proteins may have evolved in order to influence cell-cell signaling. It is notable that many proteins on the extracellular surface of cells of multicellular eukaryotes, including CD45, contain several fibronectin type III (fn-3) or Immunglobulin (Ig) domains. Through these modular building blocks extracellular proteins are extended in height above the membrane from 5 to greater than 50 nm[39,40]. Interestingly, these domains have a size of ~4 nm, which in our experiments is the size difference needed to lead to complete exclusion from the interface. Therefore, adding or removing a single Ig domain may be sufficient to completely re-localize a protein from a membrane interface in the absence of active processes, a potentially powerful evolutionary tool.

We expect that the basic principles of protein segregation at membrane interfaces reported here are at work not only at cell-cell adhesions but also at intracellular membrane contact sites[41–43], where size-dependent enrichment and exclusion of proteins at interfaces can drive key steps in molecular sorting and signaling.

Methods:

Chemical reagents. Hepes (4-(2-hydroxyethyl)-1-piperazineethanesulfonic acid), MOPS (3-(N-morpholino)propanesulfonic acid), TCEP (*tris*(2-carboxyethyl)phosphine), KCl, glucose, sucrose, β-Mercaptoethanol, and imidazole were purchased from Fisher Scientific. EDTA (Ethylenediaminetetraacetic acid), was purchased from Acros Organics. Imidazole was purchased from Sigma Aldrich. Atto 390-DOPE was purchased from ATTO-TEC. DOGS-Ni-NTA (1,2-dioleoyl-*sn*-glycero-3-[(N-(5-amino-1-carboxypentyl)iminodiacetic acid)succinyl], with nickel salt) and DOPC (1,2-dioleoyl-*sn*-glycero-3-phosphocholine), were purchased from Avanti Polar Lipids (Alabaster, AL). All purchased chemical reagents were used without further purification.

Cloning, protein expression and purification. Standard methods of molecular biology, including reagents from Quiagen, Thermo Scientific and Zymo Research, were used to generate the following constructs. BP **(**GFPuv) and NBP (mCherry) variants were cloned into petMz backbone vector (a kind gift from Dr. Peter Bieling). We cloned combinations of dark mCherry (Y72S), mCherry and GFPuv fusions to generate our synthetic toolset of binding or non-binding membrane bound proteins of different sizes. For a list of all used proteins please see domain structures in Supplementary Figure S2. Multimers of mCherry/GFPuv were created by linking C

to N-termini via a 7 amino acid (GGGGSTS) linker. To render mCherry into a non-fluorescent dark mCherry we mutated tyrosine 72 into a serine by site-directed mutagenesis.
All proteins were expressed as a Deca-His-tag fusion proteins in BL21 (DE3) pLysS cells (Stratagene). Cells were grown at 37 °C until OD600 of 0.3 - 0.5, induced with 0.3 mM IPTG and grown for 14 - 16 h at 18 °C. Cells were harvested and resuspended in 25 mM Hepes, pH 7.4, 150 mM KCl, 1 mM TCEP and 10 mM Imidazole, and lysed by freeze thawing and sonication. The lysate was centrifuged for 45 min at 20,000 × g, 4 °C and affinity purified over a His-Trap HP or a Hi-Trap Chelating column HP (GE Healthcare), including extensive washing with 25 mM Hepes, pH 7.4, 150 mM KCl, 1 mM TCEP and 10-50 mM Imidazole, followed by Imidazole gradient elution on an AKTA Pure (GE Healthcare) system. Peak fractions were pooled and proteins were cleaved in elution buffer by incubation for 2 hours at room temperature and overnight at 4°C with His6-TEV protease (purchased from Macrolab at UC Berkeley). Proteins were buffer exchanged over PD-10 columns (GE Healthcare) into 25 mM Hepes, pH 7.4, 150 mM KCl, 1 mM TCEP. Protein solution was spun at 16,000 × g at 4deg C to remove aggregated His-6 TEV protease and supernatant was rebound to the chelating column to remove the non-his-tagged z-tag. After imidazole gradient elution on the AKTA PURE system, protein was concentrated and gelfiltered via a Superdex 200 column in 25 mM Hepes, pH 7.4, 150 mM KCl, 1 mM TCEP. Proteins were concentrated, aliquoted and snap frozen. Purity was assessed via SDS PAGE.

GUV preparation. Electroformation of giant unilamellar vesicles (GUVs) was performed according to published protocols[44]. To ensure mixing of all lipid components we performed electroformation at approximately 55 °C. Vesicles were electroformed in solution containing approximately 350 mM sucrose (~350 mOsm). Lipid composition was kept constant in all our experiments with 97.5% DOPC and 2.5 % DOGS-Ni-NTA. 0.3% Atto 390-DOPE dye was used as a membrane where indicated.

Preparation and characterization of protein-coated GUVs. After electroformation, vesicles were diluted, exposed to proteins, and prepared for imaging. 1 ul GUVs were gently transferred to a home-made Polydimethylsiloxane (PDMS, Sylgard) chamber containing 100 ul of protein solution (in 25 mM Hepes buffer with 150 mM KCl and 1mM TCEP, osmotically balanced to 320 mOsm). The mixture was incubated on room temperature for 10 minutes and imaged immediately thereafter.
To avoid complications of dimer formation in solution we used protein concentrations at least 200 fold below the dimer Kd. Using fluorescence correlation spectroscopy (FCS) of supported bilayers having the same composition (for FCS and supported bilayers see Methods sections below and Supplementary Figure S1), we measured a lateral protein density of 2,317 +/- 370 molecules per um^2 for these conditions. Given an estimated footprint of ~ $(4\ nm)^2$ for GFPuv, this protein density corresponds to 3.8% membrane area coverage by protein. For each GFPuv at this density there are ten DOGS-Ni-NTA lipids available, leading to nearly irreversible protein-to-membrane attachment[32]. Interface size and shape was equilibrated rapidly (within 2 minutes), consistent with fast protein diffusion on the GUV membranes. No nonspecific binding of GFPuv to membranes lacking DOGS-Ni-NTA was observed (see Supplementary Figure S2). Wildtype GFP (dimerization kD: 110uM [46]), formed only very weak interfaces which showed only minimal protein enrichment.

Imaging. GUVs were imaged on a spinning disc confocal microscope (AxioObserverZI, Zeiss, with motorized nosepiece and spinning disk confocal, Yokogawa CSU-10) for confocal microscopy with a cooled EMCCD camera (Cascade II, Photometrics). Images were acquired using a 63x objective (Zeiss, Plan Apochromat 1.4 NA, oil), and analyzed using ImageJ (National Institutes of Health) and Matlab (Mathworks).

Image analysis. Vesicle dimers were localized within spinning disk confocal images and line scans were drawn to cross both vesicles and the vesicle interface using ImageJ (NIH). An intensity trace across the length of the line scan was extracted from the confocal images after background subtraction using a custom Matlab script (Mathworks). The three intensity peaks, corresponding to each of the two vesicles and the vesicle interface, were localized using a peak finding algorithm, and the intensity values from these peaks were used to compute the EI.

Supported Lipid Bilayer (SLB) Preparation. SLBs were formed by fusion of small unilamellar vesicles (SUVs) on RCA cleaned glass coverslips. SUVs were prepared from a lipid film composed of 97.5% DOPC and 2.5 % DOGS-Ni-NTA rehydrated in buffer containing 25 mM MOPS and 125 mM NaCl at pH 7.4. The rehydrated solution was freeze-thawed in liquid nitrogen and agitated using a high-power bath sonicator (Avanti), then filtered through a 200 nm filter (Millipore) to select for SUVs. A solution of SUVs was incubated in a home-made Polydimethylsiloxane (PDMS, Sylgard) well chamber above a clean glass coverslip for 10 minutes, then washed with MOPS buffer 10 times to remove excess SUVs from solution. Lipid bilayers were tested for fluidity after binding proteins to DOGS-Ni-NTA lipid by photo-bleaching a small region and monitoring for rapid recovery.

Distance measurement preparation. SLBs were incubated with 100 nM protein (BP, 2L-BP, 3L-BP) in the presence of GUVs to coat both the planar and vesicle membranes. GUVs settled onto the planar membrane, and binding between proteins on the SLB and GUV results in the formation of a flattened membrane-membrane interface at the base of the GUV.

Quantitative distance measurement by Reflection Interference Contrast Microscopy (RICM). Narrow-band illumination light (546 nm) selected from a mercury arc lamp (Excite) was directed through an anti-flex (EC-Plan Neofluor 63x, NA 1.25) through a crossed linear polarizing cube. A reflected light interference-contrast image was formed, such that image contrast was a function of the distance between the SLB and the bottom surface of the GUV as well as the refractive index difference at the glass-media and media-GUV interfaces. The RICM images were processed using a method previously described to extract the axial distance between the two membranes with a precision of a few nanometers[30]. Briefly, the SLB-GUV interface was modeled as a multi-layer film consisting of the following layers: glass (N=5.0), lipid (N=4.2), buffer (N=3.0, h=variable), lipid (N=4.2), sucrose (N=2.0), where the height of each lipid layer was the thickness of a typical bilayer (5.0 nm) and the buffer layer (N=3.0) was of variable axial extent. The theoretical contrast as a function of the height of the variable buffer layer, which corresponds to the distance between SLB and the bottom surface of the GUV, was calculated. RICM contrast images of the SLB-GUV interface were processed using custom Matlab scripts to extract the radially averaged intensity as a function of distance from the center of the interface. This function was used to determine the minimum and maximum of the first periodic interference fringe, and the average contrast of the flattened GUV-SLB interface area was

normalized with these extrema. This normalized interface contrast was mapped to the theoretical contrast function to determine the best-fit height of the buffer layer, and thus the separation between SLB and GUV imposed by the adhesive proteins (Supplementary Figure S3).

FCS. Fluorescence correlation spectroscopy experiments are performed on a custom-built setup based around a Nikon Eclipse TE2000 microscope body (Nikon). A 488 nm CW laser was used as an excitation source (Sapphire, Coherent). Photons counts were detected with an avalanche photo diode (SPCM-AQR-14, Excelitas), and photon arrival times were registered by the counter module of an NI DAQ board (PCI-6321, National Instruments). Autocorrelation analysis and data fitting were performed by custom written Matlab scripts (Mathworks). Experiments were carried out with a 100x oil immersion objective (NA 1.49). On each measurement day, an autocorrelation measurement from a 50nM solution of Fluorescein was acquired to calibrate the focal volume of the system. SLBs were incubated with a mixture of GFPuv and a mutated dark GFPuv (Y66S) at a 7% ratio, such that the concentration of fluorescent molecules on the SLB was within the range needed for FCS. To measure the density of molecules on the SLB, photon arrival times were recorded for periods of 10 seconds, with 6 independent measurements performed per bilayer (for a total acquisition time of 60 seconds per bilayer). An autocorrelation was performed on the photon arrival record, and the resulting curve was fit to a model of single-component two-dimensional diffusion[47]. The value of G(0) was extrapolated from the fit, and the concentration of fluorescent molecules on the bilayer was expressed as $(G(0)*A_{eff})^{-1}$, where A_{eff} is the area defined by the confocal observation volume. Concentration measurements were repeated for 5 independent SLBs.

Estimates of protein density and membrane coverage. To estimate the density of molecules on the membrane for each BP species, we used the FCS measurements of protein density for GFPuv (BP, in molecules/um^2) along with the fluorescence intensity (in arbitrary units) from confocal images of GUVs to compute a scaling factor between arbitrary fluorescence units and molecular density (AU to molecules/um^2). The fluorescence emission from each (BP, 2L-BP, 3L-BP) molecule is expected to be equivalent because each species contains a single fluorescent GFPuv module. This scaling factor is used to compute molecular density for both 2L-BP and 3L-BP. The molecular density at the interface for BP, 2L-BP, and 3L-BP is estimated by multiplying the density on the vesicle with the enrichment index of the binding protein. The area of membrane covered by protein is estimated using a footprint of $(4\ nm)^2$ for both binding proteins and non-binding proteins.

Generation of protein-membrane gap curve in Fig. 4b. To compute the protein-membrane gap, we used estimates of non-binding protein height based on crystal structure (NBP = 5 nm, 2L-NBP = 10 nm and 3L-NBP = 15 nm) and equivalent estimates of interface distance imposed by BPs (BP dimer = 5.0 nm, 2L-BP dimer = 15.0 nm and 3L-dimer 25.0 nm). These values are in the range of interface distance measured by RICM. The protein-membrane gap is the difference between the interface distance imposed by BPs and the size of the NBP.

Monte Carlo simulation model. We are simulating two adjacent quasi-flat periodic membrane interfaces employing a Metropolis Monte Carlo (MC) method based on a dynamically triangulated surface model for fluctuating fluid membranes. The bending energy of the membrane is calculated using a discretized version of the Laplacian on the triangulated lattice at constant bending

rigidity[48]. During the initialization procedure, the area (i.e. number of vertices in the triangulation) of a single bare membrane patch is equilibrated using a grand canonical MC move. Afterwards, a vertically translated copy of the resulting membrane patch is created and the number of membrane vertices is kept constant throughout the simulation. Initially, the two membrane surfaces are placed at a relative height that corresponds to the linker rest length l of the bound BP complex in simulation and all membrane vertices are populated by BP and linked pairwise. An additional MC move attempts to (un-)bind pairs of BP across the two lattices incorporating a constant binding energy 4.5kT and a harmonic linker potential of given rest length l=10nm and spring constant 20kT/nm² between the two. The density of unbound BP and NBP is equilibrated using a grand canonical MC move that inserts and subtracts these particle species within the membrane lattice at a constant chemical potential that corresponds to a protein-membrane lattice coverage of 0.1 within the implicit reservoir outside the bound membrane interface. After equilibration, fluctuating protein densities of BP (bound and unbound) and NBP are monitored. The linear length of the projected quadratic membrane area is 200nm, while the maximum length of the purely entropic membrane-internal linkers is 9.5 nm. Membrane vertices interact with themselves and other protein species on apposing membranes via steric interactions. The hard-sphere node diameter is constant at d_{mem}=5nm for the bare membrane and at BP = 10nm for vertices occupied by BP. The NBP diameter is varied in the range 5nm ≤ dNBP ≤ 20nm. The corresponding gap size for plotting NBP exclusion curves is calculated as the average distance between membranes in simulation.

Supplemental Figures:

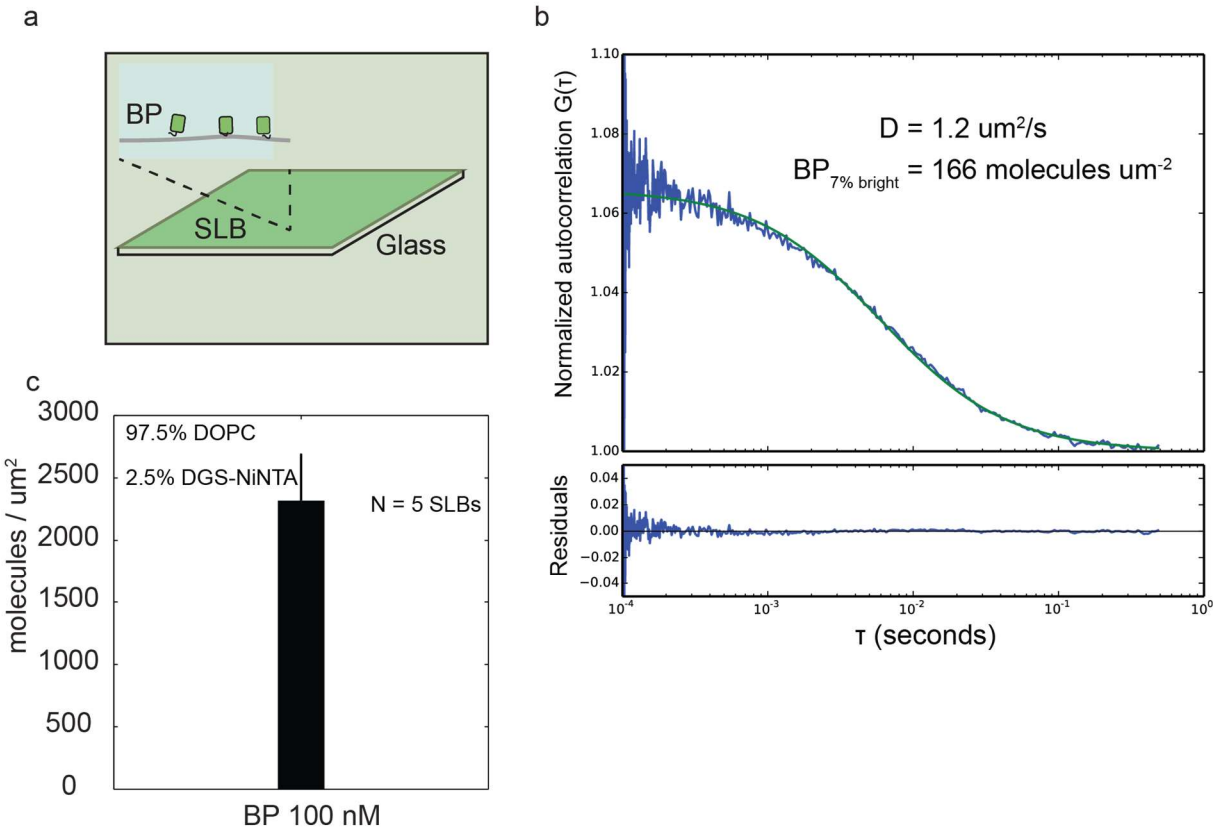

Figure S1: (a) Glass supported lipid bilayers (SLBs, composition: 94.5% DOPC, 2.5% DOGS-NiNTA) are incubated 100 nM BP solution for 10 minutes. (b) The density of BP protein on the SLB is measured by FCS. 7% fluorescent GFPuv (BP) was mixed with 93% mutated non-fluorescent GFPuv (BP-Y66S) (7% bright) to achieve the correct concentration range for FCS measurements. Normalized autocorrelation curves were fit with a single component two-dimensional diffusion model to extract the diffusion coefficient and protein density of the BP (molecules/µm2) (c) Measurements on 5 independent SLBs reveal an BP density of 2,317 +/- 370 molecules/um2 for an SLB with 2.5% DOGS-NiNTA incubated with 100 nM BP protein.

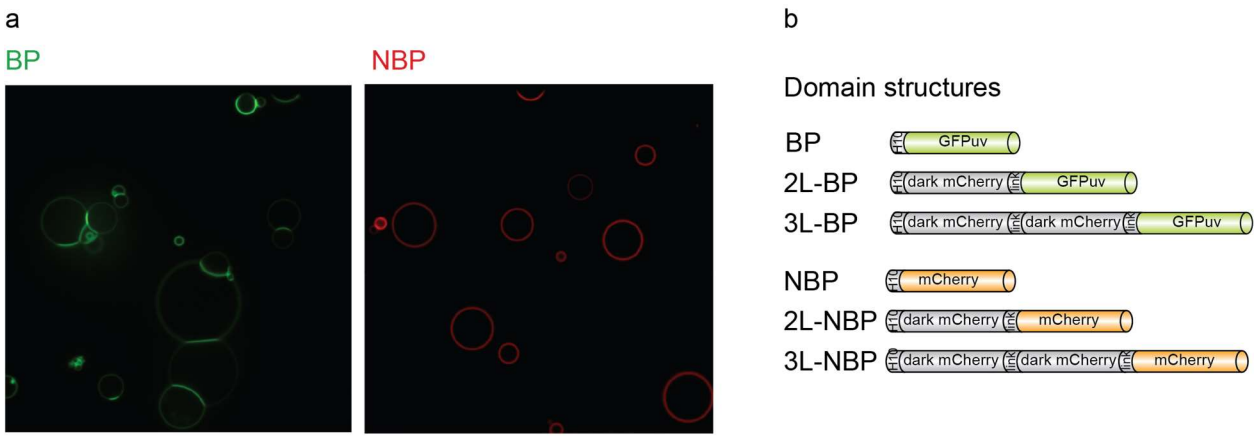

Figure S2: (a) Representative field of view of BP (green) and NBP (red) bound to DOGS-Ni-NTA containing GUV membranes (composition: 97.5% DOPC, 2.5% DOGS-Ni-NTA incubated with 100 nM protein solution for 10 min). Note how BP molecules form GUV interfaces while NBP molecules do not. Scale bar is 20 µm long. (b) A mixture of GUVs with His-tagged protein binding capability (97.5% DOPC, 2.5% DOGS-Ni-NTA) and GUVs lacking DOGS-Ni-NTA (99.7% DOPC, 0.3% Atto647-DOPE) were incubated with 100 nM GFPuv (BP). BP only bound to DOGS-Ni-NTA containing vesicles, confirming that there is no non-specific binding of BP from solution to membranes. Furthermore, we could not detect unspecific interface formation between BP-covered GUVs and proteinfree GUVs. All scale bars are 10 µm. (c) Protein domain architectures illustrate proteins used in this study.

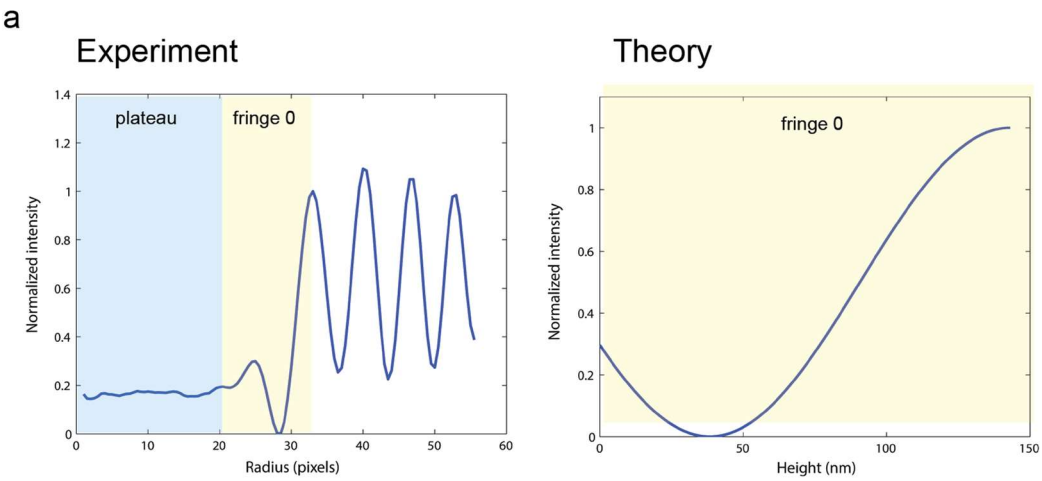

Figure S3: (left) Radially averaged RICM contrast as a function of the distance from the center of the GUV. (right) Theoretical RICM contrast as a function of the height of the variable buffer layer, which corresponds to the distance between SLB and the bottom surface of the GUV (see Methods).

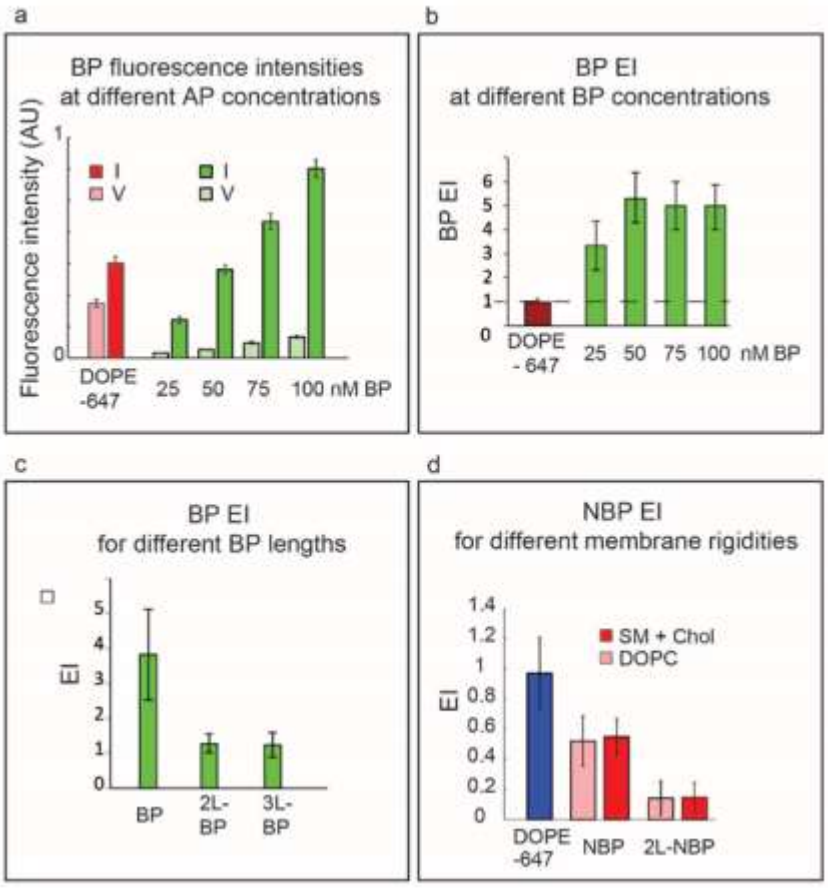

Figure S4: (a) Increasing concentrations of BP in solution leads to increased fluorescence intensities on GUVs. Vesicle (V) fluorescence intensities are plotted versus interface (I) intensities. (b) EIs for BP at different protein concentrations in solution. We note that while the intensities in a) scale with concentration, protein distribution over the vesicles stays remarkably constant at different protein densities. (c) EI values for different lengths adhesion molecules averaged over all experiments. Single lengths BP enrich more at the interface possibly due to higher 2D affinity than the longer 2L-BP and 3L-BP. (d) Exclusion of NBP or 2L-NBP from BP interfaces does not change significantly with increased membrane rigidity. GUVs from 80% Sphingomyelin and 20% Cholesterol mixtures (SM + Chol) have a approximately 6 fold higher bending rigidity than the DOPC GUVs. SM+Chol (77.5% Brain Sphingomyelin (Avanti), 20% Cholesterol (Avanti) 2.5 % DOGS Ni-NTA) GUVs were incubated with 100 nM BP and 100 nM NBP or 2L-NBP. Interface formation and NBP and 2L NBP exclusion did not differ significantly from the same experiment performed on DOPC (97.5 % DOPC, 2.5% DOGS-NiNTA) vesicles.

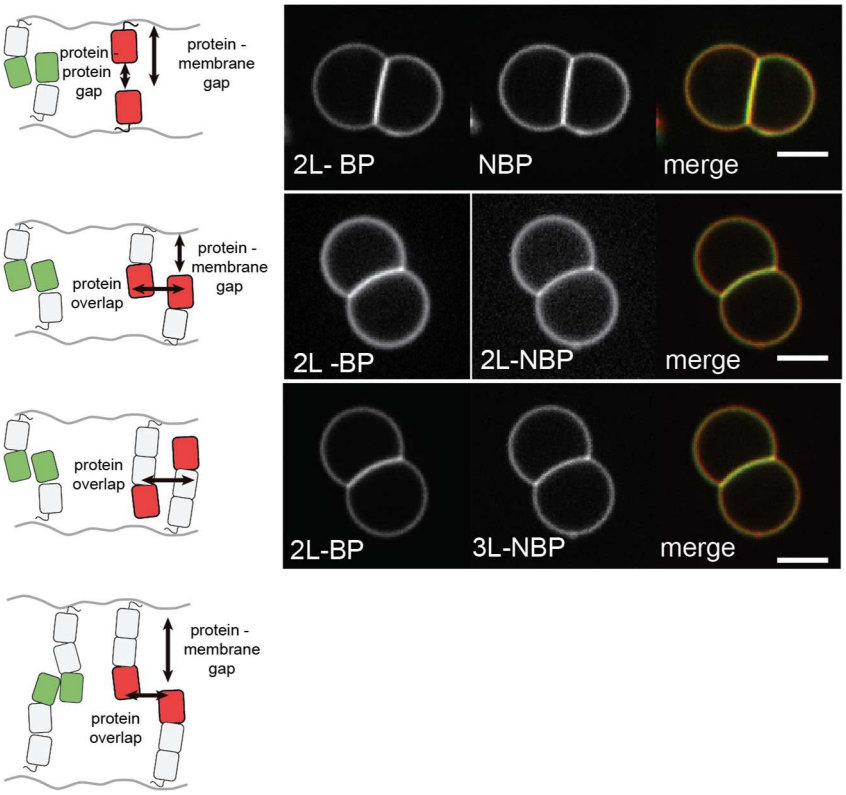

Figure S5: Representative confocal images for data in Fig. 4a. Increasing the size of the adhesive protein (2L-BP, 3L-BP) leads to decreased exclusion of NBP variants from interfaces. Representative confocal fluorescence images of GUVs (composition: 97.5% DOPC, 2.5% DOGS-Ni-NTA) incubated with 100 nM BP variants and 100 nM NBP variants in solution for 10 min. Scale bars are 5 μm long (green channel: BP, red channel: NBP). Error bars are standard error of the mean from three independent experiments on separate vesicle batches, each with ~50 vesicles categorized.

References

1. Bell, G. I. Models for the specific adhesion of cells to cells. *Sci. N. Y. NY* **200,** 618–627 (1978).

2. Dustin, M. L. The immunological synapse. *Arthritis Res. Ther.* **4,** S119–25 (2002).

3. Rochlin, K., Yu, S., Roy, S. & Baylies, M. K. Myoblast fusion: When it takes more to make one. *Dev. Biol.* **341,** 66–83 (2010).

4. Adams, C. L., Chen, Y. T., Smith, S. J. & Nelson, W. J. Mechanisms of epithelial cell-cell adhesion and cell compaction revealed by high-resolution tracking of E-cadherin-green fluorescent protein. *J. Cell Biol.* **142,** 1105–1119 (1998).

5. Goodridge, H. S. *et al.* Activation of the innate immune receptor Dectin-1 upon formation of a 'phagocytic synapse'. *Nature* **472,** 471–475 (2011).

6. Aricescu, A. R. *et al.* Structure of a tyrosine phosphatase adhesive interaction reveals a spacer-clamp mechanism. *Science* **317,** 1217–1220 (2007).

7. Monks, C. R., Freiberg, B. A., Kupfer, H., Sciaky, N. & Kupfer, A. Three-dimensional segregation of supramolecular activation clusters in T cells. *Nature* **395,** 82–86 (1998).

8. Dustin, M. L. Making a little affinity go a long way: a topological view of LFA-1 regulation. *Cell Adhes. Commun.* **6,** 255–262 (1998).
9. Grakoui, A. *et al.* The immunological synapse: a molecular machine controlling T cell activation. *Sci. N. Y. NY* **285,** 221–227 (1999).
10. Bunnell, S. C. *et al.* T cell receptor ligation induces the formation of dynamically regulated signaling assemblies. *J. Cell Biol.* **158,** 1263–1275 (2002).
11. Varma, R., Campi, G., Yokosuka, T., Saito, T. & Dustin, M. L. T cell receptor-proximal signals are sustained in peripheral microclusters and terminated in the central supramolecular activation cluster. *Immunity* **25,** 117–127 (2006).
12. James, J. R. & Vale, R. D. Biophysical mechanism of T-cell receptor triggering in a reconstituted system. *Nature* **487,** 64–69 (2012).
13. Cordoba, S.-P. *et al.* The large ectodomains of CD45 and CD148 regulate their segregation from and inhibition of ligated T-cell receptor. *Blood* **121,** 4295–4302 (2013).
14. Siu, G., Springer, E. A. & Hedrick, S. M. The biology of the T-cell antigen receptor and its role in the skin immune system. *J. Invest. Dermatol.* **94,** 91S–100S (1990).
15. Davis, S. J. & van der Merwe, P. A. CD2: an exception to the immunoglobulin superfamily concept? *Sci. N. Y. NY* **273,** 1241–1242 (1996).
16. Choudhuri, K., Wiseman, D., Brown, M. H., Gould, K. & van der Merwe, P. A. T-cell receptor triggering is critically dependent on the dimensions of its peptide-MHC ligand. *Nature* **436,** 578–582 (2005).
17. Bethani, I., Skaanland, S. S., Dikic, I. & Acker-Palmer, A. Spatial organization of transmembrane receptor signalling. *EMBO J.* **29,** 2677–2688 (2010).
18. Li, P. *et al.* Phase transitions in the assembly of multivalent signalling proteins. *Nature* **483,** 336–340 (2012).
19. Sheetz, M. P., Sable, J. E. & Döbereiner, H.-G. Continuous membrane-cytoskeleton adhesion requires continuous accommodation to lipid and cytoskeleton dynamics. *Annu. Rev. Biophys. Biomol. Struct.* **35,** 417–434 (2006).
20. Weikl, T. R., Asfaw, M., Krobath, H., Rózycki, B. & Lipowsky, R. Adhesion of membranes via receptor–ligand complexes: Domain formation, binding cooperativity, and active processes. *Soft Matter* **5,** 3213–12 (2009).
21. Milstein, O. *et al.* Nanoscale increases in CD2-CD48-mediated intermembrane spacing decrease adhesion and reorganize the immunological synapse. *J. Biol. Chem.* **283,** 34414–34422 (2008).
22. Alakoskela, J.-M. *et al.* Mechanisms for Size-Dependent Protein Segregation at Immune Synapses Assessed with Molecular Rulers. *Biophys. J.* **100,** 2865–2874 (2011).
23. McCall, M. N., Shotton, D. M. & Barclay, A. N. Expression of soluble isoforms of rat CD45. Analysis by electron microscopy and use in epitope mapping of anti-CD45R monoclonal antibodies. *Immunology* **76,** 310–317 (1992).

24. Rózycki, B., Lipowsky, R. & Weikl, T. R. Segregation of receptor–ligand complexes in cell adhesion zones: phase diagrams and the role of thermal membrane roughness. *New J. Phys.* **12,** 095003–22 (2010).
25. Burroughs, N. J. *et al.* Boltzmann Energy-based Image Analysis Demonstrates that Extracellular Domain Size Differences Explain Protein Segregation at Immune Synapses. *PLoS Comput. Biol.* **7,** e1002076–11 (2011).
26. Hu, J., Lipowsky, R. & Weikl, T. R. Binding constants of membrane-anchored receptors and ligands depend strongly on the nanoscale roughness of membranes. *Proc. Natl. Acad. Sci. U. S. A.* **110,** 15283–15288 (2013).
27. Phillips, G. N. Structure and dynamics of green fluorescent protein. *Curr. Opin. Struct. Biol.* **7,** 821–827 (1997).
28. CLONTECH Laboratories, Inc. Living Colors, Clontech User Manual. 1–51 (1998).
29. Rudolph, M. G., Luz, J. G. & Wilson, I. A. Structural and thermodynamic correlates of T cell signaling. *Annu. Rev. Biophys. Biomol. Struct.* **31,** 121–149 (2002).
30. Quinn, P., Griffiths, G. & Warren, G. Density of newly synthesized plasma membrane proteins in intracellular membranes II. Biochemical studies. *J. Cell Biol.* **98,** 2142–2147 (1984).
31. Takamori, S. *et al.* Molecular anatomy of a trafficking organelle. *Cell* **127,** 831–846 (2006).
32. Theodoly, O., Huang, Z.-H. & Valignat, M.-P. New modeling of reflection interference contrast microscopy including polarization and numerical aperture effects: application to nanometric distance measurements and object profile reconstruction. *Langmuir ACS J. Surf. Colloids* **26,** 1940–1948 (2010).
33. Yang, F., Moss, L. G. & Phillips, G. N. The molecular structure of green fluorescent protein. *Nat. Biotechnol.* **14,** 1246–1251 (1996).
34. Krobath, H., Rózycki, B., Lipowsky, R. & Weikl, T. R. Line Tension and Stability of Domains in Cell-Adhesion Zones Mediated by Long and Short Receptor-Ligand Complexes. *PLoS ONE* **6,** e23284 (2011).
35. Wu, Y., Vendome, J., Shapiro, L., Ben-Shaul, A. & Honig, B. Transforming binding affinities from three dimensions to two with application to cadherin clustering. *Nature* **475,** 510–513 (2011).
36. Müller, M., Katsov, K. & Schick, M. A new mechanism of model membrane fusion determined from Monte Carlo simulation. *Biophys. J.* **85,** 1611–1623 (2003).
37. Ho, J.-S. & BAUMGARTNER, A. Simulations of Fluid Self-Avoiding Membranes. *Europhys. Lett.* **12,** 295–300 (1990).
38. Gompper, G. & Kroll, D. M. Network models of fluid, hexatic and polymerized membranes. *J. Phys. Condens. Matter Inst. Phys. J.* 8795–8834 (1997).
39. Teichmann, S. A. & Chothia, C. Immunoglobulin superfamily proteins in Caenorhabditis elegans. *J. Mol. Biol.* **296,** 1367–1383 (2000).

40. Vogel, C. The immunoglobulin superfamily in Drosophila melanogaster and Caenorhabditis elegans and the evolution of complexity. *Dev. Camb. Engl.* **130,** 6317–6328 (2003).
41. Helle, S. C. J. *et al.* Organization and function of membrane contact sites. *BBA - Mol. Cell Res.* **1833,** 2526–2541 (2013).
42. Kornmann, B. The molecular hug between the ER and the mitochondria. *Curr. Opin. Cell Biol.* **25,** 443–448 (2013).
43. Martens, S. & McMahon, H. T. Mechanisms of membrane fusion: disparate players and common principles. *Nat. Rev. Mol. Cell Biol.* **9,** 543–556 (2008).
44. Angelova, M. I. & Dimitrov, D. S. Liposome electroformation. *Faraday Discuss. Chem. Soc.* **81,** 303 (1986).
45. Nye, J. A. & Groves, J. T. Kinetic control of histidine-tagged protein surface density on supported lipid bilayers. *Langmuir ACS J. Surf. Colloids* **24,** 4145–4149 (2008).
46. Zacharias, D. A., Violin, J. D., Newton, A. C. & Tsien, R. Y. Partitioning of lipid-modified monomeric GFPs into membrane microdomains of live cells. *Sci. N. Y. NY* **296,** 913–916 (2002).
47. Krichevsky, O. & Bonnet, G. Fluorescence correlation spectroscopy: the technique and its applications. *Rep. Prog. Phys.* **65,** 251–297 (2002).
48. Gompper, D. M. K. G. Random Surface Discetizations and the Renormalization of the Bending Rigidity. *J Phys Fr.* **6,** 1305–1320 (1996).

Chapter 3

Antigen height modulates antibody-dependent macrophage phagocytosis through size-dependent signaling

Ari Joffe, Marija Podolski, and Eva Schmid contributed to this chapter.

Abstract

Macrophages protect the body from damage and disease by targeting antibody-opsonized cells for phagocytosis. Phagocytosis is mediated through activation of Fc receptors upon ligation with a surface-bound antibody, but it remains unclear how receptor-antibody binding triggers phosphorylation of the receptor, or how Fc receptors can accommodate the variable binding geometries formed by antigens with diverse structure, shape, and size. To determine the influence of antigen height on antibody-dependent phagocytosis, we reconstituted a minimal model of a target cell surface using lipid-bilayer coated glass beads and protein antigens with height-specific antibody binding sites. We find that phagocytosis is dramatically impaired for antigens that position an antibody > 10 nm from the target surface, including the tall colorectal-cancer antigen CEACAM5. Imaging at the macrophage-target interface revealed decreasing receptor phosphorylation for tall antigens as well as segregation of the inhibitory phosphatase CD45 from Fc receptor micro-clusters, both in a size-dependent manner. Our findings suggest that close contact (< 10 nm) between a macrophage and target cell is a requirement for triggering of Fc receptors, which has implications for the design of therapeutic monoclonal antibodies to stimulate immune effector cells.

Introduction

Controlled activation of immune cells protects the body from pathogens and disease while limiting damage to healthy-self. Antibodies provide control over an immune response by targeting cells displaying foreign antigens for destruction by phagocytes and other innate immune cells. Macrophages rely on antibody-dependent phagocytosis (ADP) to destroy bacterial and fungal pathogens as well as infected self-cells, and recently ADP has been shown to contribute to anti-tumor immunity during monoclonal antibody therapy[1–3].

Antibody-dependent phagocytosis is triggered by binding between the Fc region of IgG and macrophage Fcγ receptors (FcγRs), but the mechanism of FcγR activation remains a subject of study. In particular, the role that physical changes in signaling molecules or their organization play in activation is unclear. Unlike toll-like receptors, which dimerize upon ligand binding, a one-to-one binding stoichiometry between FcγR and IgG precludes a mechanism requiring ligand-induced dimerization, and there is no evident conformational change in FcγR upon binding[4,5]. Instead, it has been suggested that clustering of multiple FcγRs on the fluid plasma membrane is necessary for receptor activation[6]. It is known that phosphorylation of the FcγR ITAM is controlled by a balance of Src family kinase (SFK) and tyrosine-phosphatase activity, and that a phosphorylated ITAM required for activation and phagocytosis, but how clustering might lead to phosphorylation of the ITAM remains unclear[7,8]

The requirements for FcγR signaling differ from other immune-receptors in an important way: because IgG is bound to an unknown antigen, there is no uniform geometry or orientation for the IgG-FcγR complex relative to the target cell-surface. Antigens are physically diverse, with different structure, shape, and size. For instance, members of the CEACAM family of cell-surface receptors, composed of 1-7 Ig-like domains, are expressed differentially during cancer progression[9]. Whether and how macrophages might accommodate this variability has

implications for the development of therapeutic antibodies, which could have decreased effectiveness if antigen height impacts FcγR signaling and phagocytosis (Figure 1a).

One way in which height could influence signaling is based on the kinetic segregation model, which has been studied in the context of the T-cell receptor (TCR). Like FcγR, TCR signals through ITAM motifs and hinges on a balance of Src family kinase (SFK) and tyrosine-phosphatase activity[10,11]. The kinetic segregation model of TCR signaling proposes that due to their large extracellular domains, the phosphatases CD45 and CD148 are physically excluded from sites of TCR-pMHC binding, which locally decreases phosphatase activity around the TCR leading to phosphorylation and activation of the receptor[12–15]. It has been suggested that a similar size-dependent mechanism of phosphatase segregation at close contacts between a macrophage and a target cell may trigger FcγR activation[6,16]. However, signaling through FcγR might also depend on establishment of a diffusion barrier by integrin binding, or concentration of SFKs along with FcγR in lipid micro-domains[17,18].

Here we show that FcγR signaling and phagocytosis is critically dependent on the height of an antibody above the target cell surface. Using reconstituted target particles with variable height antigens, we find that physical segregation of large phosphatases is necessary for signaling, and that segregation is disrupted by binding through antibodies bound to antigen-epitopes that are > 10 nm from the target-cell surface. We also find that this size dependence holds true for the tumor-expressed CEACAM antigens. Our findings suggest that therapeutic antibodies intended to direct antibody-dependent cellular-phagocytosis (ADCP) would be most productively targeted to antigens or antigen domains that are within 10 nm from the cell surface.

Results

Reconstitution of a target membrane for FcγR dependent phagocytosis

Antibody-dependent phagocytosis against cellular targets with diverse proteins, glycans, and lipids on the cell-surface involves binding through multiple pattern-recognition receptors in addition to FcγR[19] (Figure 1a). In order to isolate the mechanism of FcγR signaling, we reconstituted a simplified model of a target-cell surface *in vitro*, consisting of glass micro-beads coated with a fluid supported-lipid bilayer (SLB) (Figure 1b). Lipids with a biotinylated head-group can be incorporated into the membrane as a model of a lipid-bound antigen, providing a target for opsonization with an anti-biotin IgG1 antibody; the biotin targeted IgG1 is able to diffuse fluidly on the membrane surface, similar to an antibody bound to a diffusible mammalian cell-surface antigen. To stimulate phagocytosis, SLB-coated beads were added to an imaging chamber seeded with RAW 264.7 macrophages. Upon contact between an opsonized target and a macrophage we observed a striking enrichment of labeled anti-biotin IgG1 at the macrophage-target interface, consistent with binding between the surface-bound IgG and macrophage Fc receptors, and with the capture of the antibody-FcγR complex at the contact interface (Figure 1b). The lipid surface effectively passivates the targets; we observed little to no internalization of non-opsonized targets, and we found that macrophages are capable of eating multiple beads per cell in an IgG1-dependent manner (Figure 1c).

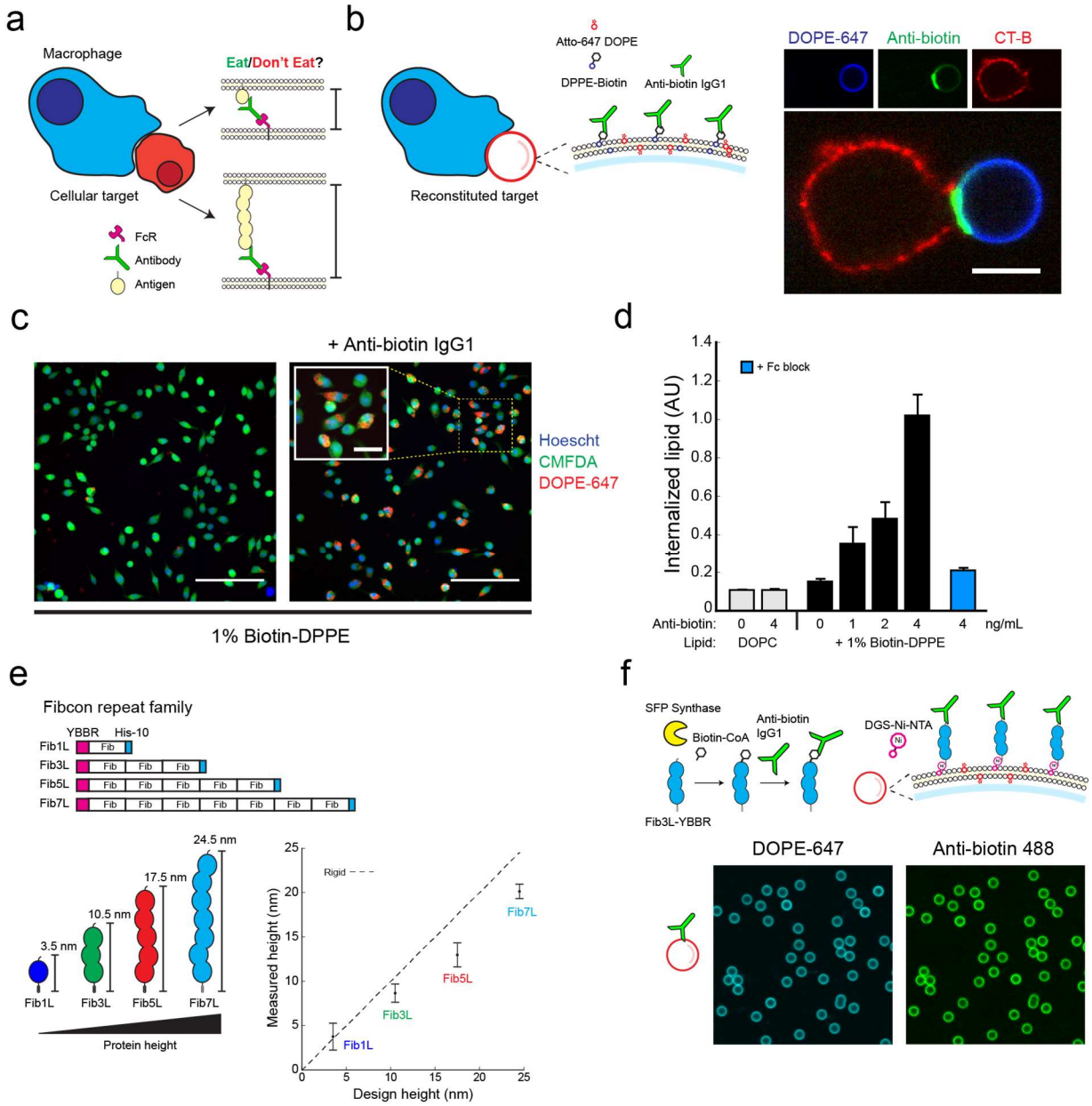

Figure 1: a. The Fc-receptor of a macrophage binds to an antibody bound to unknown antigen with variable size and shape. **b.** Reconstitution of a target cell surface. A supported lipid bilayer containing biotin-DPPE is formed on a 3.5 um glass bead. Anti-biotin antibody binds to the biotin headgroup to fluidly attached to the target surface. Anti-biotin IgG enriches at the contact between an opsonized target and a macrophage. Scale bar 5 um. **c.** A typical field of view (left) after incubating cells with targets containing only POPC lipid and (right) after incubating with biotin-DPPE containing targets. CMFDA (CellMask Green) is used to determine cell area, and DOPE-647 lipid is integrated within cells to quantify phagocytic efficiency. Scale bar of full frame is 100 um, scale bar of inset 10 um. **d.** Quantification of phagocytic efficiency. Targets containing DOPC only are not internalized. Biotin-DPPE targets are internalized in an anti-biotin IgG1 dependent manner. Addition of Fc block (anti-CD32 + anti-CD64) disrupts phagocytosis of biotin-DPPE targets. **e.** Design of Fibcon repeat proteins to

model antigens of increasing height. Fibcon repeat protein estimated heights are F1L = 3.5 nm, F3L = 10.5 nm, F5L = 17.5 nm, and F7L = 24.5 nm. (bottom right) Measurement of Fibcon repeat protein height on supported lipid bilayers using single-axis localization microscopy reveals a slightly sub-rigid configuration. **f.** SFP labeling of N-terminal YBBR peptide on Fibcon proteins generates height-controlled antigens. Addition of anti-biotin IgG1 generates an opsonized target surface with an antibody displayed at variable height.

To quantify phagocytosis, we use confocal microscopy to image the internalization of lipid-beads at single-cell resolution, and an automated image-segmentation routine to quantify the per-cell fluorescence of internalized lipid (Figure 1c). We show that as expected, the efficiency of phagocytosis of biotin-lipid opsonized targets increases with increasing concentrations of anti-biotin IgG1. We further confirmed that incubating macrophages with anti-CD16 and anti-CD32 (FcγRIII and FcγRIIB) antibody (Fc block) completely blocks phagocytosis, demonstrating that internalization of the opsonized SLB-coated beads is FcγR specific (Figure 1d).

Size-variant antigens based on a synthetic FNIII domain

To model cell-surface proteins of different heights in our reconstituted system, we developed a family of size-variant proteins based on repeats of a synthetic FNIII domain (Fibcon), which has a size of 3.5 nm (Figure 1e)[20]. Each protein consists of repeats of the Fibcon domain with no inter-domain linker. We name the repeat proteins Fib1L, Fib3L, Fib5L, and Fib7L. The proteins were expressed and purified in E coli. An N-terminal His-tag enables the proteins to bind fluidly to a target membrane incorporating a nickel-chelating lipid (Figure 1f). In an extended conformation, the proteins have predicted heights of 3.5 nm, 10.5 nm, 17.5 nm, and 24.5 nm (Figure 1e). We used a single-axis fluorescence localization method to measure the distance between the protein N-terminus and an SLB when bound via His-tag. Our measurements confirm that the Fibcon repeat proteins bind to the bilayer in an extended conformation (measured heights are 3.7 nm, 8.6 nm, 13.0 nm, 20.1 nm) (Figure 1e). Negative-stain electron microscopy of single Fib5L proteins reveals an ensemble of extended states, consistent with the conformations of a semi-flexible polymer.

To generate protein antigens with a defined epitope, we incorporated an N-terminal YBBR tag for site-specific enzymatic modification; SFP synthase was used to enzymatically couple biotin-CoA to the proteins, resulting in a family of size-variant antigens that bind fluidly to an SLB surface and can be targeted by anti-biotin IgG1 (Figure 1f).

Phagocytosis of an opsonized target is antigen-height dependent

To determine the impact of antigen height on phagocytosis, we quantified phagocytic efficiency against reconstituted targets bound with Fib1L, Fib3L, Fib5L, and Fib7L protein antigen opsonized with anti-biotin IgG1. Strikingly, we observed decreasing phagocytic efficiency with increasing antigen height; macrophages efficiently internalized beads coated with Fib1L antigen, while phagocytosis was significantly impaired against Fib3L antigen, and nearly absent for Fib5L and Fib7L antigen coated beads (Figure 2b). Using flow-cytometry of the targets we confirmed that equal concentrations of antibody were indeed binding to each protein antigen, suggesting that the change in antibody binding site, and not antibody concentration, was responsible for the observed decrease in phagocytosis.

Since phagocytosis is modulated by antibody concentration[21], we assayed phagocytic efficiency across a range of anti-biotin IgG1 concentrations for each antigen. While all Fibcon targets show increased phagocytosis with increasing concentrations of IgG, the data reveals a size-dependent impairment in the ability to activate the phagocytic response, with dramatically reduced sensitivity as a function of antibody concentration for Fib5L and Fib7L (Figure 2c). Our data suggest that short antigens promote efficient phagocytosis, while antigens that are > 10 nm have severely diminished phagocytic capacity.

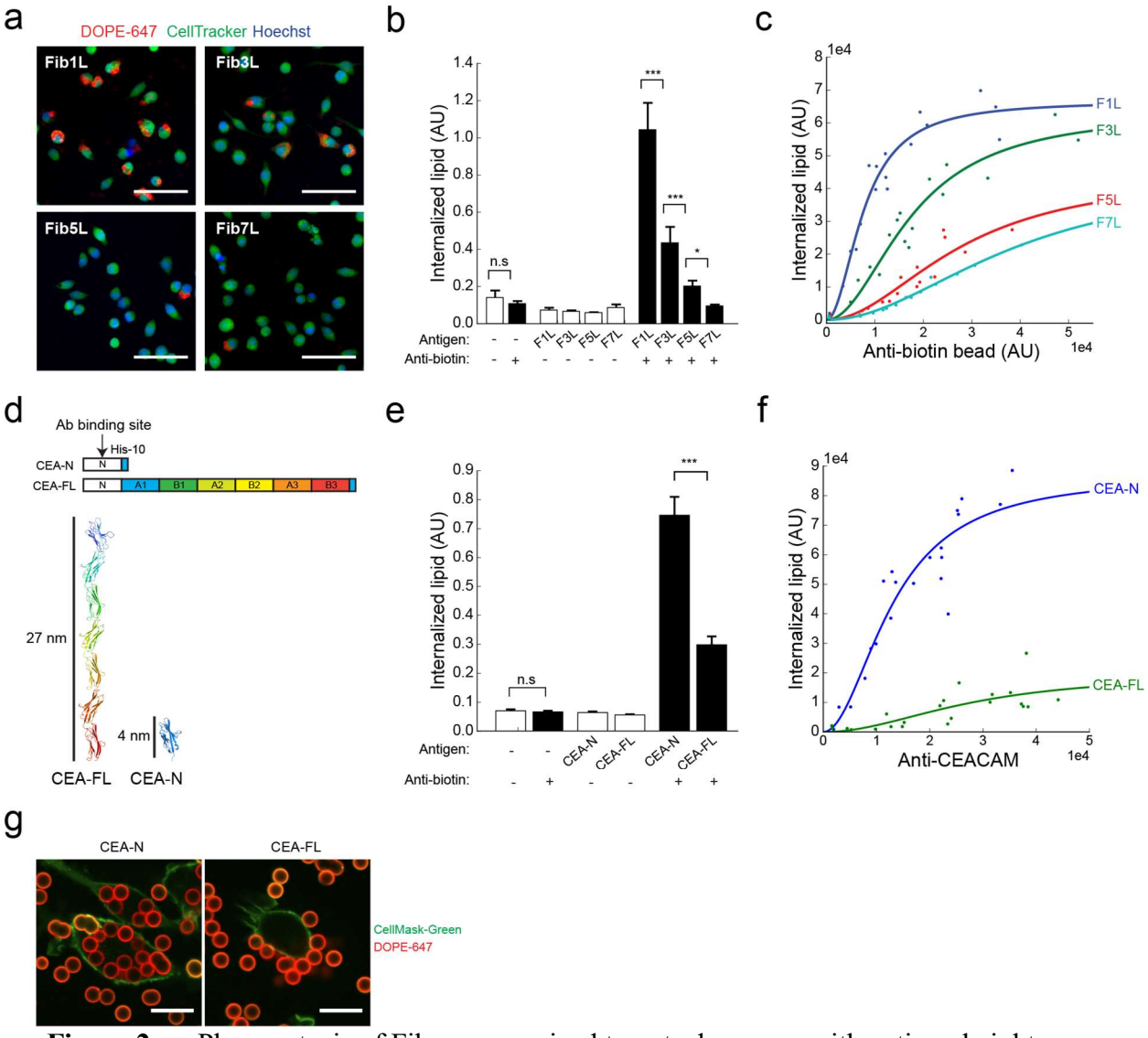

Figure 2: a. Phagocytosis of Fibcon opsonized targets decreases with antigen height. Representative images of phagocytosis after washing shows a decrease in internalized lipid for taller Fibcon species. Scale bars 100 um. **b.** Quantification of phagocytosis of Fibcon opsonized targets. With no anti-biotin IgG added, there is no phagocytosis of targets. Addition of biotinylated Fib1L and anti-biotin IgG leads to maximal phagocytosis. The efficiency of phagocytosis decreases sharply for Fib3L targets, and further for Fib5L and Fib7L targets. **c.** Quantification of phagocytosis vs anti-biotin IgG1

concentration via flow cytometry. Fib1L targets show the most sensitivity to anti-biotin density. Fib3L targets show reduced sensitivity, but an increase in phagocytosis with antibody concentration. The concentration response of Fib5L and Fib7L targets is decreased. **d.** Design of full-length CEACAM (CEA-FL) and truncated CEACAM (CEA-N) proteins. The shared N-terminal is targeted with a single anti-CEACAM antibody, resulting in a protein antigen with an antibody bound 4 nm (CEA-N) or 27 nm (CEA-FL) from the surface of a target. full-length. **e.** Phagocytosis of CEACAM antigens is height-dependent. There is no phagocytosis in the absence of both CEACAM antigen and anti-CEACAM IgG. CEA-N targets are phagocytosed at a level that is significantly different than CEA-FL targets ($p < .05$). **g.** 60x confocal images of (left) CEA-N opsonized targets and (right) CEA-FL opsonized targets after 10 minutes of phagocytosis, without washing. Beads are efficiently internalized when the antibody is attached through CEA-N, but are instead stuck to the outside of the cell but not internalized for CEA-FL targets. Scale bar 15 um.

CEACAM phagocytosis is antigen-height dependent

Is size-dependence a general property of antibody-dependent phagocytosis, or is it limited to our synthetic proteins? We next asked whether the decrease in phagocytosis for tall antigens would hold for the CEACAM family of cell-surface proteins. To this end, we expressed and purified full-length CEACAM5 (CEA-FL, 22.5 nm), along with a truncated version of CEACAM5 consisting of only the N-terminal domain (CEA-N, 3.5 nm) (Figure 2d). We selected a pan-CEACAM antibody that binds directly to the N-terminal domain of CEACAM5, so that beads coated with CEA-FL or CEA-N can be opsonized with an identical antibody. Consistent with our Fibcon experiments, we found that CEA-N is efficiently internalized, while phagocytosis of CEA-FL is significantly reduced (Figure 2e-f). Using flow-cytometry of the targets we again confirmed that equal concentrations of antibody were bound to CEA-FL and CEA-N coated beads.

We assayed phagocytic efficiency across a range of concentrations of anti-CEACAM. The results show that while phagocytosis increases with increasing antibody for both antigens, the increase is dramatically larger for CEA-N (Figure 2g). We concluded that similar to our Fibcon antigens, phagocytosis of CEACAM-family proteins is size-dependent.

Antigen size alters receptor phosphorylation

The first signaling event upon FcγR cross-linking is the phosphorylation of the ITAM by Src family kinases, followed by the recruitment of Syk kinase via its tandem SH2 domains[22]. To test whether the size-dependent modulation of phagocytosis we observed is linked to changes in signaling, we imaged the distribution of phospho-tyrosine on cells fixed during phagocytosis of Fib1L target beads. Images of beads attached to nascent phagocytic cups revealed enrichment of tyrosine phosphorylation at these contact sites. We repeated the experiment for a tall antigen, Fib7L. In contrast to the short antigen, the increase in phospho-tyrosine was notably absent at target contact sites.

Live-cell protein sensor of ITAM phosphorylation

To image the dynamics of ITAM phosphorylation, we developed a live-cell protein sensor for phosphorylation of the FcγR ITAM (Figure 3a). We designed a C-terminal fusion of mCherry

with the tandem SH2 domains of Syk kinase, which are known to mediate binding of Syk to the phosphorylated ITAM[23]. The sensor is transduced into RAW 264.7 macrophages using lentivirus, and is expressed under control of a constitutive weak promoter UBC to prevent interference with endogenous Syk localization and to reduce signal background[24]. Upon contact between cells and an SLB surface coated with Fib1L and opsonized with anti-biotin, the sensor is rapidly recruited from the cytoplasm to clusters of antibody-FcγR at the interface (Figure 3b). The sensor dissociates from these clusters within seconds upon addition of the Src kinase inhibitor PP2, consistent with sensor-specificity for phosphorylated ITAM.

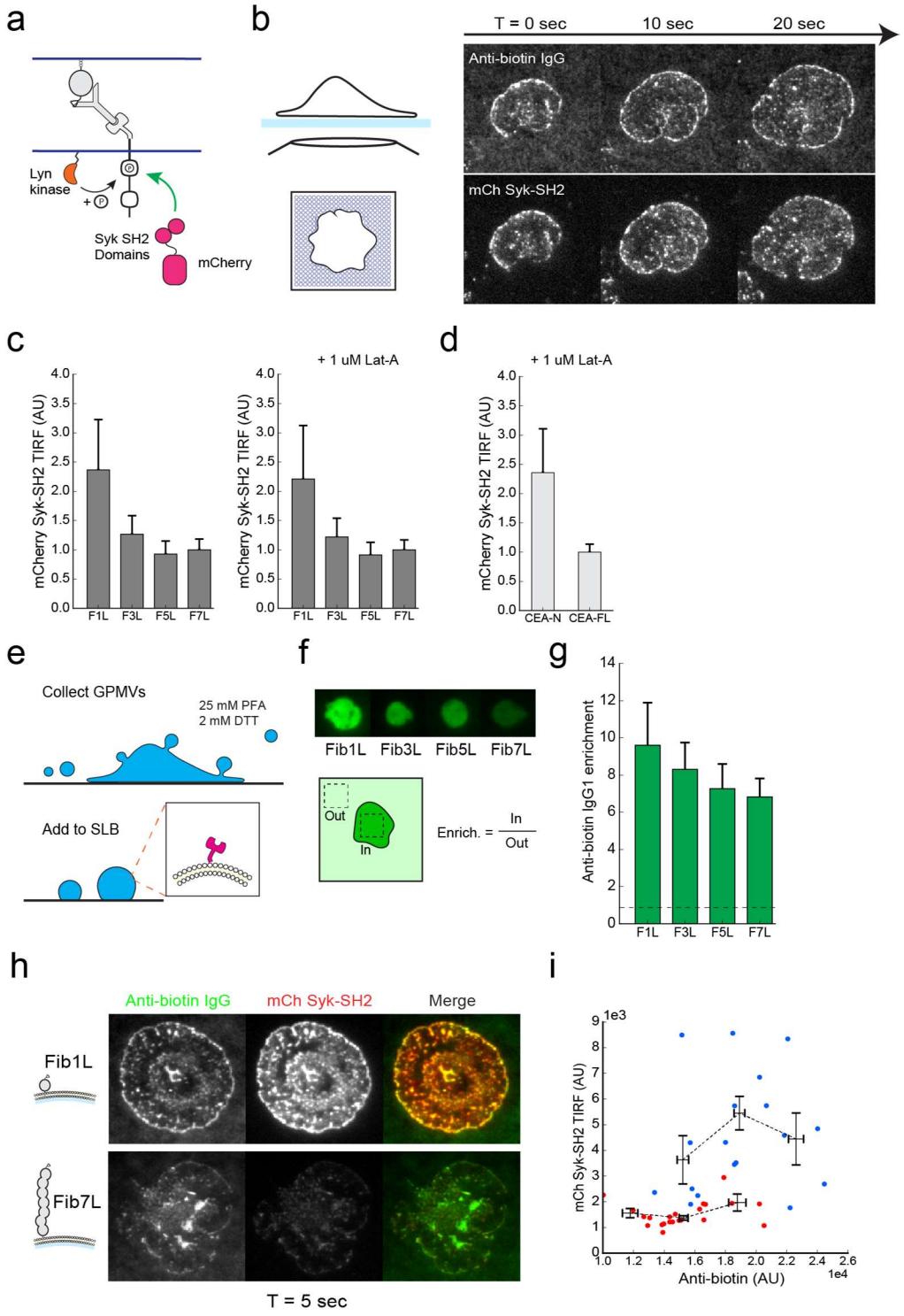

Figure 3: a. A live-cell sensor of ITAM phosphorylation. An N-terminal mCherry attached to the tandem-SH2 domains of Syk kinase is recruited to phosphorylated ITAMs, creating a phosphorylation sensor. **b.** TIRF imaging of cells spreading on a planar lipid bilayer reveal recruitment of the mCh-Syk Sh2 sensor to clusters of bound antibody-FcR. **c.** Quantification of sensor-recruitment to spread cells as a function of antigen height. Fib1L shows significantly increased recruitment of the mCh-Syk-SH2

sensor. Some residual recruitment is visible for the Fib3L antigen, while Fib5L and Fib7L antigens lead to background levels of sensor visible in TIRF images. **d.** Cells treated with Lat-A show recruitment of mCh-Syk Sh2 sensor to cell-bilayer interfaces. The antigen-size dependence of sensor recruitment is the same for Lat-A treated cells. **d.** mCh-Syk Sh2 sensor recruitment is size-dependent for CEACAM antigens, with increased recruitment to CEA-N vs CEA-FL coated planar bilayers. **e.** Giant plasma-membrane derived vesicles (GPMVs) are formed from blebbing cells, and the resulting membranes contain membrane-bound receptors including FcR. **f.** GPMVs form footprints upon contact with opsonized bilayer surfaces. The enrichment ratio of anti-biotin is measured as the intensity ratio between region beneath the cell (footprint) and the remaining background bilayer. **g.** Enrichment-ratio of anti-biotin bound to Fibcon antigens of increasing height (F1L = 9.60, F3L = 8.31, F5L = 7.26, F7L = 6.82) reveals a decrease in FcR-antibody affinity with increasing antigen height. However, significant enrichment is still observed for Fib7L, demonstrating that there is no major defect in antibody-FcR binding for tall antigens. **h.** 60x TIRF images of cells during spreading on Fib1L (top) and Fib7L (bottom) opsonized surfaces. The anti-biotin channel shows enrichment of the FcR-antibody complex for both Fib1L and Fib7L. For Fib1L coated surfaces, the mCh Syk-SH2 sensor is recruited to clusters of anti-biotin. However, Fib7L coated surfaces recruit significantly less sensor to antibody-FcR clusters. **i.** Single-cell plot of anti-biotin intensity vs mCh-Syk Sh2 sensor intensity. Despite variation in the mean anti-biotin concentration at the footprint across all cells between Fib1L and Fib7L, sensor recruitment to Fib1L is significantly higher across the entire anti-biotin concentration range.

Phosphorylation of the ITAM decreases with increasing antigen height

We next asked whether phosphorylation of FcγR changes systematically with antigen height. To do this, we used TIRF microscopy to quantify membrane-localized sensor at the macrophage-contact interface 15 minutes after spreading on an opsonized planar SLB coated with Fib1L-Fib7L antigen. We found that the level of sensor-recruitment decreases significantly between Fib1L and Fib3L antigen, with recruitment dropping to near background levels for Fib5L and Fib7L.

We previously noted that clusters of antibody-FcγR were trafficked inward from the periphery of the cell, consistent with interactions between FcγR and the actin cytoskeleton that have been described[16,25]. Interestingly, the decrease in sensor recruitment for tall antigens was still evident in Latrunculin A treated cells, suggesting that interactions between FcγR and actin filaments are not strictly necessary for receptor phosphorylation (Figure 3c). We similarly observed a decrease in receptor-recruitment in macrophages interacting with tall CEA-FL relative to short CEA-N antigen (Figure 3d).

TIRF images of macrophages during initial engagement and spreading on a planar surface coated with opsonized Fib1L or Fib7L antigen show a striking decrease in localization between antibody-FcγR clusters and the Syk-SH2 sensor (Figure 3h). Images were thresholded to segment clusters of enriched IgG, and the average fluorescence intensity of the sensor within these clusters was quantified for each cell, revealing a decrease in receptor phosphorylation for Fib7L antigen relative to Fib1L antigen during the early stages of engagement.

Size-dependent decrease in antibody-FcγR affinity

Since our experiments show that the concentration of antibody can modulates phagocytic efficiency, we asked whether there was a difference in effective concentration of FcγR within clusters for antigens of different heights. To test if the concentration of antibody-FcγR complex differed between Fib1L and Fib7L antigens, we measured the average intensity of anti-biotin within these clusters. We found that for a Fib7L antigen, the average concentration of clustered anti-biotin was lower compared to the Fib1L antigen. This result could be explained by a size-dependent decrease in receptor-ligand affinity due to changes in binding entropy that has been predicted physically.

To quantify the change in affinity with increasing antigen height, we turned to giant plasma membrane vesicles (GPMVs), which are formed from detached cellular-membrane blebs and have a lipid and protein composition that is similar to the plasma membrane (Figure 3e). We isolated GPMVs from RAW 264.7 macrophages and added them to a supported-bilayer surface coated with antigen. GPMVs settled onto the bilayer and formed planar footprints, with anti-biotin IgG bound to FcγR clearly enriched at the interface. We quantified the 'enrichment index' of the anti-biotin IgG by taking the intensity ratio between regions beneath GPMVs and regions within the lipid-bilayer background; since bound complexes become trapped at the interface, the 'enrichment index' provides a metric of receptor-ligand affinity (Figure 3f). Although for each antigen we observed significant enrichment of anti-biotin at the interface, consistent with FcγR binding, the data revealed a consistent decrease in receptor-ligand affinity with increasing antigen height (Fib1L = 9.6, Fib3L = 8.3, Fib5L = 7.2, Fib7L = 6.8) (Figure 3g).

We next asked whether the decrease in receptor phosphorylation could be explained only by decreasing receptor-ligand affinity. Plotting anti-biotin intensity against Syk-SH2 sensor recruitment on a single-cell basis, we found that the sensor recruitment to Fib1L was significantly higher across the entire anti-biotin concentration range, suggesting that changes in receptor concentration cannot explain decreased phosphorylation for tall antigens (Figure 3i). Further, we renormalized the concentration axis of the previously described phagocytic efficiency data by the enrichment index for each antigen. The renormalization caused the Fib5L and Fib7L trends to collapse onto a similar curve, suggesting that the difference in phagocytic efficiency between these antigens can be explained by affinity. However, the phagocytic response of the Fib1L and Fib3L remain significantly different, with the strongest response observed for the shortest Fib1L antigen.

Segregation of the phosphatase CD45 from clustered antibody-FcγR is antigen-size dependent

Phosphorylation of the FcγR ITAM is opposed by receptor-tyrosine kinases CD45 and CD148 (Figure 4a)[8]. To ask how inhibitory phosphatases are spatially organized on the membrane relative to enriched antibody-FcγR, we use direct-labeled antibodies to image the distribution of CD45 at the interface between a macrophage and an SLB. TIRF images revealed the striking segregation between anti-biotin and CD45 when macrophages engaged with a Fib1L opsonized surface (Figure 4b). In contrast, we observed no segregation of CD45 from anti-biotin clusters on a Fib7L opsonized surface (Figure 4b).

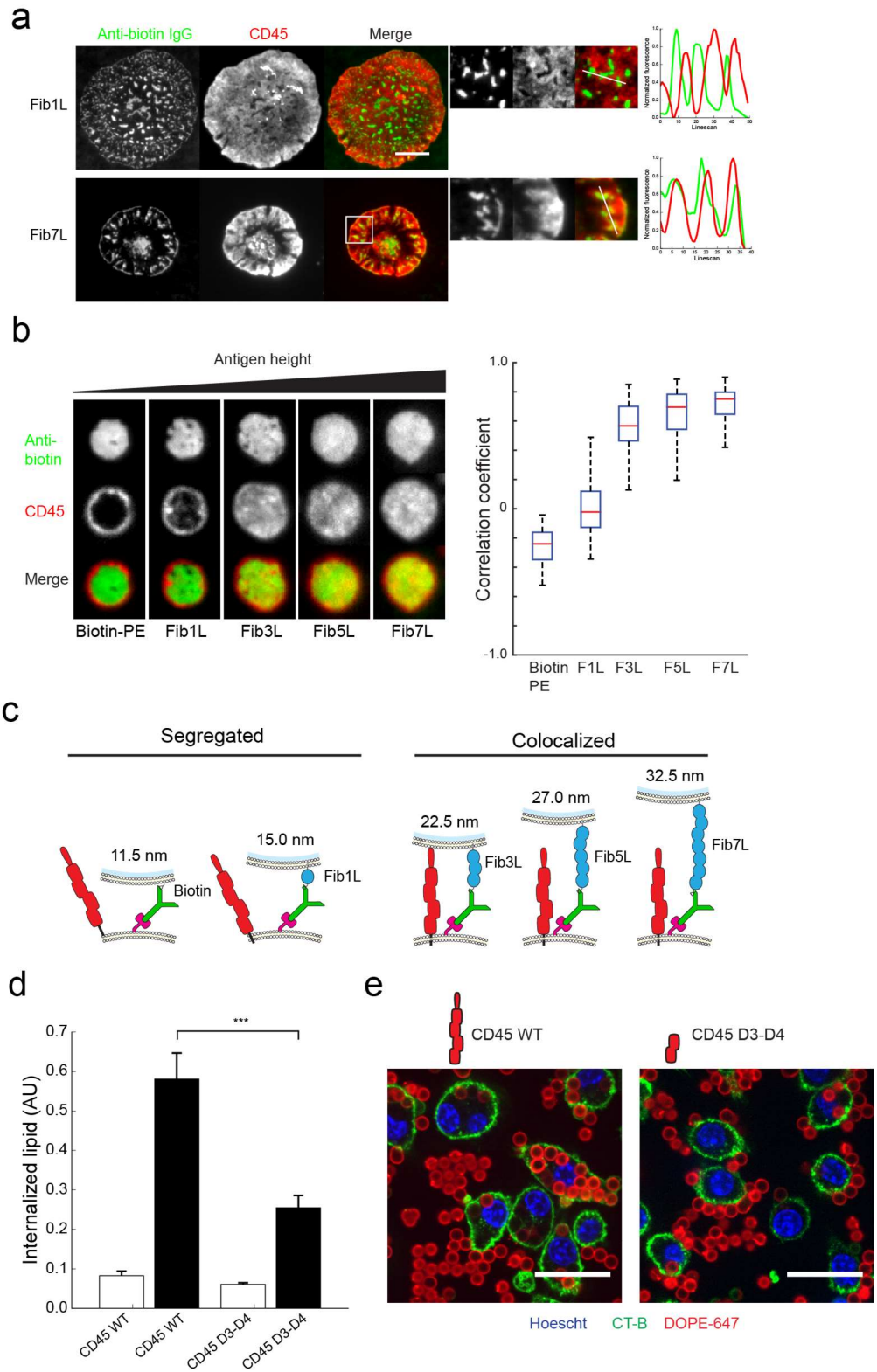

Figure 4: a. TIRF images of cell engaged with Fib1L (top) and Fib7L (bottom). Clusters of enriched anti-biotin are visible on both target surfaces. For a Fib1L antigen, CD45 is excluded from regions of anti-biotin enrichment. For a Fib7L antigen, segregation of CD45 is not observed, as is evident from the linescan across a region of surface-engaged

membrane. **b.** GPMVs in contact with antigen opsonized bilayers. For biotin-PE and Fib1L antigens, CD45 labeled with antibody is excluded from the contact interface. The exclusion of CD45 decreases for Fib3L and taller antigens. Correlation analysis (right) reveals a sharp decrease in segregation for antigens Fib3L and taller, with little change in segregation for antigens taller than Fib3L. **c.** Estimated size of the membrane-membrane interface when enforced by antibody-FcR binding through antigens of different heights. When compared to the height of CD45RO (22.5 nm), segregation is expected for the Biotin and Fib1L, but not Fib3L and taller antigens. **d.** CRISPR/Cas9 truncation of CD45wt into a protein with an ectodomain containing 2 Ig domains. Truncated CD45 reduces the level of phagocytosis significantly vs wild type cells. **e.** 60x confocal images of beads incubated with CD45wt and CD45 D3-D4 cells shows efficient internalization for wild type cells, and beads bound to but not internalized by CD45 D3-D4 cells.

We hypothesized that CD45 was physically excluded from close membrane-membrane contacts formed by antibody-FcγR due to its large extracellular domain. To determine the role of the membrane-gap, which is determined by the dimensions of the antigen-antibody complex, we generated interfaces between GPMVs and planar SLBs for antigens of increasing height. TIRF images of the interface show that CD45 is almost completely excluded from the membrane interface for both a biotin-lipid and Fib1L antigen (Figure 4c). However, interfaces formed with Fib3L antigens were populated by freely diffusing CD45. Similarly high levels of CD45 were observed at the interface for Fib5L and Fib7L antigens. Co-localization analysis reveals a size-dependent segregation threshold, with antigens Fib3L (10.5 nm) and taller failing to exclude CD45 (Figure 4c).

We computed the size of the antigen-IgG-FcγR complex for each antigen by adding the estimated height of the antigen to the distance between the base of FcγR and the antigen-binding site of an IgG antibody (PDB*, 11.5 nm)[4], and compared this height to the size of CD45RO (PDB*, 22.5 nm)[26] (Figure 4d). We have previously shown that proteins > 5 nm taller than a membrane-interface are excluded from the interface due to steric interaction with the membranes[15]. The interfaces formed through both biotin-lipid (5 nm) and Fib1L (15 nm) are both significantly shorter than CD45RO, and are thus predicted exclude CD45. However, the estimated height of the interface formed by Fib3L (22 nm) is extremely close to the height of CD45RO, and is therefore not expected to exclude CD45. The estimated height of the Fib5L interface (27.0 nm) and the Fib7L interface (32.5 nm) are both taller than CD45RO, and similarly are not predicted to exclude CD45. These calculations are completely aligned with the co-localization analysis of the GPMV data, and support a size-dependent mechanism of CD45 segregation that is governed by the height of the membrane-interface.

Truncation of the CD45 ectodomain using CRISPR/Cas9 disrupts phagocytosis

If segregation of CD45 is necessary for FcγR phosphorylation and phagocytosis, then we predicted that interfering with the mechanism of segregation by decreasing the size of the CD45 ectodomain would decrease phagocytic efficiency against short antigens. We developed a strategy for truncating the ectodomain of endogenous CD45 using CRISPR/Cas9. Using two independent guide RNAs, we targeted the intronic region downstream of the first coding exon (containing the start codon and the signal peptide), and a separate intronic region directly upstream of an exon coding for the D3 FNIII domain. Excision of a large genomic region

followed by repair via non-homologous end joining results in a gene coding for CD45 protein with a truncated ectodomain, containing only the two final FNIII domains D3-D4. The ectodomain of this protein (CD45 D3-D4) is predicted to be 7.0 nm tall (analysis from the structure of full-length CD45, PDB 5FMV), which is short enough to disrupt segregation of CD45 at a contact-interface formed through Fib1L.

We compared the phagocytic efficiency of a population of CD45 D3-D4 cells to CD45RO cells. Our data shows that truncation of the CD45 ectodomain significantly reduced phagocytic capacity (Figure 4d). We collected images cells during the process of phagocytosis; the images revealed that multiple beads bound to the cell periphery of CD45 D3-D4 cells, with dramatically reduced internalization relative to CD45RO cells (Figure 4e).

Discussion

As antibody therapeutics move into the clinic, it has become increasingly important to understand their mechanism of action. While it is well known that physical properties of the antibody Fc domain, such as isotype and glycosylation, can produce divergent immune responses due to changes in binding specificity for activating and inhibitory Fc-receptors[27,28], less is known about how the structure the antigen, which anchors the antibody in a unique position and orientation relative to the cell-surface, might impact the activity of immune effector cells.

In this work we demonstrate that FcγR-dependent phagocytosis is modulated by the height of antibody display above a target cell-surface. Specifically, we find that antigens that position an antibody < 10 nm from cell-surface are optimal for stimulating phagocytosis. The critical requirement for FcγR signaling is close contact between a macrophage and target surface. As the macrophage engages with a target surface, close contact physically forces the reorganization of proteins on the macrophage cell surface: tall proteins are pushed out by the small membrane-membrane gap. We demonstrate that the tyrosine-phosphatase CD45 is excluded from sites of FcγR-antibody binding in a size-dependent manner, and that a failure to segregate CD45 from a contact site formed by an antigen > 10 nm tall leads to a decrease in FcγR phosphorylation. We show that modifying the size of the endogenous CD45 ectodomain disrupts phagocytosis against short antigens, proving that segregation of inhibitory phosphatases is required for phagocytosis.

It has been suggested that Fc-dependent ADCC is more efficient for antibodies bound close to the membrane. This has been attributed to improved engagement with complement components, but the results here suggest an additional mechanism that favors short antigens. There is circumstantial evidence that the antigens targeted by clinically successful therapeutic antibodies are all relatively small cell-surface receptors (CD20, EGFR, HER2, CTLA4, PDL1), and it will be interesting to see if this bears out as more antibodies with diverse targets enter clinical trials.

In a recent study, it was found that the efficiency of ADCC *in vitro* was decreased for an antigen-epitope that was 16 nm above the surface, and that delivery of an antibody against a short antigen elicited successful tumor clearance *in vivo*, but a tall antigen targeted by the same antibody was ineffective. This data supports our observations of phagocytosis *in vitro,* and *we* believe our study may provide a mechanism to explain these results. Further testing of different effector

function *in vivo*, including ADCP, and their impact on tumor clearance, will show whether this is a general principle.

Our reconstituted system is useful for understanding the mechanism of phagocytosic triggering through FcγR because the targets contain only a single stimulus, the bound antibody. However, phagocytosis against cellular targets involves interactions between multiple receptors and varied ligands. Further, the cell surface is packed with proteins of different sizes, and these may influence the ability of an FcγR to bind (in contrast to our system, where binding is easy). It will be interesting to see if short antigens always win out *in vivo*, where interactions with integrins, scavenger and lipid receptors, and other pattern-recognition receptors are all generating competing impacts on target binding. A further question is how to resolve the competition between activating and inhibitory signals, which can be generated by receptors and ligands of different heights. While in our system interaction between FcγR and an antibody is sufficient for segregating inhibitory phosphatases and triggering phagocytosis, we can't rule out additional influences on the localization of these proteins, such as the integrin diffusion barrier that was described recently. Further, while we show that interaction with the cytoskeleton are not necessary for phosphorylation of the receptor, it is certain that actin is required for phagocytosis, and any connections between receptors and actin will certainly influence the spatial organization of cell-surface components. We suggest that size-dependent signaling is one organizing principle that is always influencing organization, superposed on additional lateral organization such as cytoskeletal interactions and lipid microdomains. The sensitivity of kinase-phosphatase balance in this system makes it likely that in a system with full-complexity multiple mechanisms can influence outcome.

We are also intrigued by the topology of inhibitory signaling, which shares many proteins with FcγR. For inhibitory receptors where the physical dimensions of a ligand are not defined, it will be interesting to find out if binding location matters. Other receptors have a defined ligand that places it within the proper distance to generate segregation – this has been noted for KIR receptors on NK cells. Recent efforts to generate chimeric antigen receptors and bi-specific targeting antibodies for activating receptors that have a defined ligand will be critically dependent on this mechanism for selecting appropriate antigen targets that satisfy the physical requirements of signaling. Finally, this study opens up possibilities for optimizing therapeutic monoclonal antibodies in cancer and infectious disease, and to start enumerating design principles based on physical mechanism for successful immunotherapy.

Materials and methods

Chemical reagents.

Hepes (4-(2-hydroxyethyl)-1-piperazineethanesulfonic acid), MOPS (3-(*N*-morpholino)propanesulfonic acid), TCEP (*tris*(2-carboxyethyl)phosphine), KCl, NaCl, glucose, sucrose, and imidazole were purchased from Fisher Scientific. Imidazole was purchased from Sigma Aldrich. Atto 647-DOPE was purchased from ATTO-TEC. DOGS-Ni-NTA (1,2-dioleoyl-*sn*-glycero-3-[(*N*-(5-amino-1-carboxypentyl)iminodiacetic acid)succinyl], with nickel salt) and DOPC (1,2-dioleoyl-*sn*-glycero-3-phosphocholine) were purchased from Avanti Polar Lipids (Alabaster). All purchased chemical reagents were used without further purification.

SUV preparation.
SUVs were prepared by rehydrating a lipid film composed primarily of 16:0 18:1 POPC (Avanti), doped with up to 2% of Biotin-DPPE or DGS-NI-NTA and 0.8% Atto-647 DOPE (Attotec) in pure deionized H20. Rehydrated solution was vortexed briefly, sonicated at low-power (20% of max) using a tip-sonicator, and finally filtered through a 200 nm PVDF filter (Millipore). Solutions of SUVs were stored on ice and used within 48 hours to avoid phospholipid oxidization.

Preparation of supported-lipid bilayer coated glass beads.
40 uL of 3.78 um glass bead (Bangs labs) slurry (10% solids) were cleaned using a 3:2 mixture of H2SO4:H2O2 (Piranha), and clean beads were spun down at 1000 G and resuspended in 400 uL of H20. Clean beads were stored in H20 at room temperature and used within 48 hours. To assemble supported-lipid bilayers, 20 uL of SUV solution was diluted in 80 uL of MOPS buffer (25 mM MOPS, 125 mM NaCL, pH 7.4), and 10 uL of clean bead slurry were added and mixed gently by pipetting. The bead/SUV mixture was incubated for 15 minutes at room temperature while rotating continuously to reduce bead sedimentation. Beads were spun down gently at 50 G for 1 minute, and SUV solution was carefully removed and replaced with PBS. The fluidity of the lipid-bilayer was assessed by imaging beads deposited on a glass coverslip with a spinning-disk confocal microscope (Nikon) at 60x magnification and high laser power, where diffusion of single-molecules of labeled lipid was visible after photo-bleaching a small region-of-interest.

Reconstitution of an antigen-antibody opsonized lipid surface.
SUV mixtures with up to 2% DGS-Ni-NTA were used to prepare lipid-bilayer coated beads. To prepare protein-coated beads, beads were incubated with 50 nM recombinant protein containing a C-terminal 10-His tag for 15 minutes. The protein binds fluidly to the surface via the Nickel-His interaction, and the interaction of one-protein with up to ten DGS-Ni-NTA lipids lead to nearly irreversible attachment (reference). To prepare a protein-coated and antibody opsonized beads, an anti-biotin IgG1 was added at 1-5 ng/mL and incubated along with the protein, such that the anti-biotin antibody bound fluidly to the surface via interaction with the His-tagged protein.

Microscopy assay of phagocytosis.
96-well flat-bottom tissue-culture plates (Corning) were seeded with 35,000 cells in 200 uL of RPMI 1640 medium. Cells were incubated at 37 C for at least 2 hours to allow attachment to the plastic surface. To start the assay, 100 uL of bead-protein-antibody solution containing ~500,000 beads was added to each well, and the plate was returned to 37 C for exactly 20 minutes. After 20 minutes, wells were washed once with PBS to remove non-internalized and partially bound beads, and then overlaid with a solution containing 1 uM CMDFA and 10 uM Hoechst 33342 (ThermoFisher) to fluorescently stain the cell-cytoplasm and cell-nuclei. Individual wells were imaged after 10 minutes with the staining solution on a spinning-disk confocal microscope (Nikon) at 20x. For each well, a grid pattern of 4 fields-of-view was recorded. Images were segmented using a routine written with CellProfiler (Broad Institute) to isolate single-cells, and the fluorescence intensity in the Atto-647 channel was integrated on a single-cell basis to generate the quantification of internalized lipid.

Flow-cytometry assay of phagocytosis.

96-well plates were prepared for phagocytosis as described above. To start the assay, 100 uL of bead-protein-antibody solution was added to each well, and the plate was returned to 37 C for 20 minutes. After 20 minutes, wells were washed once with PBS to remove non-internalized and partially bound beads, and then overlaid with a solution containing 20 mM EDTA and 10 uM Hoechst 33342 to detach cells from the tissue-culture plastic. Cells were gently de-adhered by pipetting up and down, then left suspended within the 96-well plate for flow-cytometry. Flow cytometry was performed on the Attune NxT equipped with an autosampler and analyzed with the provided software (Thermo Fisher). Single-cells were gated using the Hoechst channel in addition to forward and side-scatter. The 647-channel recording the fluorescence of Atto-647 lipid was used to quantify internalized lipid per cell (supplementary figure*).

Size-variant Fibcon protein antigens.

Fibcon repeat family design. The FNIII domain occurs with high frequency in cell-surface proteins, where it is often linked together in an N-C topology to create proteins with extended height (references). We designed a family of synthetic proteins that similarly rely on the FNIII domain to generate height. The Fibcon domain is a high-stability FNIII domain designed through multiple-sequence alignment (reference). The DNA sequence coding for the Fibcon protein was synthesized as a gblock gene fragment. Repeats of the Fibcon sequence were cloned into a pET28b vector (EMD Millipore) for expression in E. coli cells with no linker region via Gibson assembly. The Fibcon repeat sequence was flanked by an N-terminal YBBR peptide (reference) and a C-terminal His-10 followed by a KCK sequence for chemical labeling, and terminated with an additional His-6 sequence.

Protein expression and purification. All proteins were expressed in Rosetta DE3 competent cells (EMD Millipore). Cells were grown at 37 °C, induced with 0.3 mM IPTG and grown overnight at 18 °C. Cells were harvested and resuspended in 25 mM Hepes, 150 mM NaCl, 0.5 mM TCEP and 10 mM imidazole, and lysed by freeze thawing and sonication. The lysate was centrifuged for 45 min at 20,000*g*, affinity purified over a His-Trap HP column (GE Healthcare) through imidazole gradient elution on an AKTA Pure (GE Healthcare) system. Peak fractions were concentrated and gel-filtered via a Superdex 200 column into 25 mM Hepes, 150 mM NaCl, 0.5 mM TCEP. Proteins were concentrated, and purity was assayed on an SDS page gel. For Fibcon family proteins, the increase in protein molecular weight was verified by an elution shift during gel-chromatography from a Superdex 200 column (supplementary figure).

Site-specific modification with SFP synthase. Fibcon proteins were biotinylated at the N-terminus using an SFP synthase catalyzed reaction, which conjugates biotin to the YBBR tag (reference). 100 μM recombinant Fibcon protein, 120 μM Biotin CoA, 10 μM SFP synthase and 40 mM MgCl were mixed in a 100 μL reaction volume and rotated for 3 hours at room temperature. The labeled protein product was purified on a Superdex 75 10/300 gel filtration column (GE Healthcare) into 25 mM Hepes, 150 mM NaCl, 0.5 mM TCEP. Biotinylation of the product was confirmed by attaching the protein to a supported lipid bilayer and imaging the binding of a fluorescently labeled anti-biotin antibody (Alexa Fluor 488 BK-1/39, eBioscience).

Protein purification of CEA-N and CEA-FL protein antigens.

HEK293T cells were grown to 70% confluency in a T175 flask and transfected with CEA-N or CEA-FL DNA in a pCAGGS expression vector using TransIT-293T transfection reagent (Mirus

Bio). After 48 hours, the supernatant was collected and Halt™ protease and phosphatase inhibitor was added (ThermoFisher). The proteins were affinity purified over a His Trap Excel column (GE Healthcare) and eluted with a high imidazole buffer containing 25mM Hepes, 150 mM NaCl and 500 mM imidazole. The proteins were gel-filtered using a Superdex 200 column (GE Healthcare) and the buffer was exchanged to remove imidazole. The proteins were concentrated and the purity was confirmed using SDS-PAGE.

Immunofluorescence of phosphor-tyrosine.
For imaging interfaces between cells and supported lipid bilayer coated beads, cells were seeded into 8-well imaging chambers with a cover-glass bottom (Cellvis) and beads were added to the wells once the cells had fully adhered to the cover-glass. For immunofluorescence of cells on a cover-glass coated supported lipid bilayer, cells were seeded directly onto the bilayer. After a 15 minute incubation at 37° C, the cells were fixed for 10 minutes with 4% paraformaldehyde in PBS. Cells were permeabilized with 0.1% saponin (Alfa Aesar) and blocked with 3% (w/v) BSA in PBS along with 0.5 μg/mL Fc Block™ (BD Biosciences). Saponin (0.1%) was included in all subsequent probing and washing steps. Phospho-Tyrosine antibody (P-Tyr-1000 MultiMab™, Cell Signaling Technology) was added to cells at a dilution of 1:500 and incubated at room temperature for 1 hour. The cells were washed and secondary antibody (Alexa Fluor 488 AffiniPure Donkey Anti-Rabbit IgG, Jackson ImmunoResearch) was added at a dilution of 1:1000 and incubated for 1 hour at room temperature. The cells were given a final wash in PBS before imaging.

Live-cell sensor of ITAM phosphorylation based on Syk kinase tandem-SH2 domains.
Syk-SH2 sensor. The tyrosine-protein kinase Syk is recruited to the phosphorylated ITAM of Fc-receptors via an interaction with its tandem-SH2 domains (reference). A sensor that localizes specifically to phosphorylated ITAM was designed by placing a fluorescent protein C-terminal from the isolated Syk SH2 domains. The sensor construct consists of a C-terminal mCherry fluorescent protein, followed by a linker region, followed by amino acids 2-261 of the tyrosine-protein kinase Syk from Mus musculus (NP_035648), a region which covers the tandem SH2 domains of Syk (supplementary figure). The sensor was cloned into the pHR lentiviral expression vector (Clonetech) under control of the low-expression UBC promotor (reference).

Lentivirus production. HEK293T cells were grown in a 6-well plate to 80% confluency, and 160 ng VSV-G, and 1.3 μg CMV 8.91 were transfected into HEK293T cells using TransIT-293T transfection reagent (Mirus Bio). Viral supernatants were collected 60 hours after transfection and spun at 4000 G to remove HEK cells. Viral supernatant was stored at 4 °C for no longer than 48 hours prior to infection. For lentiviral infection, 500 uL of viral supernatant was added to 5e5 RAW 264.7 macrophages along with 4 ug/mL polybrene, and cells were spun at 400G for 25 minutes at 37 °C and then resuspended and plated in a 6-well plate. Viral media was replaced fresh growth media 24 h after infection. Cells were sorted via fluorescence-activated cell sorting on an Influx Cell Sorter (Beckton-Dickinson), and a population of cells expressing the mCh-Syk-SH2 sensor was expanded and frozen for later use.

TIRF microscopy and quantification of phosphorylation.

Supported lipid bilayer (SLB) preparation. SLBs were formed as previously described by fusion of small unilamellar vesicles on RCA-cleaned glass coverslips. 40 uL of SUV solution was diluted in 60 uL of MOPS buffer (25 mM MOPS, 125 mM NaCL, pH 7.4) in a PDMS chamber sealed over an RCA cleaned coverslip. The SUV mixture was incubated for 15 minutes at room temperature. Next, the SUV solution was washed 5x with 60 uL of PBS without drying the coverslip. The fluidity of the resulting lipid-bilayer was assessed by imaging with a spinning-disk confocal microscope (Nikon) at 60x magnification and high laser power, where diffusion of single-molecules of labeled lipid was visible after photo-bleaching a small region-of-interest.

TIRF-microscopy of macrophage surface-engagement. A solution consisting of 50 nM antigen protein and 5 ng/mL of IgG1 antibody was added to the hydrated SLB and incubated for 15 minutes at 37 °C. All imaging experiments were performed within an incubator stage insert in a 5% CO2 environment at 37 °C (Oko labs). 1e4 RAW 264.7 were added dropwise to the imaging chamber and allowed to settle towards the SLB over 5 minutes. In some experiments, cells were preincubated with CellMask (Invitrogen) to stain the cell membrane. TIRF imaging was performed on a Ti Eclipse microscope (NIKON) using a 60x TIRF 1.49 NA objective and an iXon Ultra EMCCD (Andor).

Image processing. All images were processed with custom code written in Python (Python.org). For quantifying mCh-Syk-SH2 localization to at the plasma membrane, single-cells were segmented using the CellMask channel, and the intensity of the mCh-Syk-SH2 channel was integrated within this region to quantify sensor-recruitment. To quantify mCh-Syk-SH2 localization to individual clusters of antibody-FcR, Otsu thresholding was performed to isolate high-intensity anti-biotin clusters from the background level of anti-biotin bound to the SLB, and the intensity of the mCh-Syk-SH2 channel within these clusters was averaged to quantify sensor-recruitment for each cell.

Live-cell antibody-based imaging of CD45 localization.
Cells were incubated with .5 ug/ml anti-mouse CD45 antibody 30-F11 directly conjugated to Alexa Fluor 647 (Biolegend) for 10 minutes. 50 uL of cells (1e4 cells) were diluted directly into 100 uL imaging chambers containing hydrated, protein and antibody bound SLBs (described above). After allowing cells to settle to the SLB over 5 minutes, two-color TIRF images of anti-CD45 (647) and anti-biotin (488) localization were collected on newly surface-engaged cells over a period of 15 minutes.

Giant plasma-membrane vesicles.
Giant plasma membrane vesicle (GPMV) formation. GPMVs were made following the protocol outlined by Sezgin *et al.* (Nature Protocols 2012). In brief, cells were seeded in a 6-well plate and allowed to adhere. They were then washed with buffer (10 mM Hepes, 150 mM NaCl, 2mM CaCl2) before addition of vesiculation agent (25 mM PFA and 2 mM DTT in the same buffer). GPMVs formed for one hour at 37 °C and were collected by removing the supernatant from the cells.

GPMV antibody-based imaging of CD45 localization. GPMVs were added directly to 100 uL imaging chambers containing hydrated, protein and antibody bound SLBs (described above). After settling for 15 minutes, Alexa Fluor 647 labeled CD45 antibody 30-F11 (Biolegend) was

added to the well to a concentration of 0.5 ug/mL. The GPMVs were imaged after an incubation period of 10 minutes.

Correlation analysis. Regions corresponding to the complete surface-area of single spreading cells were segmented in Python using the anti-CD45 channel, and a Pearson's correlation coefficient was calculated to quantify colocalization between CD45 and anti-biotin IgG. For GPMVs, membrane vesicles were stained with CellMask, and the CellMask channel was segmented to identify regions of vesicle surface contact.

Truncation of the CD45 ectodomain using CRISPR/Cas9

If segregation of CD45 is necessary for FcγR phosphorylation and phagocytosis, then we predicted that interfering with the mechanism of segregation by decreasing the size of the CD45 ectodomain would decrease phagocytic efficiency against short antigens. We developed a strategy for truncating the ectodomain of endogenous CD45 using CRISPR/Cas9 (Figure 5a). Using two independent guide RNAs, we targeted the intronic region downstream of the first coding exon (containing the start codon and the signal peptide), and a separate intronic region directly upstream of an exon coding for the D3 FNIII domain. Excision of a large genomic region followed by repair via non-homologous end joining results in a gene coding for CD45 protein with a truncated ectodomain, containing only the two final FNIII domains D3-D4.

1. DiLillo, D. J., Tan, G. S., Palese, P. & Ravetch, J. V. Broadly neutralizing hemagglutinin stalk-specific antibodies require FcγR interactions for protection against influenza virus in vivo. *Nat. Med.* **20,** 143–151 (2014).
2. Erwig, L. P. & Gow, N. A. R. Interactions of fungal pathogens with phagocytes. *Nat. Rev. Microbiol.* **14,** 163–176 (2016).
3. Weiskopf, K. & Weissman, I. L. Macrophages are critical effectors of antibody therapies for cancer. *mAbs* **7,** 303–310 (2015).
4. Lu, J., Ellsworth, J. L., Hamacher, N., Oak, S. W. & Sun, P. D. Crystal structure of Fcγ receptor I and its implication in high affinity γ-immunoglobulin binding. *J. Biol. Chem.* **286,** 40608–40613 (2011).
5. Akira, S. & Takeda, K. Toll-like receptor signalling. *Nat. Rev. Immunol.* **4,** 499–511 (2004).
6. Goodridge, H. S., Underhill, D. M. & Touret, N. Mechanisms of Fc Receptor and Dectin-1 Activation for Phagocytosis. *Traffic* **13,** 1062–1071 (2012).
7. Fitzer-Attas, C. J. *et al.* Fcγ Receptor–Mediated Phagocytosis in Macrophages Lacking the Src Family Tyrosine Kinases Hck, Fgr, and Lyn. *J. Exp. Med.* **191,** 669–682 (2000).
8. Zhu, J. W., Brdicka, T., Katsumoto, T. R., Lin, J. & Weiss, A. Structurally Distinct Phosphatases CD45 and CD148 Both Regulate B Cell and Macrophage Immunoreceptor Signaling. *Immunity* **28,** 183–196 (2008).
9. Beauchemin, N. & Arabzadeh, A. Carcinoembryonic antigen-related cell adhesion molecules (CEACAMs) in cancer progression and metastasis. *Cancer Metastasis Rev.* **32,** 643–671 (2013).

10. McNeill, L. *et al.* The differential regulation of Lck kinase phosphorylation sites by CD45 is critical for T cell receptor signaling responses. *Immunity* **27,** 425–437 (2007).
11. Zikherman, J. *et al.* CD45-Csk Phosphatase-Kinase Titration Uncouples Basal and Inducible T Cell Receptor Signaling during Thymic Development. *Immunity* **32,** 342–354 (2010).
12. Choudhuri, K., Wiseman, D., Brown, M. H., Gould, K. & van der Merwe, P. A. T-cell receptor triggering is critically dependent on the dimensions of its peptide-MHC ligand. *Nature* **436,** 578–582 (2005).
13. Varma, R., Campi, G., Yokosuka, T., Saito, T. & Dustin, M. L. T cell receptor-proximal signals are sustained in peripheral microclusters and terminated in the central supramolecular activation cluster. *Immunity* **25,** 117–127 (2006).
14. James, J. R. & Vale, R. D. Biophysical mechanism of T-cell receptor triggering in a reconstituted system. *Nature* (2012). doi:10.1038/nature11220
15. Schmid, E. M. *et al.* Size-dependent protein segregation at membrane interfaces. *Nat. Phys.* **advance online publication,** (2016).
16. Freeman, S. A. *et al.* Integrins Form an Expanding Diffusional Barrier that Coordinates Phagocytosis. *Cell* **164,** 128–140 (2016).
17. Katsumata, O. *et al.* Association of FcγRII with Low-Density Detergent-Resistant Membranes Is Important for Cross-Linking-Dependent Initiation of the Tyrosine Phosphorylation Pathway and Superoxide Generation. *J. Immunol.* **167,** 5814–5823 (2001).
18. Beekman, J. M., van der Linden, J. A., van de Winkel, J. G. J. & Leusen, J. H. W. FcγRI (CD64) resides constitutively in lipid rafts. *Immunol. Lett.* **116,** 149–155 (2008).
19. Gordon, S. Pattern Recognition Receptors. *Cell* **111,** 927–930 (2002).
20. Jacobs, S. A. *et al.* Design of novel FN3 domains with high stability by a consensus sequence approach. *Protein Eng. Des. Sel.* **25,** 107–117 (2012).
21. Ben M'Barek, K. *et al.* Phagocytosis of immunoglobulin-coated emulsion droplets. *Biomaterials* **51,** 270–277 (2015).
22. Crowley, M. T. *et al.* A Critical Role for Syk in Signal Transduction and Phagocytosis Mediated by Fcγ Receptors on Macrophages. *J. Exp. Med.* **186,** 1027–1039 (1997).
23. Turner, M., Schweighoffer, E., Colucci, F., Di Santo, J. P. & Tybulewicz, V. L. Tyrosine kinase SYK: essential functions for immunoreceptor signalling. *Immunol. Today* **21,** 148–154 (2000).
24. Systematic Comparison of Constitutive Promoters and the Doxycycline-Inducible Promoter. Available at: http://journals.plos.org/plosone/article?id=10.1371/journal.pone.0010611. (Accessed: 25th June 2017)
25. Jaumouillé, V. & Grinstein, S. Receptor mobility, the cytoskeleton, and particle binding during phagocytosis. *Curr. Opin. Cell Biol.* **23,** 22–29 (2011).
26. Chang, V. T. *et al.* Initiation of T cell signaling by CD45 segregation at 'close contacts'. *Nat. Immunol.* **17,** 574–582 (2016).

27. Nimmerjahn, F. & Ravetch, J. V. Divergent Immunoglobulin G Subclass Activity Through Selective Fc Receptor Binding. *Science* **310,** 1510–1512 (2005).
28. Jefferis, R. Glycosylation as a strategy to improve antibody-based therapeutics. *Nat. Rev. Drug Discov.* **8,** 226–234 (2009).

Chapter 4

Rapid, point-of-care quantification of *Loa loa* microfilariae in human whole blood with a mobile phone microscope

Michael V. D'Ambrosio[1*], Matthew Bakalar[1*], Sasisekhar Bennuru[3], Clay Reber[1], Arunan Skandarajah[1], Lina Nilsson[1], Neil Switz[1,2], Joseph Kamgno[4,5], Sébastien Pion[4,6], Michel Boussinesq[6], Thomas B. Nutman[3#], and Daniel A. Fletcher[1,2#]

[1]Department of Bioengineering and [2]Biophysics Group, UC Berkeley, Berkeley, CA; [3]Laboratory of Parasitic Diseases, National Institute of Allergy and Infectious Diseases, Bethesda, MD; [4]Center for Research on Filariasis and other Tropical Diseases, Yaoundé, Cameroon; [5]Faculty of Medicine and Biomedical Sciences University of Yaounde I, Yaounde Cameroon; [6]UMI 233, Institut de Recherche pour le Développement (IRD) and University of Montpellier, Montpellier, France

[*]Co-first authors

From D'Ambrosio, Bakalar et al. Point-of-care quantification of blood-borne filarial parasites with a mobile phone microscope. Science Translational Medicine *7*, 286re4-286re4 (2015).

Abstract:

Parasitic helminths cause debilitating diseases that affect millions of people in primarily low-resource settings. Efforts to eliminate onchocerciasis and lymphatic filariasis in Central Africa through mass drug administration have been suspended because of ivermectin-associated serious adverse events, including death, in patients infected with the filarial parasite *Loa loa*. To safely administer ivermectin for onchocerciasis or lymphatic filariasis in regions co-endemic with *L. loa*, a strategy termed "test and (not) treat" has been proposed whereby those with high levels of *Loa loa* microfilariae (>30,000/ml) that put them at risk for life-threatening serious adverse events are identified and excluded from mass drug administration. Here we demonstrate a mobile phone-based video microscope that automatically quantifies *L. loa* microfilariae in whole blood loaded directly into a small glass capillary from a finger prick, without the need for conventional sample preparation or staining. This point-of-care device automatically captures and analyzes videos of microfilarial motion in whole blood using a combination of motorized sample scanning and on-board motion detection that is coordinated and controlled by the phone, minimizing input from healthcare workers and providing a quantification of microfilariae per ml (mf/ml) of whole blood in under two minutes. To validate performance and usability of the mobile phone microscope, we tested 33 potentially *Loa*-infected patients in Cameroon and confirmed that automated counts correlated with manual thick smear counts (94% specificity; 100% sensitivity). Use of this technology to exclude patients from ivermectin-based treatment at the point of care in *Loa*-endemic regions would allow resumption/expansion of mass drug administration programs for onchocerciasis and lymphatic filariasis in Central Africa.

Introduction:

Diseases caused by the filarial nematodes *Loa loa, Onchocerca volvulus*, and *Wuchereria bancrofti* are a major public health and socio-economic burden in co-endemic regions of Africa. The severity of symptoms and long-term consequences for patients depend on both the parasite and the parasitic load. *L. loa*, the causative agent of loiasis, is highly endemic in Central Africa (Cameroon, Gabon, Republic of the Congo, Central African Republic, and Democratic Republic of the Congo, in particular). Although the manifestations of *L. loa* infection are often subclinical or relatively muted, including subconjunctival migration of an adult worm ('eyeworm') and/or transient angioedema (Calabar swellings), loiasis has been associated in some cases with serious renal, cardiac, and neurologic abnormalities (1,2). Onchocerciasis or "river blindness", caused by *O. volvulus*, is the second most common cause of infectious blindness worldwide and can result in disfiguring, highly pruritic skin disease (3). Lymphatic filariasis (LF), caused by *W. bancrofti*, is the second leading cause of disability worldwide, infecting 120 million worldwide and responsible for lymphedema, hydroceles, and elephantiasis (4).

To eliminate onchocerciasis and LF, mass drug administration (MDA) programs have been established to administer the antiparasitic drug ivermectin (IVM) for onchocerciasis and the combination of IVM and albendazole for LF. In Central Africa, individuals may be infected not only by *O. volvulus* and *W. bancrofti* but also by *L. loa*. Because IVM also acts on *L. loa* microfilariae (mf), treatment with IVM can induce serious adverse events (SAEs) in individuals with high circulating levels of *L. Loa* mf. When the levels exceed 30,000 mf/ml of blood, a potentially fatal encephalopathy can occur within 2-3 days after IVM administration (5), while long-term neurologic sequelae may occur in non-fatal cases. Individuals with more than 8,000 mf/ml but less than 30,000 mf/ml are also at risk for SAEs, including temporary functional

impairment that is primarily non-neurological and usually reversible (6). Some antibiotics, such as doxycycline, are effective against *O. volvulus* and *W. bancrofti* owing to their activity against the bacterial endosymbiont *Wolbachia* present in the parasites, but these antibiotics have no effect on *L. loa* since it does not harbor *Wolbachia*. Furthermore, these antibiotics require a daily regimen over 6 weeks and thus are impractical for MDAs campaigns (7–9).

Loa-associated SAEs have led to the suspension of IVM-based MDA programs in areas highly endemic for co-incident *L. loa* infection, representing a major setback for onchocerciasis and LF elimination campaigns (5,10). A potential solution to prevent *Loa*-associated SAEs is to identify those *Loa*-infected individuals at the highest risk for SAEs (>30,000 mf/ml) and exclude them from IVM-based MDA programs. This strategy, termed "test and (not) treat", requires a quantitative test for *L. loa* microfilariae that is rapid, inexpensive, and can be performed accurately at the community level.

Existing methods for quantifying parasitic microfilariae in blood are neither rapid nor suitable for point-of-care (POC) screening needed for MDA programs. The current 'gold standard' involves manual counting of individual microfilariae within a defined volume of blood in Giemsa-stained thick smears by a trained technician with a conventional light microscope (11). Preparation and reading of slides requires laboratory equipment not available in many field settings and typically takes at least a day to complete, making throughput unacceptably low for use as part of MDA programs, where patient follow-up is not practical. Alternate methods of microfilaria quantification have been developed, including molecular methods (e.g. qPCR) (12), but these methods are not only time intensive but also require transportation of samples to a centralized laboratory facility, use of expensive equipment and reagents, and significant training, making them inappropriate for POC use. A new approach for rapid, POC quantification of *L. loa* mf load is needed.

Here we present a mobile phone microscope that uses motion — the 'wriggling' motion of individual microfilariae — instead of molecular markers or stained morphology to count microfilariae in whole blood. This approach eliminates the need for complex molecular assays or sample preparation and staining, allowing automated quantification in minutes as opposed to hours or days. We show using Poisson statistics that our approach can achieve a false negative rate as low as a 1 in 10 million. We also show that quantitative results from our device are highly correlated with those from 'gold standard' microscopy of patients evaluated in Cameroon ($r=0.99$). Use of this technology as a tool for screening patients prior to treatment could enable resumption of IVM-based MDA programs in Central Africa.

Results

Automated counting of Loa loa microfilariae in whole blood

We developed a rapid method for quantifying *L. loa* microfilariae at the POC by video microscopy with a mobile phone. Our method is based on the 'wriggling' motion of live *L. loa* microfilariae, which can be seen in magnified time-lapse images of microfilariae isolated from blood samples (13) (Fig. 1A). We found that microfilarial movement can be detected in whole blood simply by observing the displacement of red blood cells surrounding the microfilariae in a thin (200 μm) imaging chamber (Fig. 1B, movie S1). This approach eliminates the need for

preparation and staining of blood samples to make the *L. loa* visible, and it permits the use of digital image processing to detect motion and automate microfilaria quantification.

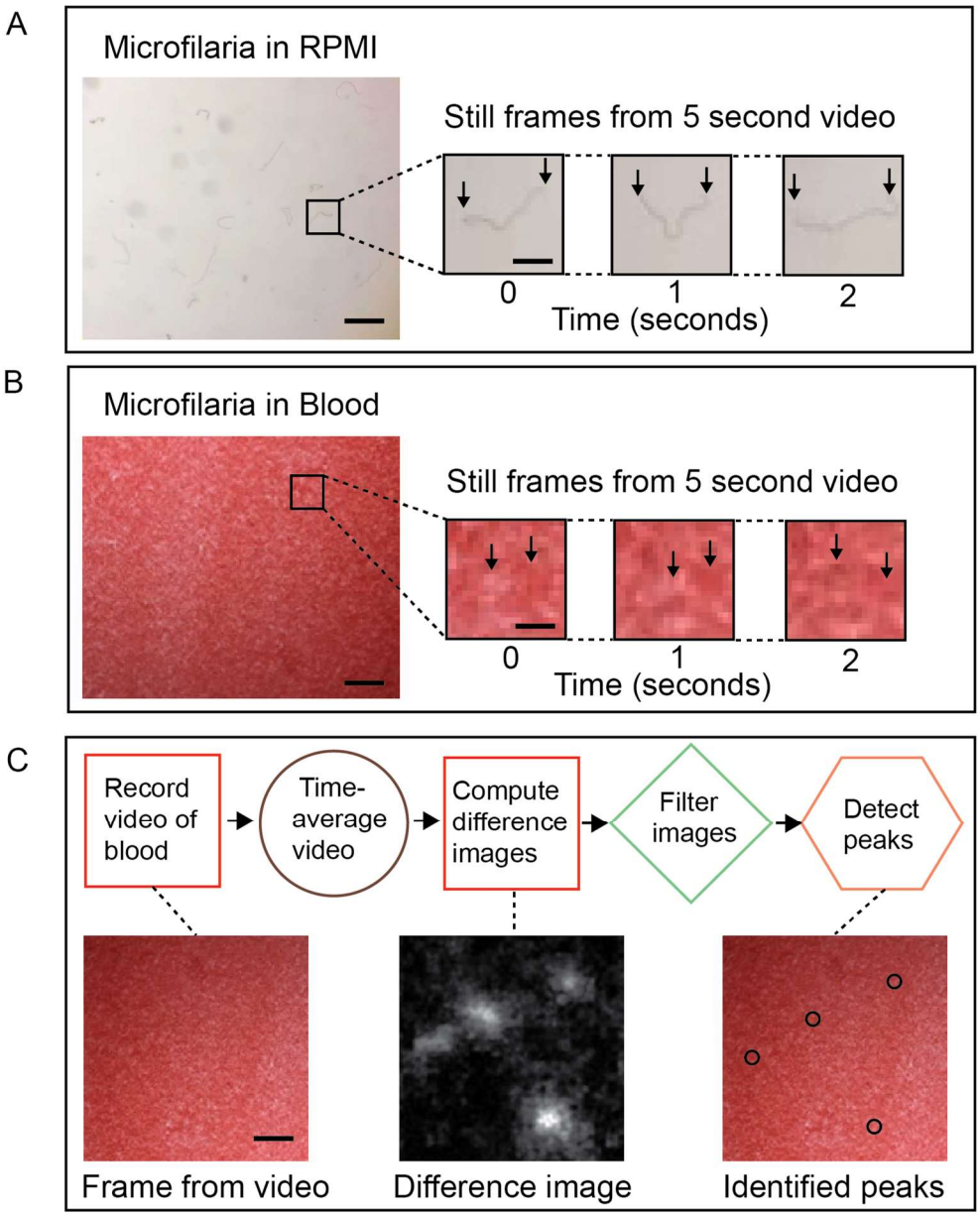

Figure 1. Strategy for quantifying mf in whole blood. (**A**) A single frame from a video of mf resuspended in RPMI medium, as well as a zoomed-in region of a single mf at 1, 2, and 3 s of the video. Scale bars, 500 and 100 µm (zoom). (**B**) A single frame of a video of mf in whole peripheral blood, as well as zoomed-in region of a single mf at 1, 2, and 3 s of the video. Arrows indicate differences in the images (see movie S1). (**C**) A single frame of a video taken of mf in whole peripheral blood, as well as difference image calculated by averaging, subtracting, and morphologically filtering subsequent frames of

the video, and mf localized within the FOV, which were quantified using a peak-finding algorithm on the processed difference image.

To rapidly determine the number of *L. loa* microfilariae in a magnified video of whole blood, we developed an image-processing algorithm that automatically identifies disturbances in the blood caused by moving microfilariae (Fig. 1C; movie S2). Briefly, the algorithm first subtracts subsequent frames of the video to generate a difference image, where regions of high intensity correspond to the motion of one or more microfilariae. Using a local peak-finding routine, the algorithm then localizes and counts the number of microfilariae within the 4 mm x 3.16 mm field of view (FOV) of the video. The algorithm was developed and optimized using a series of videos of *L. loa* microfilariae in whole blood collected from patients in Cameroon.

Capturing Loa loa microfilarial movement on a mobile phone

To capture microfilarial motion on a portable device suitable for MDA program use, we designed a compact video microscope with automated sample movement based around an Apple iPhone 5s (Fig. 2A). The device, which we refer to as the CellScope Loa, builds on recent progress using mobile phones for image-based diagnostics (14–18) and is the product of an iterative development process in collaboration involving engineers, clinicians, and local health workers in Cameroon. The CellScope Loa uses the camera of the iPhone 5s coupled with a reversed iPhone camera lens module for imaging and an LED array for illumination to form a simple bright-field video microscope with resolution of < 6.5 μm over a 4 mm × 3.16 mm FOV (17) (Fig. 2B). Wide-field imaging at this resolution is achieved by inverting a lens module from an iPhone 5s and positioning it adjacent to the iPhone 5s camera, resulting in an unmagnified image of the sample projected onto the phone's imaging sensor. Alignment of the mobile phone camera with the inverted lens module is achieved by sliding the unmodified mobile phone into a 3D-printed plastic case in which the lens module is embedded. The case also encloses the LED array, sample holder, battery, and control electronics. The movement of *L. loa* microfilariae (~200 μm in length) can be detected at any depth within a thin glass capillary (internal dimensions 4 mm wide, 200 μm deep, and 50 mm long). A video taken of a single FOV can be used to quantify the number of moving microfilariae within 2.59 μl of whole blood (Fig. 2C). In order to screen a larger volume of blood, additional fields of view are captured along the length of the capillary by driving the capillary, which is secured within a 3D-printed plastic carriage, along a linear rail by a servo motor. The servo motor and illumination array are controlled by an Arduino microcontroller board that is itself controlled by the mobile phone via Bluetooth.

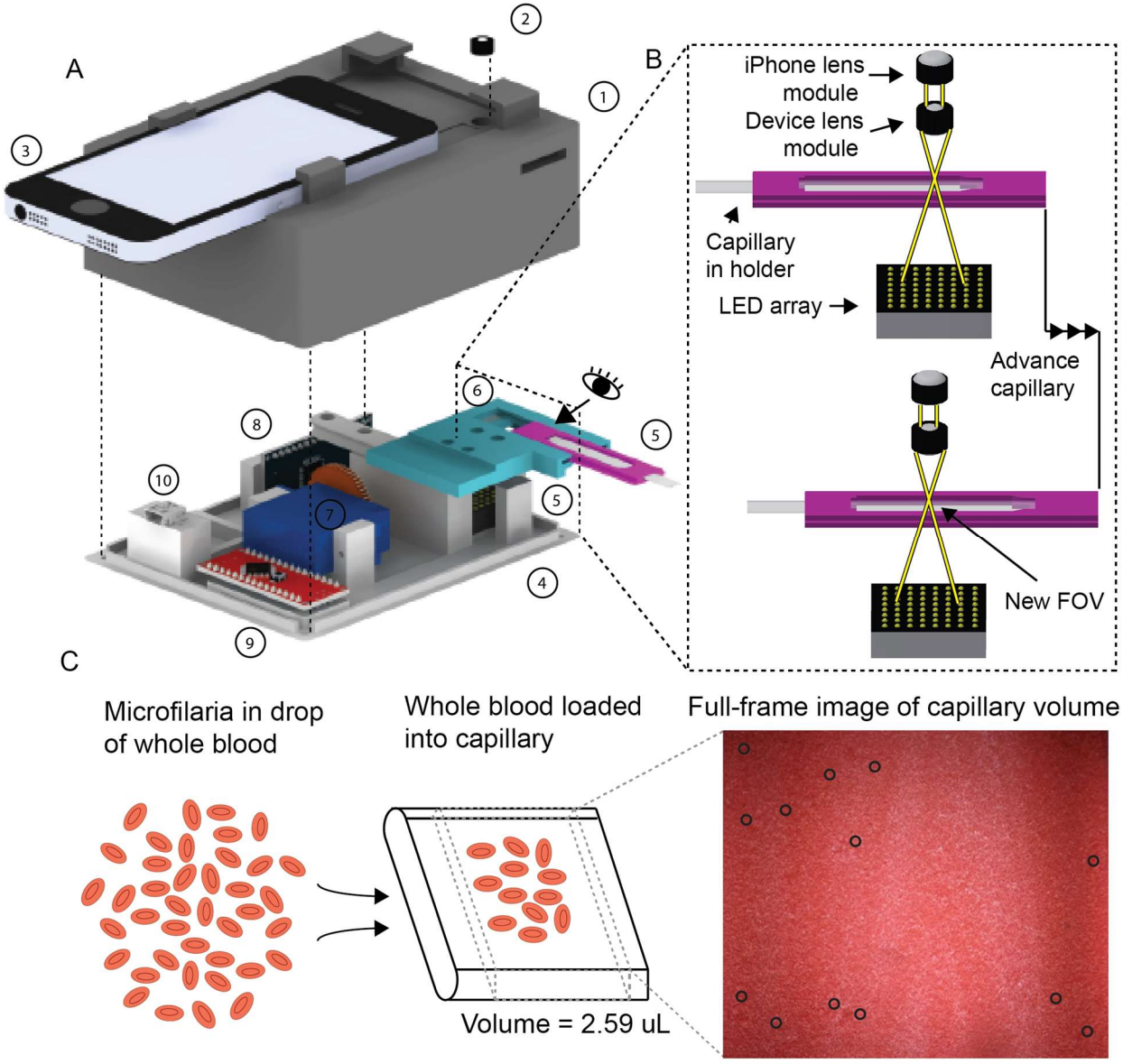

Figure 2. An automated cell phone–based video microscope. (**A**) A 3D-printed lid (i) aligns an isolated iPhone 5s cell phone lens module (ii) with the camera of a removable iPhone 5s (iii). A 3D-printed base (iv) positions a LED array directly beneath a capillary loaded with blood (v), which is mounted on a moveable carriage (vi). The carriage can slide along a single-axis rail driven by a rack coupled to its underside and a servo-mounted gear (vii), moving different regions of the capillary into the microscope FOV. An Arduino microcontroller board (viii) and a Bluetooth controller board (ix) communicate between the iPhone 5s, the servo, and the LED array. (x) A micro-USB (universal serial bus) port powers the device. (**B**) Simplified optical diagram of the microscope device. White light from the LED array illuminates the blood-loaded capillary. An isolated camera module from an iPhone 5s is inverted and positioned against the capillary. Light from the sample is collected by the inverted (objective) lens and then refocused by the optics of the iPhone 5s lens module onto the camera sensor. The capillary can be translated to position a new FOV into the optical path. (**C**) A video

acquired by the device captures microfilarial motion from a known volume of whole blood within a rectangular glass capillary. A still frame from a video of whole blood is shown (movie S1). Scale bar, 1 mm.

We wrote a custom iPhone app to control operation of the mobile phone microscope and enable one-touch counting of *L. loa* microfilariae in whole blood (movies S2 and S3). After the capillary with whole blood is loaded and a sample ID entered, the app moves the capillary into the device and focuses on the first FOV. A 5-second movie is automatically captured and analyzed on the phone by the algorithm described above, and the capillary is then moved to the next FOV to repeat the process for each FOV imaged. Each iteration of imaging and analysis takes in total <8 seconds. After the final FOV is imaged, the results (microfilariae per ml of blood, or mf/ml) are presented to the user within 5 seconds. Total time from insertion of the capillary to presentation of results is < 2 minutes. An additional minute is required to load finger-prick blood into the capillary and remove the capillary after test completion.

Statistical confidence in results from < 15 µl of blood

To determine the total blood volume that must be imaged to accurately exclude patients with high *L. loa* loads from IVM-based MDA, we considered the probability of observing k microfilariae within a volume v given a true sample concentration ρ mf/ml (19). According to Poisson statistics, the distribution of estimated *Loa* mf concentration k/v becomes more closely distributed around the true sample concentration ρ as the volume v increased (Fig. 3A). As a result, for an individual patient, the probability that the true microfilaria load is above the SAE threshold of 30,000 mf/ml but the estimated microfilaria load based on the total number of imaged FOVs is below the treatment threshold – a false negative, which would lead to treatment of a patient at risk for SAE – decreases with increasing number of FOV (Fig. 3B).

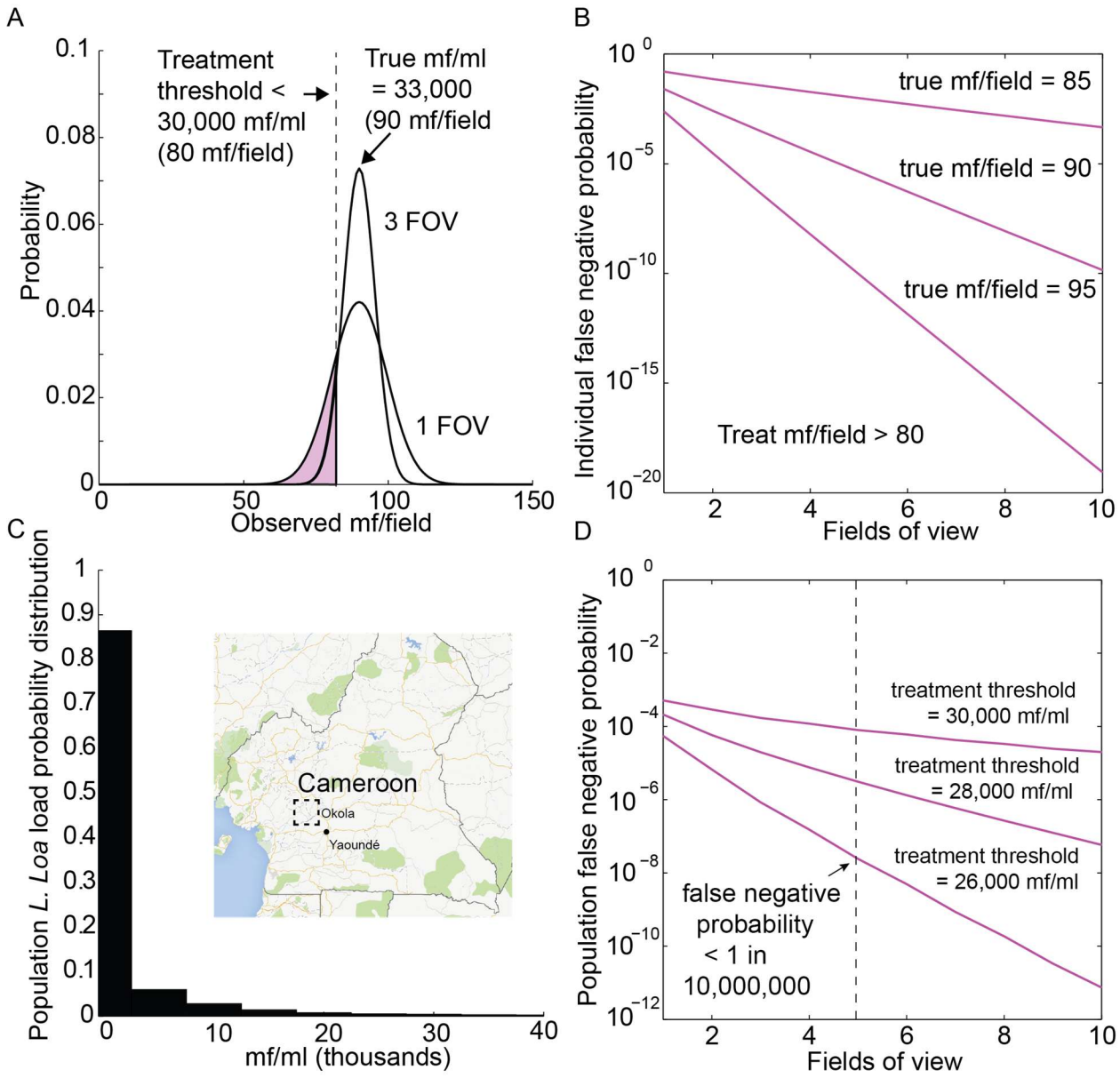

Figure 3. Predicted counting statistics for *L. loa* diagnostic decisions.

(**A**) For a patient with a load of 30,000 mf/ml, the distribution of observed mf/ml sampled in the small blood volume within the capillary obeyed Poisson statistics, such that any measurement of mf/ml load fell either below or above the true mf/ml. A treatment threshold defined the estimated mf/ml above which a patient was excluded from testing. If the true mf/ml was higher than the treatment threshold and the measured mf/ml was lower than the threshold, the measurement was a false negative (purple regions). (**B**) For a patient with a given true mf/ml, increasing the number of FOVs captured on the device decreased the probability of false negatives. (**C**) Probability density function of *L. loa* infection load within the target population around Okola, Cameroon ($n = 2000$). (**D**) Impact of increasing the number of captured FOVs on the probability of false negatives within the Okola population. To decrease the risk of false-negative tests, the treatment threshold can be lowered beneath the load at which severe adverse events are triggered

(treatment threshold < SAE threshold of 30,000 mf/ml). Using a treatment threshold of 26,000 mf/ml over five observed FOVs yields a false-negative probability below 1×10^{-7} (1 test in 10,000,000). (**E**) For a patient with a given true mf/ml, increasing the number of FOVs captured on the device decreases the probability of false positives. (**F**) Impact of increasing the number of captured FOVs on the probability of false positives within the Cameroonian population. To decrease the risk of false-positive tests, the treatment cutoff can be lowered beneath the load at which severe adverse events are triggered (treatment cutoff < SAE cutoff of 30,000 mf/ml). Using a treatment cutoff of 26,000 mf/ml over five observed FOVs yields a false-positive rate below 1×10^{-3} (1 test in 1000).

To estimate the rate of false negatives within the target population (population false negative), we constructed a probability density function of measured *L. loa* microfilaria load within the target community from thick blood smears collected from 2000 patients in Okola, Cameroon and read using manual 'gold standard' microscopy (Fig. 3C). Integrating individual patient risk over the population, we estimated a false-negative probability for our mobile phone video microscope of less than 1 in 10 million patients (0.00001%) when imaging 5 FOVs, corresponding to a volume of 13.7 μL, using the SAE threshold of 30,000 mf/ml and a treatment threshold of 26,000 mf/ml (patients with measured microfilaria loads above the treatment threshold are excluded from treatment) (Fig. 3D). The false negative probability could be decreased arbitrarily by further lowering the treatment threshold below the SAE threshold, at the expense of increasing false positives – patients whose true microfilaria load is below the SAE but whose measured microfilaria load causes them to be excluded from treatment (Fig. 3E, 3F).

Validation of automated screening of Loa-infected patients in Cameroon

To evaluate the accuracy and ease of use of the mobile phone video microscope, 33 potentially *Loa*-infected subjects in Cameroon were tested with the CellScope Loa, and their results were compared to results obtained by manual 'gold standard' microscopy of thick blood smears. This pilot study was approved by the National Ethics Committee of Cameroon, and tests were performed by both visiting scientists and local doctors and technicians. A flow-chart of the procedure used for the test are shown in Fig. 4A. After obtaining written informed consent, the patient's peripheral blood from a finger prick was drawn into two rectangular capillaries (2.59 μl each) and loaded into two devices to obtain duplicate measurements. The CellScope Loa operator initiated *Loa* microfilaria counting with one touch in the custom app, and the device automatically collected, imaged, analyzed, and quantified five independent FOVs in fewer than two minutes (movie S3). Capillary blood was also collected from each patient to carry out "gold standard" smear microscopy and manual counting for comparison. Thick smears were made and dried after collection, and the samples were transported to a central laboratory for staining and reading by two independent technicians who were blinded to the results from CellScope Loa.

The microfilaria load measured by the mobile phone video microscope correlated strongly with the results from manually-counted thick blood smears of the same patients (r=0.99) (Fig. 4B), indicating agreement with the 'gold standard' method. Two blood smears read by two technicians and two capillaries read by two CellScope Loa devices were averaged for each patient. The absolute mf/ml count from the CellScope Loa were scaled by a constant linear factor (m = 0.43) relative to the thick blood smear (Fig. 4C). We speculate this difference is the result of a constant non-motile fraction of the microfilaria population that is seen in stained thick

smears but not observable in our device, as well as a loading bias into the capillary due to its size and shape. Incorporating this scaling factor, the device achieved a sensitivity of 100% for patients above the SAE threshold of 30,000 mf/ml and a specificity of 94% relative to thick blood smear. There were 0 false negatives (patients with an actual microfilarial loads over 30,000 mf/ml that CellScope Loa counted as below the 26,000 mf/ml treatment threshold) and 2 false positives (patients with an actual microfilaria load below 30,000 mf/ml that CellScope Loa counted as above the 26,000 mf/ml cutoff). Automated counts made by the motion detection algorithm also correlated with those from manual counts of the same movies from two blinded observers (r=0.99, Fig. 4D), and the output of the two duplicate CellScope Loa tests were highly correlated (r=0.96), indicating repeatability of the test (Fig. 4E). Together these results demonstrate that rapid and accurate quantification of moving *L. Loa* microfilariae in peripheral blood is possible at the POC.

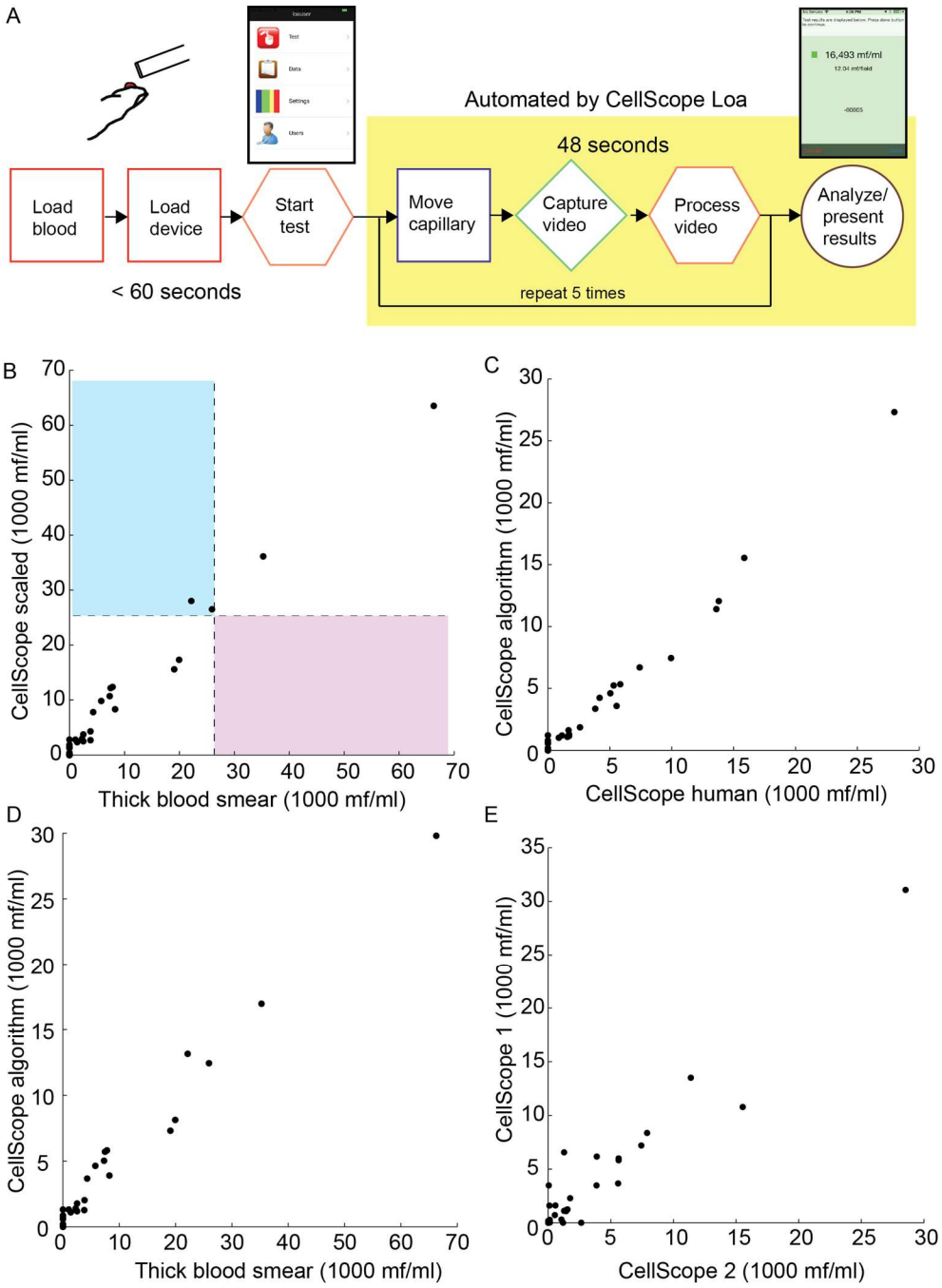

Figure 4. Results of a pilot study conducted in Cameroon to assess the effectiveness of the device.

(**A**) Flowchart describing the test procedure for the device. (**B**) Blood smear versus CellScope Loa quantifications of mf load. Results from two CellScope Loa readings of the same patient are averaged and scaled by a linear correction factor (**Fig. 4C**). Results from two thick blood smears are also averaged. $r = 0.99$. Purple region corresponds to false negatives (that is, patients whom CellScope Loa assessed with 99.99% certainty were under the SAE threshold but were actually over the threshold as assessed by blood smear). Blue-shaded region corresponds to false positives (that is, patients whom

CellScope Loa could not confidently guarantee were under the SAE threshold of 30,000 mf/ml but actually were under the SAE threshold as assessed by blood smear). The lower left quadrant corresponds to true negatives (that is, patients whom CellScope Loa assessed with 99.99% certainty were under the SAE threshold and were also under the SAE threshold as assessed by blood smear). The upper right quadrant corresponds to true positives (that is, patients whom CellScope Loa determined were above the SAE threshold of 30,000 mf/ml and were confirmed to be over the SAE threshold as assessed by blood smear). (**C**) Calculation of the correction factor. A linear fit between CellScope and calibrated thick-smear counts was performed to determine the correction factor *m*. Results from two CellScope Loa readings were averaged. (**D**) Comparison of blinded human counts of whole-blood movies to automated CellScope Loa counts. CellScope Loa and human counts from two readings are averaged. (**E**) Repeatability of CellScope Loa measurements. Two blood samples were taken from each patient ($n = 33$) and read by separate devices with blinded separate operators using the automated algorithm ($r = 0.96$).

Discussion

The screening technology presented here takes advantage of the decreasing cost and increasing computational and imaging capabilities of mobile phones to create a mobile phone video microscope that provides rapid and accurate quantification of *L. loa* microfilariae at the POC. By detecting microfilarial motion in whole blood rather than staining for morphology or screening for molecular markers, our device is able to provide results in minutes – while the patient remains in the testing area prior to receiving treatment – and requires neither substantial training on the part of the healthcare worker nor a custom disposable element. Pilot testing in Cameroon demonstrated excellent correlation (r=0.99) with gold standard microscopy. By using a treatment cutoff (26,000 mf/ml) below the SAE cutoff (30,000 mf/ml), we could ensure a low false negative rate at the expense of an increased false positive rate, as reflected in our pilot study where there were 0 false negatives and 2 false positives. Since the consequences for false negatives are much greater than for false positives, use of a treatment cutoff may be an effective strategy for minimizing SAEs in IVM-based MDA programs in Central Africa.

In addition to diagnostic speed and accuracy, our mobile phone video microscope offers several important advantages for POC microfilaria quantification over manual 'gold standard' microscopy and PCR. First, no sample preparation of the blood is required—simply a finger prick—thus limiting the potential for staining and dilution errors and sample loss during handling. Second, the primary consumables used for each patient are a single glass capillary and a lancet, both off-the-shelf items, ensuring the recurring cost of testing is low (< $1 USD). In addition to one-touch imaging and microfilaria quantification, the CellScope Loa app manages patient information, records test results, and uploads data to an off-site server for long-term storage and quality assessment. Use of automated image collection and processing avoids issues that affect the reliability of human readers, including fatigue and distraction, and the device can be operated with minimal training, an important consideration in a large MDA program. In addition, this device provides an immediate way to collect and organize individual subject data and to track metadata, such as microfilaria loads at different geographic locations, for subsequent epidemiological analysis.

The CellScope Loa device design reported here, which uses an automated sample stage and a compact reversed lens optical system (17), was built to address issues identified during field testing of our initial prototype mobile phone video microscope, which used a manual stage and was based on a previously developed folded objective-based system (18). In the initial prototype, blood was loaded into the same capillary for imaging, but the capillary was advanced by manually turning a wheel. Based on initial tests in Cameroon, we found that only 85% of the videos from the initial prototype (200 total videos) could be successfully analyzed, as opposed to 98% with the automated device presented here (not counting automatically excluded videos). The failure modes were (i) residual flow in the capillary that led to miscounting of microfilariae (73% of errors), (ii) incorrect focus or illumination (15% of errors), and (iii) bumps of the device and inappropriate manual capillary advancement (12% of errors). To address these failure modes, we (i) implemented flow detection in the automated analysis algorithm to exclude regions of the video with high residual flow, (ii) implemented automated illumination and focus control, and enclosed the sample imaging area so the device could be used outside in daylight, and (iii) made the device smaller and more stable to avoid image artifacts caused by accidental bumps, as well as automated image collection and sample scanning to minimize errors caused by inaccurate or incomplete advancement of the capillary. We also modified the software user interface to enable one-touch completion of the assay (movies S2 and S3), and improved the video analysis software to increase accuracy and avoid blood movement artifacts identified in movies taken with the initial prototype. Testing of the initial prototype by healthcare workers in field settings was a critical part of the design process that resulted in the automated CellScope Loa presented here.

Our device differs from other mobile phone-based diagnostics in that it combines video microscopy with automated sample scanning and a field-validated on-board quantitative detection algorithm in a compact and portable design that is easy for minimally trained for healthcare workers to use. The CellScope Loa device presented here could also be useful for screening and quantification of other motile blood-borne infectious agents such as trypanosomes and other filariae. *Wuchereria bancrofti*, expected to be found in numbers up of 1000 mf/ml, may be detected by performing a similar assay at night, when their microfilariae are at their peak n the peripheral circulation. *Mansonella perstans,* which has no periodicity, would be difficult to differentiate from *L. loa* with our assay. However, heavy parasitemia of *Mansonella perstans* is very rare and thus would be unlikely to have a significant influence on the clinical decision made about a patient with a *L. loa* load of 30,000 mf/ml. Further studies would be necessary to determine if microfilariae could be speciated by the motion patterns they produce. Only a single trypanosome would likely be seen within the volume of this particular assay and would exhibit a significantly different movement pattern, limiting the potential for skewed *L. loa* quantification by the presence of trypanosomes. However, a modified image processing algorithm and assay incorporating sample concentration or larger volumes may be useful for detecting trypanosomes. Mobile phone-based microfilaria quantification has the potential to enable safe and effective MDA control programs for onchocerciasis and lymphatic filariasis at the POC in regions where *L. loa* is endemic. Using the CellScope Loa, a team of three individuals could screen up to 200 patients during the 4-hour (10AM-2PM) window when *L. loa* circulates at its peak in peripheral blood (1). Target areas for future use of the technology includes regions co-endemic with *Loa* and other filariae, including parts of Nigeria, Cameroon, Central African Republic, DR Congo, Congo, and Equatorial Guinea (5). Scale-up of the technology for broader use will require development beyond

the prototype presented here, including design for manufacturing and cost reduction engineering, as well as additional testing to verify performance of a production device. While few existing regulatory barriers beyond approvals already obtained would prevent the use of this technology as part of an MDA program, FDA approval would be needed if the device were to be used in the United States. To date, the FDA has approved multiple mobile-phone based medical devices, setting a precedent for the use of mobile phones in regulated healthcare applications (20). The device reported here provides an example of how mobile phone technology can be used to address critical gaps in the treatment of neglected tropical diseases.

Methods:

We evaluated *L. loa* mf density in whole blood of 33 *Loa*-infected subjects from the region surrounding Yaoundé, Cameroon using the mobile phone video microscope. Protocols for this pilot study were approved by the National Ethics Committee of Cameroon (P. O. Box 1937, Yaoundé, Cameroon) and written informed consent was obtained for each subject. Rules for stopping data collection after 300 subjects, over a number of discrete trails, were in place. Data from a subset of these subjects, comprising the complete initial trial of the CellScope Loa, are presented here. Study requirements were that individuals were living in a *L. Loa* endemic region and were willing to participate, were greater than 6 years old, and were able to give consent (or, in the case of minors assent with consent of parent/guardian). A disposable lancet was used to prick the finger of each patient, and peripheral blood from the finger prick was drawn into two rectangular capillaries. Each capillary was loaded into a device, and a series of videos were taken and analyzed by the mobile phone software app. Blood was also obtained from each patient for analysis by the gold standard (thick-smear) method for microfilaria quantification. The two minutes needed to screen a patient for SAE risk with the mobile phone video microscope included time to fill the capillary with blood, load the capillary into the microscope, trigger the software app to collect a series of videos, and receive the results from automated image processing.

Of the 300 (5 or10 videos per patient, 33 patients) videos collected in this study, 16 videos, from 4 patients, were excluded from this analysis. Ten videos from 2 patients were automatically rejected by the algorithm for inconsistent counts between FOVs. An additional 6 videos were excluded manually, 5 due to an illumination malfunction likely due to a poor solder joint, and 1 due to a malfunction with the camera initialization in software. Note that the 6 manual exclusions were made after the scaling factor was calculated. If the scaling factor were instead calculated after the exclusions, it would have been 0.45. Both malfunctions have been fixed by repairing the wiring and installing a software update. All videos used in the data analysis followed a standard protocol where freshly drawn blood was analyzed.

Mobile phone video microscope

The mobile phone video microscope used in this study, which we refer to as the CellScope Loa, was built from a reversed iPhone camera lens module, a linear rail and carriage (McMaster Carr), a hobby servo (Hitec 8045), an Arduino Micro (Adafruit), a Bluetooth communication Board (RedBear Labs), and a 3D printed plastic body (Fig. 2, A and B). The 3D printed body aligned the iPhone 5s camera over the lens module. All 3D printed parts were produced on a Dimension uPrint 3D printer, and require a printing resolution of 200 μm. A glass capillary (VitroCom) was press fit into a 3D-printed holder. When inserted into the device, this holder was held in the

correct position by a pair of neodymium magnets. The servo and linear rail then translated the sample across the lens by one FOV when triggered by the iPhone over Bluetooth. Custom control software for the Arduino was written in C. All software is available in a public GitHub repository (www.github.com/cellscopeloa).

Mobile phone software app

The software was created using the Apple developer tools, although similar applications could be written in multiple other languages based on the steps outlined below. A mobile app running on the iPhone 5s guides the user to load the sample into the device and acquire a series of five-second videos, one for each new field-of-view along the capillary. Image-processing (described below) of the videos to identify microfilariae begins immediately upon acquisition, and when finished, the app presents the user with a summary of the test results (counted microfilariae, treat or not-treat). Each video is stored on the phone along with the results of the counting algorithm. The date and time of acquisition, current GPS coordinates, and a unique patient identifier are also stored with the test results. All results can be uploaded from the field to a password protected central database, where they are immediately available for further analysis or quality control. After the movies were taken, the app automatically began processing them in the background using the algorithm described below.

Automatic image processing to detect microfilaria motion

The algorithm first subtracted subsequent frames of the video and summed them to generate a single difference image. From that summed difference image, the background was estimated by taking the lowest value after it was blurred using a convolution operation using a 5 by 5 Gaussian kernel to smooth image noise. The original five-second video was divided into five one-second videos, and a summed difference image is created for each one-second video. These 1-second summed difference images were blurred using a median filtering and a 5 by 5 Gaussian convolution operation to smooth image noise. A second convolution with a mean-subtracted Gaussian is applied to enhance worm-like difference fields. The algorithm then uses a local peak-finding routine to scan the entire image with a 17 by 17 pixel box, designed to allow each mf to have only one maximum, and sums the number of independent positions within the FOV. Farneback motion estimation can optionally be used to detect directional flow within the capillary and eliminate false worm identification, and was used for the results reported in this paper (21). This process was repeated for all five 1-second summed difference images, and the average number of microfilaria was reported. This algorithm was implemented using the C++ interface for OpenCV 2.4 and run on the iPhone 5s.

Statistical analysis of volume imaged

Each video from the mobile phone microscope samples a region of the capillary that contains 2.59 µl of whole blood. We sought to understand how the probabilities of false negatives and false positives were affected by examining larger volumes of blood, achieved by imaging multiple fields of view. For each patient with a mean density of mf/ml ρ, there exists a true mean $N = \rho v$ that corresponds to the mean number of mf contained within an observation volume of blood v. The probability that a measured number of mf k is observed within a volume v from a sample with a true mf density ρ derives from a Poisson probability distribution around the true mean N:

$$Prob(k, N) = \left(N^k e^{-(N)}\right)/k!$$

The probability that an observation k falls between 0 and an upper value u is computed:

$$Prob(0 \leq k \leq u, N) = \sum_{k=0}^{u} Prob(k, N)$$

To compute the probability of a patient's true mf density ρ falling above the SAE threshold of 30,000 mf/ml when the observed number of mf k within the observation volume v is below a given 'no treatment' threshold t within that same observation volume (false negative), we integrate across all observations (k, N) for all possible N, weighted by the probability of N within the target population:

$$Prob(False\ negative) = Prob(0 \leq k \leq t, N \geq 30{,}000v)$$

$$Prob(False\ negative) = \sum_{N=30{,}000v}^{\infty} \sum_{k=0}^{t} Prob(N) * Prob(k, N)$$

Similarly, we compute the probability that a patient's true mf density ρ falls below the SAE threshold of 30,000 mf/ml while the observed number of mf k is above the 'no treatment' threshold t (false positive) according to:

$$Prob(False\ positive) = Prob(k \geq t, N < 30{,}000v)$$

$$Prob(False\ positive) = \sum_{N=0}^{30{,}000v} \sum_{k=t}^{\infty} Prob(N) * Prob(k, N)$$

References:

1. Boussinesq M. Loiasis. Ann Trop Med Parasitol. 2006 Dec;100(8):715–31.
2. Metzger WG, Mordmüller B. Loa loa—does it deserve to be neglected? Lancet Infect Dis. 2014 Apr;14(4):353–7.
3. Basáñez M-G, Pion SDS, Churcher TS, Breitling LP, Little MP, Boussinesq M. River blindness: a success story under threat? PLoS Med. 2006 Sep;3(9):e371.
4. Zeldenryk LM, Gray M, Speare R, Gordon S, Melrose W. The emerging story of disability associated with lymphatic filariasis: a critical review. PLoS Negl Trop Dis. 2011 Dec;5(12):e1366.
5. Gardon J, Gardon-Wendel N, Demanga-Ngangue, Kamgno J, Chippaux JP, Boussinesq M. Serious reactions after mass treatment of onchocerciasis with ivermectin in an area endemic for Loa loa infection. Lancet. 1997 Jul 5;350(9070):18–22.
6. Boussinesq M, Gardon J, Kamgno J, Pion SD, Gardon-Wendel N, Chippaux JP. Relationships between the prevalence and intensity of Loa loa infection in the Central province of Cameroon. Ann Trop Med Parasitol. 2001 Jul;95(5):495–507.
7. Turner JD, Tendongfor N, Esum M, Johnston KL, Langley RS, Ford L, et al. Macrofilaricidal activity after doxycycline only treatment of Onchocerca volvulus in an area of Loa loa co-endemicity: a randomized controlled trial. PLoS Negl Trop Dis. 2010;4(4):e660.
8. Brouqui P, Fournier PE, Raoult D. Doxycycline and eradication of microfilaremia in patients with loiasis. Emerg Infect Dis. 2001;7(3 Suppl):604–5.
9. Taylor MJ, Makunde WH, McGarry HF, Turner JD, Mand S, Hoerauf A.

Macrofilaricidal activity after doxycycline treatment of Wuchereria bancrofti: a double-blind, randomised placebo-controlled trial. The Lancet. 2005 Jun 24;365(9477):2116–21.
10. Boussinesq M, Gardon J, Gardon-Wendel N, Chippaux J-P. Clinical picture, epidemiology and outcome of Loa-associated serious adverse events related to mass ivermectin treatment of onchocerciasis in Cameroon. Filaria J. 2003 Oct 24;2(Suppl 1):S4.
11. Moody AH, Chiodini PL. Methods for the detection of blood parasites. Clin Lab Haematol. 2000 Aug 1;22(4):189–201.
12. Fink DL, Kamgno J, Nutman TB. Rapid Molecular Assays for Specific Detection and Quantitation of Loa loa Microfilaremia. PLoS Negl Trop Dis. 2011 Aug 30;5(8):e1299.
13. Storey B, Marcellino C, Miller M, Maclean M, Mostafa E, Howell S, et al. Utilization of computer processed high definition video imaging for measuring motility of microscopic nematode stages on a quantitative scale: "The Worminator." Int J Parasitol Drugs Drug Resist [Internet]. [cited 2014 Oct 5]; Available from: http://www.sciencedirect.com/science/article/pii/S2211320714000232
14. Breslauer DN, Maamari RN, Switz NA, Lam WA, Fletcher DA. Mobile Phone Based Clinical Microscopy for Global Health Applications. PLoS ONE. 2009 Jul 22;4(7):e6320.
15. Tseng D, Mudanyali O, Oztoprak C, Isikman SO, Sencan I, Yaglidere O, et al. Lensfree microscopy on a cellphone. Lab Chip. 2010;10(14):1787.
16. Bogoch II, Andrews JR, Speich B, Utzinger J, Ame SM, Ali SM, et al. Mobile Phone Microscopy for the Diagnosis of Soil-Transmitted Helminth Infections: A Proof-of-Concept Study. Am J Trop Med Hyg. 2013 Apr 3;88(4):626–9.
17. Switz NA, D'Ambrosio MV, Fletcher DA. Low-cost mobile phone microscopy with a reversed mobile phone camera lens. PloS One. 2014;9(5):e95330.
18. Skandarajah A, Reber CD, Switz NA, Fletcher DA. Quantitative Imaging with a Mobile Phone Microscope. PLoS ONE. 2014 May 13;9(5):e96906.
19. Miles RE. On the homogeneous planar Poisson point process. Math Biosci. 1970;6:85–127.
20. U.S. Food and Drug Administration. Examples of MMAs the FDA Has Cleared or Approved [Internet]. 2014. Available from: http://www.fda.gov/MedicalDevices/ProductsandMedicalProcedures/ConnectedHealth/MobileMedicalApplications/ucm368784.htm
21. Farnebäck G. Two-Frame Motion Estimation Based on Polynomial Expansion. In: Bigun J, Gustavsson T, editors. Image Analysis [Internet]. Springer Berlin Heidelberg; 2003 [cited 2015 Jan 28]. p. 363–70. Available from: http://link.springer.com/chapter/10.1007/3-540-45103-X_50

Chapter 5 – Concluding Remarks

Immune-cells have the difficult task of identifying threats to the body in a sea of complex information. This task is made even more challenging by evolutionary competition – targets of the immune-system gain a survival advantage by avoiding detection. Although there has been extensive work cataloguing the identity of immune-receptors and their conjugate molecular patterns, new receptors and receptor-targets are being identified still to this day. Importantly, immune receptors are physically constrained by the two-dimensional surface of the cell membrane, and many of the ligands that form molecular patterns are similarly constrained on a target surface. These physical constraints change the way in which molecules interact, and can have dramatic consequences on their spatial organization. When coupled to intracellular signaling modules, the two-dimensional spatial organization of a membrane-bound receptor can control the difference between activation and quiescence of a cellular immune response.

In Chapter 2, I described a simple mechanism for spatially segregating proteins at the interface between two cell membranes that depends on the physical constraints of membrane proteins. When membranes are brought into close-contact by binding between adhesion proteins, the distance between the membranes is defined by the height of the adhesion complex stapling them together. For proteins that are taller than this height, the membrane must physically bend above them in order to accommodate them sterically. However, on a fluid membrane, proteins can also diffuse out of the contact zone to a region where there is no membrane-ceiling to push against, resulting in spatial segregation of tall proteins from regions of close-contact.

Using cell-free reconstitution of membrane-membrane adhesion, we show that this process is extremely sensitive to the relative height between a protein and the interface, with proteins that are > 5 nm taller than the membrane interface completely excluded at equilibrium. Interestingly, the 5-nm segregation scale is similar to the height of one of the building blocks of extracellular proteins, the Ig domain (3.5 - 4 nm). As a consequence, at any cell-cell interface receptors of diverse heights will be subject to different localization depending on their heights and affinities. In the future, it will be interesting to understand how the relative height, concentration, and affinity of binding-proteins at the cell-surface before formation of a cell-cell contact sets up the competition to position the membrane at the optimal binding height for each protein.

Chapter 3 explored the consequences of size-dependent protein segregation at the interface between a macrophage and a phagocytic target on effector cell activity. The Fc-receptor-antibody complex presents an interesting test of the theory described in Chapter 2. An antibody is raised against a foreign antigen, and its binding epitope and binding geometry relative to the target cell surface are completely unknown to an effector cell that encounters it bound to a target surface. This means that effector cells encounter antibody-FcR complexes that span a range of heights. How does this change in macrophage-target membrane-membrane distance, which is inherent to antibody-Fc binding, impact phagocytosis? Chapter 2 suggests that the spatial organization of both membranes, macrophage and target, will be influenced by the change in membrane-membrane contact height.

As it turns out, FcγR-dependent phagocytosis is modulated by the height of antibody display above a target cell-surface - antigens that position an antibody < 10 nm from cell-surface are optimal for stimulating phagocytosis. The critical requirement for FcγR signaling is close contact between a macrophage and target surface. Close contact physically forces the reorganization of proteins on the macrophage cell surface: tall proteins are pushed out by the small membrane-membrane gap. On the macrophage, the inhibitory phosphatase CD45 is critically segregated from the interface, releasing the brakes on downstream signaling and phagocytosis.

This observation suggests a number of directions for developing more effective therapeutics that depend on Fc-receptor signaling. Most clearly, if an antibody must be positioned close to the cell surface in order to trigger phagocytosis, then monoclonal antibodies (mAb) must be targeted to short, rather than tall antigens, for maximum therapeutic benefit. This hypothesis can be easily tested in the context of anti-cancer mAb therapy both *in vitro* and *in vivo* by carefully designing a target antigen on the surface of a tumor cell to display a common epitope at multiple heights. One parameter that we have not explored in the reconstituted system is what happens when you bind an antibody to the bottom of a tall protein. It might be that rather than eliminating all tall tumor-specific antigens as potential targets of mAb therapy, it is simply critical to consider antibody binding site, in addition to antigen physical characteristics, to get the maximum activity.

The theory of size-dependent physical segregation describes a mechanism that cells use to transduce changes in membrane-membrane distance into changes in lateral protein organization. This idea might be more broadly useful for manipulating the surface state of cells for therapeutic benefit. Signaling by inhibitory PRRs such as SIRPα allows tumor cells to evade immune detection by upregulating the ligand CD47, tricking macrophages into recognizing cancer as healthy self. In research that is part of the UC Berkeley Immunotherapeutics and Vaccine Research Initiative funded by Aduro Biotech, we are exploring a strategy for defeating this aberrant “recognition of self” by hijacking the process of size-dependent segregation. The fundamental idea is this: if an inhibitory PRR or its ligand is forced to co-segregate with CD45 away from the macrophage-target contact site it will be unable to signal, and activating PRRs will trigger productive phagocytosis. This can be accomplished with bispecific, non-blocking antibodies that are co-targeted to CD47 and a tall tumor cell-surface protein (Figure 1). Because they are non-blocking, they are only active when bound to CD47 at the tumor cell-surface, where binding to tall surface proteins changes the effective height of CD47 and forces its segregation, and not on healthy blood cells or tissue. These reagents can be targeted to different cancer cell-types by selecting a unique cell-surface protein for bispecific binding.

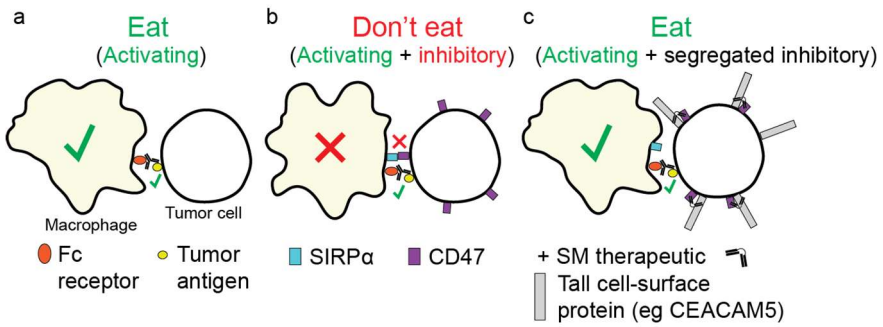

Figure 1: Disrupting macrophage inhibitory signaling by hijacking size-dependent segregation. (a) Tumor cells opsonized with IgG are phagocytosed due to interactions with macrophage Fc receptors. **(b)** Tumor-expressed CD47 binds to macrophage SIRPα to send a 'don't eat me' signal, outcompeting the pro-phagocytic signal through Fc receptors. **(c)** Bispecific antibodies link CD47 to a tall cell-surface protein (eg CEACAM5), forcing the segregation of CD47 from the tumor-macrophage contact site, disrupting the 'don't eat me' signal, and resulting in productive phagocytosis

The aim of Chapter 2 and 3 was to describe a mechanism of protein organization that is necessarily at play at cell-cell contacts due to their unique physical constraints, and to test this proposition by investigating a cell-cell contact where changes in membrane-membrane distance are fundamental to the cellular function of the junction. We hope that this thesis suggests some important design principles, motivated by some simple physical properties of cell-cell contacts, for developing the next generation of immuno-therapeutics against cancer and infectious disease.

Chapter 4 of this thesis covered my work on CellScope Loa, a mobile-microscope for quantifying a blood-borne parasitic worm directly at the point-of-care. I had the privilege of traveling to Cameroon in July 2015 to perform training for the initial pilot deployment. Since that time, more than 50,000 tests have been run on devices in Cameroon and Nigeria, and more than 30,000 doses of Ivermectin have been distributed to patients as a result of diagnostic decisions aided by the device. The applications of CellScope Loa have quickly grown beyond the envisioned "test and treat" strategy pioneered by the Gates foundation consortium that we participated in. In 2016, we prepared fifteen devices for donation to the Carter Foundation for a mapping study of *L. loa* distribution in a region of Nigeria that was thought to be hypoendemic for the parasite. It turned out after examining more than 10,000 patients with the device, while a fraction of the population was infected with Loa, not a single patient had a level of infection that would generate a risk of adverse events upon treatment with Ivermectin. This means that Ivermectin could potentially be safely delivered within this region without the need to test each individual patient, a "map and clear" strategy to complement "test and treat". Together, these therapeutic approaches that use CellScope Loa to determine how to safely treat patients with Ivermectin are poised to impact on treatment of Onchocerciasis across Africa.